Title

The effects of high energy processes on atmospheric species: Investigations of isotope effects in the photoionization of N2 and CO2 and in the corona discharge formation of N2O and light-scattering from photochemically-generated aerosols

Author

Randazzo, John B.

Publication Date

2014

Peer reviewed|Thesis/dissertation

The effects of high energy processes on atmospheric species: Investigations of isotope effects in the photoionization of N_2 and CO_2 and in the corona discharge formation of N_2O and light-scattering from photochemically-generated aerosols

by

John B. Randazzo

A dissertation submitted in partial satisfaction of the

requirements for the degree of

Doctor of Philosophy

in

Chemistry

in the

Graduate Division

of the

University of California, Berkeley

Committee in charge:

Professor Kristie A. Boering, Chair
Professor Ronald C. Cohen
Professor Imke de Pater

Spring 2014

Abstract

The effects of high energy processes on atmospheric species: Investigations of isotope effects in the photoionization of N_2 and CO_2 and in the corona discharge formation of N_2O and light-scattering from photochemically-generated aerosols

by

John B. Randazzo

Doctor of Philosophy in Chemistry

University of California, Berkeley

Professor Kristie A. Boering, Chair

In the research reported in this dissertation, experiments were designed and performed to investigate the interactions of atmospheric gases with high-energy photons and/or electrons, which can produce highly reactive ions and radicals via ionization and dissociation, and which in turn may result in previously unexplored isotope effects or in formation of aerosols with optical properties that are difficult to predict and measure. Knowledge of both isotope effects and the optical properties of aerosols formed by UV photolysis of precursor gases are highly relevant for interpreting observations of and understanding chemical and physical processes occurring in a wide variety of planetary atmospheres. Here, photoionization efficiency spectra of isotopologues of N_2 ($^{14}N_2$, $^{15}N^{14}N$, and $^{15}N_2$) and CO_2 ($^{12}C^{16}O_2$, $^{13}C^{16}O_2$, $^{12}C^{16}O^{18}O$, $^{13}C^{16}O^{18}O$, $^{12}C^{18}O_2$, and $^{13}C^{18}O_2$) using synchrotron radiation at the Advanced Light Source were measured, the polarization and intensity of laser light scattered by photochemically-generated aerosols suspended in the gas phase as a function of scattering angle were investigated *in situ* using a newly designed and built computer-controlled custom polarimeter, and the isotopic composition of N_2O produced in a newly designed and constructed corona discharge apparatus was measured.

Isotope effects in the photoionization of N_2 and CO_2 may be important in determining the isotopic composition in planetary atmospheres, such as those on Earth and Titan in the case of N_2 and on Mars and Venus in the case of CO_2, and provide new data to address uncertainties in spectral peak assignments in the photoionization spectra, and yet have not been previously measured. For example, for N_2, the measured differences in photoinization efficiencies between $^{14}N_2$ and $^{15}N^{14}N$, may help resolve differences in the isotopic composition of N_2 versus that for HCN observed on Titan. In addition, the spectral assignment for the feature at 15.677 eV in the $^{14}N_2$ photoionization spectrum has remained controversial despite decades of research. The measured isotope shifts for this peak are compared with isotope shifts predicted using Herzberg equations for the isotopic differences in harmonic oscillator energy levels plus the first anharmonic correction for the three proposed assignments. The measured isotope shifts for this peak relative to $^{14}N_2$ are 0.015±0.001 eV for $^{15}N_2$ and 0.008±0.001 eV for $^{15}N^{14}N$ (reported here for the first time), which match most closely with the isotope shifts predicted for transitions to the (A $^2\Pi_u$ v'=2)4sσ_g $^1\Pi_u$ state of 0.0143 eV for $^{15}N_2$ and 0.0071 eV for $^{15}N^{14}N$, and thus assignment to this transition is favored. For CO_2, the measured isotope effects in photoionization yield ratios of photoionization rate coefficients, *J*

(i.e., photoionization cross-sections convolved with the solar spectrum and integrated over all photoionization energies), that are less than 1: $J(^{13}C^{16}O_2)/J(^{12}C^{16}O_2) = 0.97 \pm 0.02$, $J(^{12}C^{16}O^{18}O)/J(^{12}C^{16}O_2) = 0.97 \pm 0.02$, $J(^{13}C^{16}O^{18}O)/J(^{12}C^{16}O_2) = 0.97 \pm 0.02$, $J(^{12}C^{18}O_2)/J(^{12}C^{16}O_2) = 0.99 \pm 0.02$, and $J(^{13}C^{18}O_2)/J(^{12}C^{16}O_2) = 0.98 \pm 0.02$. These isotope effects in photoionization rate coefficients are likely large enough to contribute to (if not dominate) enrichments in ^{13}C in CO_2 in the martian atmosphere, which have largely been attributed to atmospheric escape over billions of years, and may also be important in the atmospheres of Venus and Earth, thus warranting inclusion in models of the isotopic composition of CO_2 in planetary atmospheres.

Aerosols generated by UV photolysis of precursor gases are present in a number of planetary atmospheres, including Titan, and most likely, early Earth and early Mars, and are expected to have a profound effect on atmospheric radiative transfer, yet the number of investigations of aerosol optical properties suspended in the gas phase is extremely limited. In order to measure the intensity and polarization state of light scattered by photochemically-generated aerosols as a function of scattering angle, a custom polarimeter consisting of a quarter-wave plate mounted in a computer-controlled rotating stage and a linear polarizer was designed and built. The polarimeter was placed into the 13 L reaction chamber to measure the intensity and polarization of light scattered by photochemically-generated aerosol *in situ*, and the parameters of the Stokes vector were calculated at a number of scattering angles. The results demonstrate that this technique can be used to measure the polarization and angular dependence (phase function) of light scattered by aerosol particles *in situ* while still suspended in the gas phase, with the ultimate goal of using these measurements to attain the size distribution and index of refraction of the aerosol particles for applications to radiative transfer in planetary atmospheres, such as early Earth and Titan.

Measurements of the isotopic composition of N_2O can be used to infer its sources and sinks, and understanding the isotopic composition of N_2O formed by corona discharge in air (a process which can occur, for example, in thunderstorms) may be important for understanding atmospheric observations of N_2O if the isotope effects in N_2O formation are large. To measure the isotopic composition of N_2O formed by corona discharge, a new apparatus was designed and built to produce N_2O by corona discharge and isolate and collect the N_2O cryogenically for subsequent analysis by continuous flow isotope ratio mass spectrometry. Results from the first measurements of isotopic composition (reported as $\delta^{15}N$, $\delta^{18}O$, and the "site-specific" $\delta^{15}N$ values, $\delta^{15}N^{\alpha}$ and $\delta^{15}N^{\beta}$) indicate that, under some conditions, the isotopic composition of N_2O formed by corona discharge is significantly different from the reactant N_2 and O_2 and from background tropospheric N_2O, although none of the measurements reported here show fractionations larger than 4% (i.e., 40 per mil) relative to the starting N_2 or O_2 or tropospheric N_2O. Additional testing under other experimental conditions (e.g., pressure, discharge residence time, discharge current) is warranted to assess whether fractionations might be large enough to include in atmospheric models.

For my family, who has always been there for me

Table of contents

List of tables

List of figures

Acknowledgements

I would like to thank my advisor, Professor Kristie Boering, whose support and guidance shaped me into a great scientist. I would also like to thank my committee members, Professor Imke de Pater and Professor Ron Cohen, whose guidance and understanding helped this thesis come together. My former and current labmates: Dr. Phil Croteau for helping me run experiments and analyze data for the N_2 photoionization work and doing the initial work on the aerosol scattering project, Dr. Emily Chu for setting up the aerosol chamber in its current state and teaching me all its nuances, Amadu Kanu for his encouraging feedback on my oral presentations, Dr. Aaron Wiegel for doing the preliminary literature research for the corona discharge project, Lauren Garofalo for always being available to share ideas with, undergraduates Ryan Roppel and Jon Weiner for helping collect data, and other Boering group members, Dr. Karen Fielberg, Mica Smith, and Dr. Armando Estillore, for their rich discussions, motivation, encouragement, and advice on all topics, personal and scientific. My collaborators, Professor Yuk Yung of Caltech and Dr. Danie Liang of Caltech and Academia Sinica for their modeling of N_2 photoionization in Titan's atmosphere using our measured cross-sections. Scientists at the Advanced Light Source, Dr. Musa Ahmed, Dr. Oleg Kostko, and Dr. Amir Golan for helping me set up and run experiments at the ALS and for guidance in interpreting the measured data.

On a more personal side, I would like to thank my friends and classmates, particularly those that came to weekly tea meetings: Laura Brandt for being a persistent friend and wonderful roommate, Sara Thoi for always organizing events and outings, Ben Rancatore for being a model of hard work, Troy Moore for his enlightening discussions, Mike Coyle for his constant encouragement, and Chris Snedigar for his reassurance during our last semester. Without their inspiration and kind words, graduate school would have been a much bleaker place. In the past couple years, Melanie Raygoza has always been there to lend her unwavering support and has believed in me through all the struggles and hurdles. I would like to especially thank my parents, Patricia Randazzo and Frank Randazzo, my brother, Sam Randazzo, and my sister, Francie Randazzo-Capp, for always believing in me and encouraging me.

Chapter 1

Introduction and overview

In this dissertation, I report on measurements and analysis of isotope effects in the non-dissociative photoionization of molecular nitrogen (N_2) and carbon dioxide (CO_2), the development and demonstration of a new *in situ* technique for measuring the intensity and polarization of light scattered by photochemically-generated aerosols suspended in the gas phase, and the design, construction, and preliminary testing of a new apparatus to produce and collect nitrous oxide (N_2O) via corona discharge in air for subsequent analysis of the N_2O isotopic composition. The overarching goal of this work was to investigate the interactions of atmospheric gases with high-energy photons and/or electrons, which can produce highly reactive ions and radicals via ionization and dissociation, and which in turn may result in previously unexplored isotope effects (as revealed in the N_2, CO_2, and N_2O experiments) or in formation of aerosols with optical properties that are difficult to predict and measure (as in the UV photolysis/light-scattering experiments), both of which are highly relevant for interpreting observations of and understanding chemical and physical processes occurring in a wide variety of planetary atmospheres. Each of the laboratory investigations reported here was designed to contribute missing information on the isotopic or optical properties of gases and aerosols, needed for a more fundamental understanding of the isotopic composition of atmospheric gases or the effect of aerosols on radiative transfer in many planetary atmospheres, ranging from present day Earth to Earth billions of years ago and from other terrestrial planets in our solar system, such as Mars and Venus, to Saturn's moon, Titan. Given below is an overview of each of the individual experimental investigations of this dissertation, including both the motivations for and the advances made by each of these projects.

Chapter 2: Isotope effects and spectroscopic assignments in the non-dissociative photoionization spectrum of N_2

In Chapter 2, I expand upon previous work in our group in which we tested for the possible influence of measured isotope effects in the non-dissociative photoionization of $^{14}N_2$, $^{15}N^{14}N$, and $^{15}N_2$ using synchrotron radiation at the Advanced Light Source (ALS) on the isotopic composition of N_2 and HCN in Titan's atmosphere. Here, I present additional experimental details on the energy and intensity calibrations and on the overall accuracy and precision for the isotope-specific photoionization cross-sections first reported by *Croteau* [2010] and by *Croteau, Randazzo, Kostko, Ahmed, Liang, Yung, and Boering* [2011], and present the magnitudes of the isotope shifts for a number of specific transitions, including those for $^{15}N^{14}N$ which have not been reported before. I then use the measured isotope shifts to address long-standing controversies over spectral peak assignments, especially the feature at 15.677 eV in the $^{14}N_2$ spectrum (the so-called second "cathedral" peak), which has had assignments proposed to three different transitions by various investigators [*McCormack et al.*, 1990; *Sommavilla et al.*, 2002; *Lefebvre-Brion*, 2005]. More generally, the measured isotope shifts in both energy and intensity for $^{15}N_2$ and $^{15}N^{14}N$ relative to $^{14}N_2$ provide new experimental benchmarks for theoretical calculations and may yield a greater understanding of the quantum states involved and their interaction energies with one another and with the ionization continuum. Such improvements in theory are of importance in the field of theoretical physical chemistry and will also increase confidence in theoretical calculations of isotope effects needed in applications to planetary atmospheres for molecular systems for which isotopic measurements are not yet available.

Chapter 3: Measurements of isotope effects in the non-dissociative photoionization of CO_2 and applications to spectroscopy and planetary atmospheres

In Chapter 3, I present measurements similar to those presented in Chapter 2 for isotopic N_2 of the photoionization efficiency spectra of $^{12}C^{16}O_2$, $^{13}C^{16}O_2$, $^{12}C^{16}O^{18}O$, $^{13}C^{16}O^{18}O$, $^{12}C^{18}O_2$, and $^{13}C^{18}O_2$ from 13.7 eV to 20 eV using synchrotron radiation at the ALS. Isotope effects in the photoionization of CO_2 may be important in determining the isotopic composition in the CO_2-rich planetary atmospheres of Mars and Venus [e.g., *Fox*, 2004; *Fox and Paxton*, 2005] over billions of years via photochemical processes, self-shielding [e.g., *Lyons*, 2007, 2008], and/or atmospheric loss processes [e.g., *Dubinin et al.*, 2011], and yet have not been measured prior to this work. The measured isotope-specific photoionization cross-sections are convolved with the solar spectrum to yield photoionization rate coefficients (the so-called J-values) which show differences in the resulting photoionization rate coefficients that are large enough to warrant inclusion in models of the isotopic composition of CO_2 in planetary atmospheres, especially in light of recent [*Webster et al.*, 2013; *Mahaffy et al.*, 2013] and upcoming [e.g., *Atreya et al.*, 2013] observations of the isotopic composition of CO_2 in the martian atmosphere aimed at determining the mechanism and extent of atmospheric escape over the course of martian history. Indeed, isotope effects in the direct photoionization of CO_2 may be large enough, for example, to be a substantial contributor to the enrichment in ^{13}C relative to ^{12}C in present-day martian CO_2 that is now largely interpreted as enrichment due to preferential escape of ^{12}C [e.g., *Webster et al.*, 2013; *Mahaffy et al.*, 2013]. In addition, similar to the isotopic N_2 spectra presented in Chapter 2, the newly measured isotope-specific photoionization cross-sections also provide important new constraints on spectroscopic assignments for electronic and vibrational states involved in the CO_2 spectral transitions as well as new benchmarks for theory.

Chapter 4: Demonstration of a new *in situ* technique for measuring light scattering by aerosols suspended in the gas phase

In Chapter 4, I discuss the design, development, and implementation of a custom polarimeter which is capable of *in situ* measurements of the angular dependence of the polarization state and of the intensity of laser light scattered by photochemically-generated aerosol suspended in the gas phase. Photochemically-generated aerosols are present in a variety of planetary atmospheres, including Titan [e.g., *Tomasko et al.*, 2005] and, most likely, early Earth and Mars [e.g., *Trainer*, 2013], where they have a profound effect on radiative transfer, determined by their optical properties. However, most investigations of aerosol optical properties, which are needed to accurately model radiative transfer in a planetary atmosphere and in turn determine the extent to which aerosols warm or cool the atmosphere or surface, have been performed on thin films of the aerosols collected on slides rather than *in situ* measurements of aerosol particles suspended in the gas phase. One exception is the investigation by *Hasenkopf et al.* [2010], in which the refractive indices of Titan- and early-Earth-analog aerosols suspended in the gas phase were measured *in situ*, but which is restricted to measurements of spherical particles due to limitations of the residence time in their instrument. In this chapter, I present preliminary results of light-scattering measurements using a custom polarimeter incorporated into a 13 L reaction chamber capable of forming not only spherical particles, but also fractal particles, which are likely to be important on both Titan [*Tomasko et al.*, 2005] and early Earth [*Wolf and Toon*, 2010]. In principle, elements of the scattering matrix for the free-floating aerosol particles can be derived from the polarimeter measurements and then inverted to attain the size distribution and index of refraction of the aerosol

particles at the laser wavelength of each experiment. The results presented here for size-calibrated polystyrene spheres and for aerosol particles generated by UV photolysis of acetylene (C_2H_2) demonstrate 'proof of concept' that *in situ* aerosol scattering measurements can be carried out in our reaction chamber and that elements of the scattering matrix can be retrieved.

Chapter 5: The isotopic composition of nitrous oxide formed in a corona discharge in air

In Chapter 5, I discuss the design, construction, and preliminary results from an apparatus to generate and collect N_2O by corona discharge (a low-current plasma discharge caused by ionization of gases in a high-voltage gradient) in air for subsequent measurements of the N_2O isotopic composition by isotope ratio mass spectrometry (IRMS). Measurements of the isotopic composition of N_2O in Earth's atmosphere have been used previously to infer the sources of N_2O to the atmosphere [*Sowers et al.*, 2002; *Röckmann et al.*, 2003; *Röckmann and Levin*, 2005; *Park et al.*, 2012], with a particular interest in determining the cause of the 20% increase in the concentration of N_2O in the atmosphere since 1750. Recently, *Park et al.* [2012] used the measured trends and seasonal cycles in the isotopic ratios of N_2O ($^{15}N/^{14}N$ and $^{18}O/^{16}O$), especially the relative enrichment or depletion of the ^{15}N at the central N atom versus the terminal N atom in N_2O, as an isotopic fingerprint to demonstrate empirically that an increase in the use of nitrogen-based fertilizers for agriculture is indeed the major cause of the increase in concentration of N_2O since the 1940s. However, there is still room for improvement in estimates of all anthropogenic and natural sources of N_2O and how these may change as climate changes, as well as how isotopic N_2O measurements may inform these uncertainties.

One example that invites additional investigation is the isotopic composition of N_2O produced by corona discharge in thunderstorms. *Wofsy* [2011] showed that an enhancement of N_2O mixing ratios in the upper troposphere suggests the presence of unaccounted for tropical sources of N_2O. Corona discharge in thunderstorms is known to produce significant amounts of N_2O on a local scale [*Griffing*, 1977; *Hill et al.*, 1984]. While thunderstorms are only a small source of N_2O globally, if the isotopic signature of N_2O formed by corona discharge is greatly different from the isotopic composition of background N_2O in the troposphere or of its various sources or sinks, then the effect of contributions of N_2O formed by corona discharge on the isotopic composition of tropospheric N_2O, and how such a source may have changed over time, could be important for interpreting long-term trends and/or seasonal cycles measured over time, such as those in *Park et al.* [2012]. Indeed, it is thought, for example, that the frequency and severity of thunderstorms may increase as climate changes (or has changed already [e.g., *Trapp et al.*, 2007; *Diffenbaugh et al.*, 2013]). In addition, two previous laboratory studies have shown very large enrichments in ^{15}N relative to the initial N_2 in the gaseous species formed by electric discharges: 5 to 25% enrichments in ^{15}N were measured by magnetic sector mass spectrometry in nitrogen oxides formed in a glow discharge at 77 K [*Manuccia and Clark*, 1976], while 30-fold enrichments in ^{15}N atoms were measured by electron spin resonance (ESR) spectroscopy in nitrogen gas passed through a pulsed discharge [*Gorshunov and Gudenko*, 2003]. These intriguing results suggest that excited-state nitrogen and oxygen chemistry and/or ion-molecule reactions in a discharge could indeed involve large isotope effects in the formation of N_2O, at least for the $^{15}N/^{14}N$ ratio.

To investigate the isotopic composition of N_2O formed in a corona discharge – the discharge phenomenon most relevant for N_2O in the atmosphere – I designed and built an apparatus consisting of a high-voltage corona discharge cell and vacuum and cryogenic system for collecting the N_2O produced for offline measurements of the isotopic composition by continuous flow IRMS [e.g., *Croteau*, 2010; *Park et al.*, 2012]. Preliminary results indicate interesting differences in the

isotopic composition of the N_2O formed in the corona discharge with respect to the starting N_2 and O_2 from which it was formed, as well as differences with respect to the isotopic composition of N_2O present in the atmosphere to which, for example, thunderstorm-generated N_2O would be added, although the enormous ^{15}N enrichments of the previous two studies on nitrogen and nitrogen oxides in a discharge [*Manuccia and Clark,* 1976; *Gorshunov and Gudenko,* 2003] were not observed under the conditions tested so far. As more measurements are collected over more experimental conditions using this new apparatus, insights into various controls on the nitrogen and oxygen isotopic composition of N_2O produced by corona discharge can be obtained and the range of isotopic compositions so produced can be tested in atmospheric box models to test for their possible influence on background tropospheric N_2O isotopic compositions as well as on long-term trends, seasonal cycles, and interannual variations.

Atreya, S.K., M.G. Trainer, H.B. Franz, M.H. Wong, H.L.K. Manning, C.A. Malespin, P.R. Mahaffy, P.G. Conrad, A.E. Brunner, L.A. Leshin, J.H. Jones, C.R. Webster, T.C. Owen, R.O. Pepin, and R. Navarro-Gonzalez (2013) Primordial argon isotope fractionation in the atmosphere of Mars measured by the SAM instrument on Curiosity and implications for atmospheric loss, *Geophys. Res. Lett.*, *40*, 5605–5609, doi:10.1002/2013GL057763.

Croteau, P. (2010) Nitrous oxide and molecular nitrogen isotopic compositions and aerosol optical properties: experiments and observations relevant to planetary atmospheres. University of California - Berkeley.

Croteau, P., J.B. Randazzo, O. Kostko, M. Ahmed, M.C. Liang, Y.L. Yung, and K.A. Boering (2011) Measurements of isotope effects in the photoionization of N_2 and implications for Titan's atmosphere, *Astrophys. J. Lett.*, *728*.

Diffenbaugh, N.S., M. Scherer, and R.J. Trapp (2013) Robust increases in severe thunderstorm environments in response to greenhouse forcing, *Proc. Natl. Acad. Sci. U. S. A.*, *110*, 16361–16366, doi:10.1073/pnas.1307758110.

Dubinin, E., M. Fraenz, A. Fedorov, R. Lundin, N. Edberg, F. Duru, and O. Vaisberg (2011) Ion energization and escape on Mars and Venus, *Space Sci. Rev.*, *162*, 173–211, doi:10.1007/s11214-011-9831-7.

Fox, J.L. (2004) CO_2^+ dissociative recombination: A source of thermal and nonthermal C on Mars, *J. Geophys. Res.-Space Phys.*, *109*, A08306, doi:10.1029/2004JA010514.

Fox, J.L., and L.J. Paxton (2005) C and C^+ in the Venusian thermosphere/ionosphere, *J. Geophys. Res.-Space Phys.*, *110*, A01311, doi:10.1029/2004JA010813.

Gorshunov, N.M., and S.V. Gudenko (2003) Enrichment of the nitrogen atomic component with the ^{15}N isotope in a post-discharge zone, *Jetp Lett.*, *77*, 162–166, doi:10.1134/1.1571874.

Griffing, G.W. (1977) Ozone and oxides of nitrogen-production during thunderstorms, *J. Geophys. Res.-Oceans Atmospheres*, *82*, 943–950, doi:10.1029/JC082i006p00943.

Hasenkopf, C.A., M.R. Beaver, M.G. Trainer, H.L. Dewitt, M.A. Freedman, O.B. Toon, C.P. McKay, and M.A. Tolbert (2010) Optical properties of Titan and early Earth haze laboratory analogs in the mid-visible, *Icarus*, *207*, 903–913, doi:10.1016/j.icarus.2009.12.015.

Hill, R.D., R.G. Rinker, and A. Coucouvinos (1984) Nitrous oxide production by lightning, *J. Geophys. Res.-Atmospheres*, *89*, 1411–1421, doi:10.1029/JD089iD01p01411.

Lefebvre-Brion, H. (2005) Assignment in the near-threshold absorption spectrum of N_2, *J. Chem. Phys.*, *122*.

Lyons, A.R. (2008) Photolysis of long-lived predissociative molecules as a source of mass-independent isotope fractionation: The example of SO_2. *In* Advances in Quantum Chemistry, Vol 55: Applications of Theoretical Methods to Atmospheric Science. J.R. Sabin and E. Brandas, editors. 57–74.

Lyons, J.R. (2007) Mass-independent fractionation of sulfur isotopes by isotope-selective photodissociation of SO_2, *Geophys. Res. Lett.*, *34*, L22811, doi:10.1029/2007GL031031.

Mahaffy, P.R., C.R. Webster, S.K. Atreya, H. Franz, M. Wong, P.G. Conrad, D. Harpold, J.J. Jones, L.A. Leshin, H. Manning, T. Owen, R.O. Pepin, S. Squyres, and M. Trainer (2013) Abundance and isotopic composition of gases in the martian atmosphere from the Curiosity rover, *Science, 341*, 263–266, doi:10.1126/science.1237966.

Manuccia, T.J., and M.D. Clark (1976) Enrichment of N^{15} by chemical reactions in a glow discharge at 77°K, *Appl. Phys. Lett.*, *28*, 372–374, doi:10.1063/1.88785.

McCormack, E.F., S.T. Pratt, J.L. Dehmer, and P.M. Dehmer (1990) Double-resonance spectroscopy of autoionizing states of N_2 near the ionization threshold, *Phys. Rev. A, 42*, 5445–5451.

Park, S., P. Croteau, K.A. Boering, D.M. Etheridge, D. Ferretti, P.J. Fraser, K.-R. Kim, P.B. Krummel, R.L. Langenfelds, T.D. van Ommen, L.P. Steele, and C.M. Trudinger (2012) Trends and seasonal cycles in the isotopic composition of nitrous oxide since 1940, *Nat. Geosci.*, *5*, 261–265, doi:10.1038/NGEO1421.

Röckmann, T., J. Kaiser, and C.A.M. Brenninkmeijer (2003) The isotopic fingerprint of the pre-industrial and the anthropogenic N_2O source, *Atmospheric Chem. Phys.*, *3*, 315–323.

Röckmann, T., and I. Levin (2005) High-precision determination of the changing isotopic composition of atmospheric N_2O from 1990 to 2002, *J. Geophys. Res.-Atmospheres*, *110*, D21304, doi:10.1029/2005JD006066.

Sommavilla, M., U. Hollenstein, G.M. Greetham, and F. Merkt (2002) High-resolution laser absorption spectroscopy in the extreme ultraviolet, *J. Phys. B-At. Mol. Opt. Phys.*, *35*, 3901–3921.

Sowers, T., A. Rodebaugh, N. Yoshida, and S. Toyoda (2002) Extending records of the isotopic composition of atmospheric N_2O back to 1800 AD from air trapped in snow at the South Pole and the Greenland Ice Sheet Project II ice core, *Glob. Biogeochem. Cycles*, *16*, 1129, doi:10.1029/2002GB001911.

Tomasko, M.G., B. Archinal, T. Becker, B. Bezard, M. Bushroe, M. Combes, D. Cook, A. Coustenis, C. de Bergh, L.E. Dafoe, L. Doose, S. Doute, A. Eibl, S. Engel, F. Gliem, B. Grieger, K. Holso, E. Howington-Kraus, E. Karkoschka, H.U. Keller, R. Kirk, R. Kramm, M. Kuppers, P. Lanagan, E. Lellouch, M. Lemmon, J. Lunine, E. McFarlane, J. Moores, G.M. Prout, B. Rizk, M. Rosiek, P. Rueffer, S.E. Schroder, B. Schmitt, C. See, P. Smith, L. Soderblom, N. Thomas, and R. West (2005) Rain, winds and haze during the Huygens probe's descent to Titan's surface, *Nature*, *438*, 765–778, doi:10.1038/nature04126.

Trainer, M.G. (2013) Atmospheric prebiotic chemistry and organic hazes, *Curr. Org. Chem.*, *17*, 1710–1723.

Trapp, R.J., N.S. Diffenbaugh, H.E. Brooks, M.E. Baldwin, E.D. Robinson, and J.S. Pal (2007) Changes in severe thunderstorm environment frequency during the 21st century caused by anthropogenically enhanced global radiative forcing, *Proc. Natl. Acad. Sci. U. S. A.*, *104*, 19719–19723, doi:10.1073/pnas.0705494104.

Webster, C.R., P.R. Mahaffy, G.J. Flesch, P.B. Niles, J.H. Jones, L.A. Leshin, S.K. Atreya, J.C. Stern, L.E. Christensen, T. Owen, H. Franz, R.O. Pepin, and A. Steele (2013) Isotope ratios of H, C, and O in CO_2 and H_2O of the martian atmosphere, *Science, 341,* 260–263, doi:10.1126/science.1237961.

Wofsy, S.C. (2011) HIAPER Pole-to-Pole Observations (HIPPO): fine-grained, global-scale measurements of climatically important atmospheric gases and aerosols, *Philos. Trans. R. Soc. -Math. Phys. Eng. Sci., 369,* 2073–2086, doi:10.1098/rsta.2010.0313.

Wolf, E.T., and O.B. Toon (2010) Fractal organic hazes provided an ultraviolet shield for early Earth, *Science, 328,* 1266–1268, doi:10.1126/science.1183260.

Chapter 2

Isotope effects and spectroscopic assignments in the non-dissociative photoionization spectrum of N_2

Adapted from a manuscript of the same title in press in *J. Chem. Phys.* on May 7, 2014 authored by Randazzo, J. B., P. Croteau, O. Kostko, M. Ahmed, and K. A. Boering.

Abstract

Photoionization efficiency spectra of $^{14}N_2$, $^{15}N^{14}N$, and $^{15}N_2$ from 15.5 to 18.9 eV were measured using synchrotron radiation at the Advanced Light Source at Lawrence Berkeley National Laboratory with a resolution of 6 meV, and significant changes in peak energies and intensities upon isotopic substitution were observed. Previously, we reported the isotope shifts and their applications to Titan's atmosphere. Here, we report more extensive experimental details and tabulate the isotope shifts of many transitions in the N_2 spectrum, including those for $^{15}N^{14}N$, which have not been previously reported. The isotope shifts are used to address several long-standing ambiguities in spectral peak assignments just above the ionization threshold of N_2. The feature at 15.677 eV (the so-called second "cathedral" peak) is of particular interest in this respect. The measured isotope shifts for this peak relative to $^{14}N_2$ are 0.015±0.001 eV for $^{15}N_2$ and 0.008±0.001 eV for $^{15}N^{14}N$, which match most closely with the isotope shifts predicted for transitions to the (A $^2\Pi_u$ v'=2)4sσ_g $^1\Pi_u$ state using Herzberg equations for the isotopic differences in harmonic oscillator energy levels plus the first anharmonic correction of 0.0143 eV for $^{15}N_2$ and 0.0071 eV for $^{15}N^{14}N$. More generally, the isotope shifts measured for both $^{15}N_2$ and $^{15}N^{14}N$ relative to $^{14}N_2$ provide new benchmarks for theoretical calculations of interferences between direct and indirect autoionization states which can interact to produce intricate resonant structures in molecular photoionization spectra in regions near ionization thresholds.

2.1 Introduction

Isotope effects in the spectrum of molecular nitrogen have long been used to make and confirm spectral assignments, determine spectroscopic parameters for the different isotopic species, characterize perturbations caused by interactions between excited states of similar energies, and compare experimental data with theoretical calculations [*Bayes and Kistiakowsky*, 1960; *Carroll and Mahon-Smith*, 1963; *Mahon-Smith and Carroll*, 1964; *Ogawa*, 1964; *Ogawa et al.*, 1964; *Yoshino et al.*, 1975; *Yoshino and Tanaka*, 1977; *Burridge and Hewitt*, 1984; *Hajim and Carroll*, 1987; *Sprengers et al.*, 2003, 2005]. In a previous publication [*Croteau et al.*, 2011], we reported measurements of the photoionization efficiency spectra of $^{14}N_2$, $^{15}N^{14}N$, and $^{15}N_2$ using vacuum ultraviolet (VUV) synchrotron radiation from the Advanced Light Source (ALS) at Lawrence Berkeley National Laboratory from the ionization threshold of N_2 at 15.5 eV to 18.9 eV. The measured isotope effects have potential importance in a variety of terrestrial [*Aikin*, 2001; *Kaye*, 1987] and extraterrestrial [*Terzieva and Herbst*, 2000; *Fox and Dalgarno*, 1980, 1983; *Fox*, 1993; *Fox and Hać*, 1997; *Wilson and Atreya*, 2004; *Waite et al.*, 2007; *Imanaka and Smith*, 2007, 2009, 2010; *Muskatel et al.*, 2011; *Hily-Blant et al.*, 2013] environments, and, in the earlier work, we tested for their possible influence on the isotopic compositions of N_2 and HCN in Titan's atmosphere. The singly substituted isotopic species, $^{15}N^{14}N$, is especially relevant for planetary atmospheres and interstellar space, but has been spectroscopically studied less extensively than the doubly substituted molecule, $^{15}N_2$. It was determined that including N_2 photoionization isotope

effects in atmospheric models of nitrogen-rich atmospheres may help to resolve discrepancies between models and measurements where earlier [*Liang et al.*, 2007] only neutral species were considered.

Here, we document additional experimental details on the energy and intensity calibrations and on the overall accuracy and precision for the isotope-specific photoionization cross-sections first reported in by *Croteau et al.* [2011]. We also present the magnitudes of the isotope shifts for a number of specific transitions, including those for $^{15}N^{14}N$ which have not been reported before. The isotope shifts are then used to address ambiguities in spectral peak assignments just above the ionization threshold of N_2.

2.2 Methods

In order to determine the relative photoionization cross-sections as a function of energy for the three isotopic species of N_2, the experiments were performed using a continuous molecular beam of N_2 coupled to the 3 m monochromator at Terminal 3 of the Chemical Dynamics Beamline (CDB) at the Advanced Light Source [*Nicolas et al.*, 2006; *Kostko et al.*, 2008], as shown in Figure 2.1. A beam of N_2 was formed from a mixture of $^{14}N_2$ (99.999% purity N_2, Airgas, Randor, PA), $^{15}N^{14}N$ (99%, Icon Services, Summit, NJ), and $^{15}N_2$ (98%, Icon Services), prepared by flowing each of the three different isotopic gases through three calibrated mass-flow controllers ("MFCs"; Model 1179, 20 sccm full range; 1% full scale accuracy; MKS Instruments, Andover, MA) controlled to 2.5 sccm. The gas mixture was then expanded through a 100 μm diameter orifice into a vacuum chamber, forming a molecular beam, which was then skimmed to 2 mm. Although the temperature of the beam was not measured directly, experiments done under similar conditions show [*Aoiz et al.*, 1999; *Mori et al.*, 2005] N_2 with a translational and rotational temperature of ~50 K. At these temperatures, the Boltzmann distribution of rotational energy levels for N_2 peaks at J=2, and 99% of molecules are in rotational states with $J \leq 7$, while no vibrational excitation is expected. Monochromatized vacuum ultraviolet (VUV) light from the synchrotron passed through a He-gas filter to remove any light from higher harmonics generated by the undulator, then passed through a 50 μm slit, intersected the molecular beam, and was detected by a NIST-calibrated Si-photodiode. The combination of the monochromator and the 50 μm slit width resulted in light with a spectral bandwidth of 6 meV FWHM as determined by measuring resonances of atomic silicon from 9.82 eV to 9.93 eV at various slit widths [*Kaiser et al.*, 2010].

The VUV light ionized some of the N_2 molecules, which were directed to a time-of-flight (TOF) mass spectrometer (R. M. Jordan Co., Grass Valley, CA) using Wiley-McLaren ion optics. The electric potential on the ion optics was pulsed at 30 kHz, and the start time of the TOF detector was triggered by the start of each pulse. The different velocities imparted to ions of different mass-to-charge ratio (m/z) by the electric potential caused ions of different masses to be separated in the TOF tube, and the ions were detected by collecting the time-dependent signal from a microchannel plate (MCP) detector with a multichannel-scaler card, which was then integrated with a PC. The peaks corresponding to $^{14}N_2^+$, $^{15}N^{14}N^+$, and $^{15}N_2^+$ were each integrated for each 3 meV energy step. The signal was normalized by the photon flux, which was monitored throughout the experiment with the Si-photodiode. The final mixing ratios of $^{14}N_2$, $^{15}N^{14}N$, and $^{15}N_2$ in the molecular beam were determined by taking the average and standard deviation of the signals for the three isotopic species in the relatively featureless regions of the spectra (i.e., in regions of the spectra that are not on-resonance with discrete valence or Rydberg states) since there should be no isotope effects in direct photoionization to the continuum, resulting in mixing ratios for $^{14}N_2$, $^{15}N^{14}N$, and $^{15}N_2$ of 0.339±0.002 (1σ), 0.321±0.002, and 0.340±0.002, respectively. The measured

intensity for each isotopic species was then scaled by the inverse of its mole fraction, so that the overall results shown below represent those for a 1:1:1 mixture. Scaling the intensity by the inverse of the mole fraction for each isotopic species greatly reduced the uncertainty in the 1% full-scale accuracy specification of the mass-flow controllers, corrected for any center-line enrichment in the heavier isotopic species, which may have occurred in the molecular beam [*McLean and Sawyer*, 1974], and corrected for any isotope impurity in each gas cylinder (e.g., the 2% ^{14}N in the cylinder of 98 atom % $^{15}N_2$ gas).

Converting the raw intensity signals measured as a function of monochromator position into photoionization spectra ranging from 15.5 to 18.9 eV involved several steps. First, peaks in the spectra of $^{14}N_2$, $^{15}N^{14}N$, and $^{15}N_2$ were fit to Lorentzian profiles using the Multi-Peak Fit package in Igor Pro, version 6.3 (WaveMetrics, Lake Oswego, OR). Next, in order to create a fully consistent and accurate spectrum over the entire energy range measured, individual experimental runs covering only ~1 eV (due to the file size limitations of the PC used for data acquisition) needed to be "stitched" together and offsets due to the limited mechanical precision of the monochromator taken into account. For example, each energy region – which always included some overlapping data with the adjacent energy regions by design – was scanned two or three times and an average run-to-run offset of 20 meV, with a maximum offset of 40 meV, in the peak energies was observed. This offset can be seen in Figure 2.2(a) in which data from different runs over the same nominal energy region are plotted together. In addition to the constant offset in energy, there was a concern that a compression or expansion of the energy scale (for example, if the energy step size was inaccurately recorded during the experiment) might also occur. As a metric of such possible inaccuracies, a linear regression was calculated in each energy region for peak positions in our experimental spectrum versus the peak positions of well-known peaks in the $^{14}N_2$ spectrum, which are given in Table 2.1. The formula for each linear regression, which had an uncertainty ranging between 1 and 4 meV, was then used to convert the energy scale recorded for each experimental run to the same energy scale recorded in previous studies.

With self-consistent energy scales, the intensity scales between the two or three runs over the same ~1 eV energy regions could then be compared. Individual runs over the same energy region varied due to small differences in detector efficiency from run to run, with a maximum variation in intensity of 10%. For completeness, all of the runs are shown in Figures 2.S1-2.S4 on the energy scale calibrated above and with intensity reported in arbitrary units. For the full energy spectrum figure shown in Section 2.3 and in the single dataset of N_2 isotopologue absorption cross-sections versus energy, however, a single run was chosen in each energy region, rather than averaging together multiple runs (although the 1σ standard deviations of the average intensity for the two or three runs over a particular energy region are also shown for completeness). In order to create a consistent intensity scale for all runs and to merge each run from different energy regions into a single dataset, the areas that contained overlapping data between adjacent energy regions were normalized to the maximum intensity measured within the overlapping data. The overlapping data from the higher energy run were then removed to give a monotonically increasing energy axis. Finally, the intensity scale in the PIE spectra was converted from arbitrary intensity units to absolute cross-sections in cm^2 using the absolute photoionization cross-sections from previous measurements of $^{14}N_2$ [*Samson et al.*, 1977; *Itikawa et al.*, 1986; *Shaw et al.*, 1992].

While linear regressions were the approach taken to calibrate the individual runs used in the full energy spectra, simply using a constant energy offset and using all 3 runs proved to be sufficient when considering only small energy ranges, as we do in several analyses presented in the results and discussion below, particularly in calculating the isotope shifts. For example, in

Figure 2.2(a) the peaks marked with asterisks result from the same transition in three different individual experimental runs. Upon adding a constant to the energy scale recorded in each of the three experimental runs such that the marked peaks were set to exactly 15.677 eV, all other features in the spectra agree to better than 1 meV, as shown in Figure 2.2(b). For calculating the isotope shifts, all runs were used, and the sources and magnitudes of uncertainties in the peak energy differences between the isotopologues can be summarized as follows. The uncertainty returned from peak fitting to Lorentz profiles using Igor Pro ranged from $\pm 5.7 \times 10^{-5}$ eV to $\pm 1.4 \times 10^{-4}$ eV (1σ). Uncertainties in peak energies due to run-to-run variations over small energy ranges, resulting from imprecision in the energy scale calibration discussed above for the data shown in Figure 2.2(b) ranged from $\pm 1.3 \times 10^{-4}$ eV to $\pm 2.2 \times 10^{-4}$ eV (1σ, N=3), based on fitting each of the peaks to Lorentz profiles and then applying the constant offset shown in Figure 2.2(b). Assuming these two sources of uncertainty are random, summing the uncertainties in quadrature and then propagating the errors in calculating the isotope shifts as peak energy differences between $^{14}N_2$, $^{15}N^{14}N$, and $^{15}N_2$ for the 3 different runs yielded statistical uncertainties of $\pm$ 0.0003 eV (1σ) in the isotope shifts in the cathedral peaks region of the spectrum. It is possible that uncertainties in the isotope shifts in a particular energy range are larger than this estimate. The largest effect could result from a combination of the monochromator steps of 3 meV and the bandwidth of 6 meV; we note in several instances that the energy of the fitted peak differed from the energy of the maximum experimental intensity by up to 1 meV in the cathedral peaks region of the spectrum (this occurred in one run for the $^{15}N_2$ peak, despite a good statistical uncertainty to this particular peak fit of $\pm$0.06 meV.) For this reason, we report the uncertainties for the controversial second cathedral peak as $\pm$ 1 meV. Other uncertainties are either much smaller and not expected to contribute or require additional experiments to be performed at higher resolution to quantify them. For example, the effect of possible peak asymmetries due to rotational excitation, which could be different for the different N_2 isotopologues, on the fitted values of the peak maxima is small at the experimental temperature of 50 K; under the rigid rotor approximation and a Boltzmann distribution of rotational energies, we calculated shifts in the peak location to be less than 0.01 meV at 50 K for both $^{14}N_2$ and $^{15}N_2$ when taking rotational excitation into account. In contrast, the possible effect of peak asymmetries resulting from our experimental bandwidth of 6 meV is difficult to quantify. Our analysis of isotope shifts by the measured energy differences between N_2 isotopologue peaks assumes that the 6 meV bandwidth should in large part simply cancel out, but it is conceivable that isotope shifts in energy and intensity of several low intensity peaks that are known to exist from higher resolution spectra [*Sommavilla et al.*, 2002] of $^{14}N_2$ near the same energy as the cathedral peaks, may not completely cancel out (Compare, for example, Figure 2.S5 showing our $^{14}N_2$, $^{15}N^{14}N$, and $^{15}N_2$ data and spectral fits in this region to the high resolution data for $^{14}N_2$ in Figure 8 of *Sommavilla et al.* [2002]). An estimate of the magnitude of such effects on the reported isotope shifts is beyond the scope of this work and provides motivation for future high resolution isotopic spectra, as discussed further below in Section 2.4.

2.3 Results and analysis

Figure 2.3 shows the PIE spectrum for each isotopologue from 15.5 to 18.9 eV, along with peak assignments; the shaded region indicates the 1σ standard deviation of the average intensities from the two or three runs over a particular energy region (see Section 2.2). For the peak assignments given in the figure, we have followed many of the well-established assignments from *Berg et al.* [1991], who used a similar experimental setup to ours, over the same energy region for $^{14}N_2$. For many of the peaks left unidentified by *Berg et al.* [1991] we have followed the

suggestions of *Lefebvre-Brion and Yoshino* [1993] except where otherwise noted. Given these assignments, the most intense features in the photoionization spectra are transitions from the X $^1\Sigma_g^+$ ground state of N_2 to autoionizing Rydberg states, which converge to vibrational levels of the second (A $^2\Pi_u$) and third (B $^2\Sigma_u^+$) ionized states of N_2. Most of the features in the spectra are relatively broad (especially those at energies >15.8 eV), and are therefore fully resolvable at our experimental resolution of 6 meV. Only measurements near the ionization threshold at 15.5 eV show narrower features, as made clear by the higher resolution spectra measured by *Sommavilla et al.* [2002] and *Dehmer et al.* [1984].

The general trend for the isotope shifts in energy, evident in Figure 2.3, is that the peaks arising from transitions to Rydberg states of the molecule occur in the order $^{15}N_2$, $^{15}N^{14}N$, $^{14}N_2$ from lowest to highest energy. This trend is due to isotopic differences between the vibrational energy levels of the ground electronic state and the vibrational energy levels in the excited electronic state of the ion to which the Rydberg series converges [*Ogawa*, 1964; *Herzberg*, 1950], as predicted by *Herzberg* [1950] in Equation 2.1:

$$\Delta E = [E(v') - E(v')_i] - [E(v'') - E(v'')_i] \qquad \text{Eq. 2.1}$$

$$= (1-\rho)[\omega_e'(v'+½) - \omega_e''(v''+½)] - (1-\rho^2)[\omega_e'x_e'(v'+½)^2 - \omega_e''x_e''(v''+½)^2],$$

Here, $E(v)$ and $E(v)_i$ are the vibrational energies of the common and isotopically substituted molecules, respectively, v' and v'' are the vibrational quantum numbers of the upper and lower states of the transition, and ρ is equal to $(\mu/\mu_i)^{½}$, where μ and μ_i are the reduced masses of the common and isotopically substituted molecules, respectively. The measured peak energies and isotope shifts for a number of transitions, along with the isotope shifts predicted by Equation 2.1, are tabulated in Table 2.2, and most of the measured isotope shifts match the predicted values within 1σ or 2σ uncertainty.

2.4 Discussion

Despite decades of study, uncertainties and controversies in spectral peak assignments have remained in this highly complex region of the N_2 spectrum, where many autoionizing Rydberg and valence states overlap and couple [*Ogawa and Tanaka*, 1962; *Ogawa*, 1964; *Cook and Metzger*, 1964; *Cook and Ogawa*, 1965; *Gürtler et al.*, 1977; *Stahel et al.*, 1983; *Dehmer et al.*, 1984; *Giusti-Suzor and Lefebvre-Brion*, 1984; *Kosman and Wallace*, 1985; *Cremaschi et al.*, 1986; *Huber and Jungen*, 1990; *McCormack et al.*, 1991, 1992; *O'Keeffe et al.*, 2012; *Shaw et al.*, 1992]. For CO, a molecule isoelectronic with N_2, *Erman et al.* [1994] used isotope shifts predicted by calculations (such as Equation 2.1) of the vibrational energy level differences between the ground and electronically excited states of CO isotopologues to identify some previously unassigned transitions in the CO spectrum as members of a Rydberg series with principal quantum number n=3 converging to A $^2\Pi$, with members of higher n which had been observed years before [*Ogawa and Ogawa*, 1972]. Thus, *Erman et al.* [1994] were able to extend this series and clarify the overall understanding of the region of the CO spectrum just above the ionization potential. We find here that the isotope shifts for N_2 – especially those for $^{15}N^{14}N$ in combination with $^{15}N_2$ – can be used in a similar way to address ambiguities in spectral peak assignments just above the ionization threshold of N_2.

One prominent example for which the measured and calculated isotope shifts shed new light is for assignment of the peak at 15.677 eV, the second peak in the "cathedral" near the

ionization threshold of N_2, shown in Figure 2.4 on an expanded energy scale, which has remained controversial. Table 2.3 shows calculated isotope shifts for three different assignments proposed by various investigators for this peak, along with our experimentally measured isotopes shifts, while details and a brief history of each proposed assignment are given in Table 2.4. The experimental shifts from this work are 0.0152 ± 0.0003 eV for $^{15}N_2$ and 0.0080 ± 0.0003 eV for $^{15}N^{14}N$ using statistical uncertainties, or 0.015 ± 0.001 eV and 0.008 ± 0.001 eV, respectively, using our more conservative estimate of quantifiable uncertainties (see Section 2.2). These values for the isotope shifts match most closely with the shifts predicted by Equation 2.1 for the (A $^2\Pi_u$ v'=2)4sσ_g $^1\Pi_u$ state: 0.0143 eV for $^{15}N_2$ and 0.0071 eV for $^{15}N^{14}N$. In contrast, the isotope shifts predicted for the (A $^2\Pi_u$ v'=1)3dσ_g $^1\Pi_u$ state from Equation 2.1 are 0.0068 eV for $^{15}N_2$ and 0.0034 eV for $^{15}N^{14}N$ and appear to be outside our experimental uncertainties. *Lefebvre-Brion* [2005a] calculated an isotope shift of 0.035 eV for $^{15}N_2$ for the b' $^1\Sigma_u^+$ v'=44 valence state using coupled-channel Schrödinger calculations, which is much larger than that observed in our experiment. While other possible sources of uncertainty discussed in Section 2.2 – such as the possible influence of lower intensity peaks "buried" by our experimental resolution of 6 meV – may mean that our experimental uncertainties are greater than our conservative estimate of ±0.001 eV, it does seem overly coincidental that the overall effect of these difficult-to-quantify uncertainties or perturbations from nearby Rydberg or valence states would result in our experimental values matching both the $^{15}N_2$ and $^{15}N^{14}N$ isotope shifts with respect to $^{14}N_2$ calculated by Equation 2.1; thus we favor assignment of the second cathedral peak to a transition to the (A $^2\Pi_u$ v'=2)4sσ_g $^1\Pi_u$ state.

Lefebvre-Brion [2005a; b] provides reasons why the assignment to b' $^1\Sigma_u^+$ v'=44 by *Sommavilla et al.* [2002] and *Sommavilla and Merkt* [2006] might be questioned: 1) the theoretical peak width calculated by evaluating the interaction energy of the b' $^1\Sigma_u^+$ v'=44 state with the ionization continuum is 0.01 cm^{-1}, roughly two orders of magnitude smaller than the experimental width of 5 cm^{-1}; 2) coupled-channel Schrödinger equation calculations predicted a rotational constant of 0.66 cm^{-1} for the b' $^1\Sigma_u^+$ v'=44 state, which is much different from the experimentally derived rotational constant of 1.5 cm^{-1}; and 3) peaks corresponding to b' $^1\Sigma_u^+$ v'=42 and 43 were observed in the double resonance spectrum via the electronically and vibrationally excited a $^1\Pi_g$ v''=5 state taken by *McCormack et al.* [1990]; if the peak in question was b' $^1\Sigma_u^+$ v'=44, it should have been observed also. However, *Sommavilla et al.* [2002] and *Sommavilla and Merkt* [2006] also provide strong evidence for their assignment to b' $^1\Sigma_u^+$ v'=44, particularly through the detailed theoretical simulation of the peak shape, width, and height determined by the rotational structure of the peak. Simulations assuming a final state of $^1\Sigma_u^+$ symmetry gave good agreement with the results from their experimental spectrum, while a final state of $^1\Pi_u$ gave significantly worse agreement. Additional theoretical investigations, including calculations for the newly measured $^{15}N^{14}N$ cross-sections and energies reported here, as well as measurements of high resolution PIE spectra for $^{15}N_2$ and/or $^{14}N_2$ are clearly warranted to further clarify the assignment of this peak.

In addition to new constraints on the assignment of the peak at 15.677 eV, several additional measured isotope shifts can also be used to revisit other assignments in the N_2 spectrum, such as the series of peaks occurring at 15.984, 16.209, 16.437, and 16.658 eV. This progression, denoted Progression 1 or P(1) by *Ogawa* [1964], was first identified as a vibrational progression of Rydberg states converging to the A $^2\Pi_u$ state of N_2^+ in the VUV absorption spectrum of N_2. *Lefebvre-Brion and Yoshino* [1993] tentatively assigned the peaks in this progression as (A $^2\Pi_u$ v'=0)4dσ_g $^1\Pi_u$, (A $^2\Pi_u$ v'=1)4dσ_g $^1\Pi_u$, (A $^2\Pi_u$ v'=1)5dσ_g $^1\Pi_u$, and (A $^2\Pi_u$ v'=3)4dσ_g $^1\Pi_u$, in order of increasing energy. The third member of the series, however, sticks out from the pattern in two

ways: it is the only one with a configuration of $5d\sigma_g$ rather than $4d\sigma_g$ and it breaks the pattern of increasing vibrational quantum number, v', incrementally by one. We show in Table 2.2 that the successive increase in isotope shifts measured and calculated for these peaks from the spectra presented here instead follows closely the isotope shifts calculated with Equation 2.1 for the first four vibrational levels of the A $^2\Pi_u$ state (i.e. v'=1, 2, 3, and 4 within the same electronic Rydberg configuration). We therefore favor assignment to the (A $^2\Pi_u$ v'=0)$4d\sigma_g$ $^1\Pi_u$, (A $^2\Pi_u$ v'=1)$4d\sigma_g$ $^1\Pi_u$, (A $^2\Pi_u$ v'=2)$4d\sigma_g$ $^1\Pi_u$, and (A $^2\Pi_u$ v'=3)$4d\sigma_g$ $^1\Pi_u$ states.

More generally, the measured isotope shifts for $^{15}N_2$ and the newly measured $^{15}N^{14}N$ should also be useful as benchmarks for theoretical calculations, including coupled-channel Schrödinger calculations [*Sprengers et al.*, 2003] and whether standard theories can account for the measured isotope-dependent changes in peak intensity or whether they may be governed by more complex, isotope-dependent quantum interference effects or quantum symmetry effects [*Sprengers et al.*, 2003, 2005; *Vieitez et al.*, 2008]. Indeed, Figures 2.3, 2.4 and 2.S5 also show an isotope effect in peak intensities, which does not follow a regular pattern like the peak energy trends do. For example, for some transitions all three isotopic species show the same transition intensity, while other transitions show either $^{15}N_2$ or $^{14}N_2$ having the strongest intensity. Our new measurements, when compared with theory, should contribute to a better understanding of how the interaction energies change between states that ultimately lead to photoionization for the different isotopologues [*Huber and Jungen*, 1990], as well as the nature of the interaction between the states involved and the ionization continuum. Our new data also provide motivation to measure higher resolution isotopic spectra near the cathedral peaks region to check whether our measured isotope effects in peak intensities are due to, for example, changes in Frank-Condon factors or mixing of states upon isotopic substitution versus how much could be due to differing isotope shifts in energy (and/or intensity) for some of the smaller intensity peaks underlying our 6 meV spectral bandwidth in this region. In a recent study by *Holland et al.* [2013], for example, it was suggested that the intermediate states in autoionization near the ionization threshold of N_2 may not be "pure" Rydberg states (i.e., they are perturbed by interactions with valence states) based on measured vibrational branching ratios for the N_2^+ product ion after autoionization which did not correspond with Franck-Condon factors between the presumed intermediate Rydberg state and the measured vibrational state of the ion. The isotope-specific ionization cross-sections presented here, in conjunction with isotope-specific vibrational branching ratios of N_2^+ after autoionization and isotope-specific Franck-Condon factors, can further clarify the nature of the states involved and help assess if and to what extent the Rydberg states in this region of the spectrum are perturbed by interactions with valence states.

In addition to providing new spectroscopic insights, the measured isotope effects also have potential astrophysical and geophysical applications to interstellar molecular clouds [*Terzieva and Herbst*, 2000; *Hily-Blant et al.*, 2013] and to planetary atmospheres on Earth [*Aikin*, 2001; *Kaye*, 1987], Mars [*Fox and Dalgarno*, 1980, 1983; *Fox*, 1993; *Fox and Hać*, 1997], and Titan [*Wilson and Atreya*, 2004; *Waite et al.*, 2007; *Imanaka and Smith*, 2010, 2007, 2009]. For example, in the atmospheres of both Earth and Titan, N_2 is the primary component and a major absorber of solar vacuum ultraviolet (VUV) radiation in the ionospheres of both bodies. Isotope effects in the photoionization of N_2 may potentially play a role in determining changes in the isotopic composition of N_2 over billions of years due to isotopic differences in the gravitational escape rates of nitrogen atoms [*Fox and Dalgarno*, 1980, 1983; *Fox*, 1993; *Fox and Hać*, 1997; *Lunine et al.*, 1999] and/or in affecting the isotopic composition of minor atmospheric species produced via reactions of N_2^+ on much shorter photochemical timescales, such as NO on Earth [*Aikin*, 2001] or

HCN on Titan [*Liang et al.*, 2007; *Croteau et al.*, 2011]. In a previous publication [*Croteau et al.*, 2011], we showed that the isotope shifts in peak energy and intensity in the N_2 photoionization spectrum, shown here in Figure 2.3, are large enough to cause isotope fractionation of species in planetary atmospheres under optically-thick conditions for $^{14}N_2$, leading to an enhancement in the photoionization rate constant of $^{15}N^{14}N$ relative to that for $^{14}N_2$ by as much as 17% -- smaller than that due to N_2 photodissociation but still potentially significant. We concluded that taking isotope effects in N_2 photoionization into account may thus contribute to a more quantitative understanding of the observed differences in the isotopic compositions of N_2 and HCN in Titan's atmosphere [*Marten et al.*, 2002; *Gurwell*, 2004; *Niemann et al.*, 2005; *Waite et al.*, 2005; *Vinatier et al.*, 2007].

2.5 Conclusions

We have presented isotope shifts for a number of transitions in the spectrum of N_2 above the ionization threshold, including those for $^{15}N^{14}N$, which have not been reported before. The isotope shifts we measured are used to address ambiguities in spectral peak assignments, including that for the second "cathedral" peak, which has remained controversial. The experimental isotope shifts for the second cathedral peak match most closely with those calculated for $(A\ ^2\Pi_u\ v'=2)4s\sigma_g\ ^1\Pi_u$, and we thus favor this assignment. More generally, the isotope shifts in both energy and intensity for $^{15}N_2$ and $^{15}N^{14}N$ relative to $^{14}N_2$ provide new experimental benchmarks for theoretical calculations and may yield a greater understanding of the quantum states involved and their interaction energies with one another and with the ionization continuum.

Table 2.1. Well-known peaks in the $^{14}N_2$ spectrum used in the energy scale calibration for $^{14}N_2$, $^{15}N_2$, and $^{15}N^{14}N$

Peak energy (eV)	Reference
15.6571	*Ogawa* [1964]
15.6764	
15.8773	
15.9806	
16.2098	
16.4383	
16.5854	
16.6787	
16.8120	
17.1507	*Ogawa and Tanaka* [1962]
17.8649	
18.1872	
18.3626	
18.4667	
18.5337	
18.5797	
18.6124	
18.6389	
18.6532	

Table 2.2. Selected spectral peaks from Figure 2.3 and their measured and calculated isotope shifts

Assignment	*Ogawa* [1964] designation	$^{14}N_2$	$^{15}N^{14}N$			$^{15}N_2$			
		Peak energy (eV)	Peak energy (eV)	Measured ΔE^a (eV)	Predicted ΔE^b (eV)	Peak energy (eV)	Measured ΔE^a (eV)	Predicted ΔE^b (eV)	*Ogawa* [1964] ΔE (eV)
(A $^2\Pi_u$ v'=2)4sσ_g $^1\Pi_g$	Unidentified[c]	15.6768	15.6688	0.0080±0.0003	0.0071	15.6618	0.0152±0.0003	0.0143	0.0169
(A $^2\Pi_u$ v'=2)3dσ_g $^1\Pi_u$	Unidentified[d]	15.8747	15.8666	0.0081±0.0006	0.0071	15.8581	0.0166±0.0007	0.0143	0.0185
(A $^2\Pi_u$ v'=0)4dσ_g $^1\Pi_u$	P(1) v'=0	15.9840	15.9819	0.0022±0.0005	-0.0005	15.9797	0.0043±0.0006	-0.0010	-0.0002
(A $^2\Pi_u$ v'=1)4dσ_g $^1\Pi_u$	P(1) v'=1	16.2094	16.2065	0.0029±0.0006	0.0034	16.2029	0.0065±0.0005	0.0068	0.0057
(A $^2\Pi_u$ v'=2)4dσ_g $^1\Pi_u$	P(1) v'=2	16.4386	16.4323	0.0063±0.0007	0.0071	16.4245	0.0140±0.0011	0.0143	0.0139
(A $^2\Pi_u$ v'=3)4dσ_g $^1\Pi_u$	P(1) v'=3	16.6616	16.6535	0.0080±0.0010	0.0106	16.6408	0.0208±0.0009	0.0215	0.0222
(A $^2\Pi_u$ v'=0)6dσ_g $^1\Pi_u$	P(2) v'=0	16.3529	16.3513	0.0016±0.0009	-0.0005	16.3493	0.0036±0.0009	-0.0010	0.0020
(A $^2\Pi_u$ v'=1)6dσ_g $^1\Pi_u$	P(2) v'=1	16.5836	16.5794	0.0042±0.0012	0.0034	16.5742	0.0094±0.0006	0.0068	0.0102
(A $^2\Pi_u$ v'=2)6dσ_g $^1\Pi_u$	P(2) v'=2	16.8130	16.8028	0.0102±0.0008	0.0071	16.7929	0.0202±0.0012	0.0143	0.0179

[a] Measured isotope shifts, ΔE, were determined by fitting the peaks in the $^{14}N_2$ spectrum and the corresponding peaks resulting from the same transition in the $^{15}N^{14}N$ or $^{15}N_2$ spectrum to Lorentzian profiles and taking the difference. All experimental runs were used. The reported uncertainties, which vary from ± 0.0003 to ± 0.0012 eV (1σ), are the statistical uncertainties resulting from the individual peak fitting uncertainties for each isotopologue for each run, the run-to-run peak energy variations after using a constant energy offset for each run, and propagation of error in taking the differences between the isotopologues.

[b] Predicted isotope shifts, ΔE, were calculated using Equation 2.1 from *Herzberg* [1950], where μ=7.0015 for $^{14}N_2$, μ_i=7.2422 for $^{15}N^{14}N$ and 7.5001 for $^{15}N_2$. For the X $^1\Sigma_g^+$ state, ω_e"=0.29243 eV and ω_e"x_e"=0.0017760 eV, and for the A $^2\Pi_u$ state, ω_e'=0.23601 eV and ω_e'x_e'=0.001861 eV [*Lofthus and Krupenie*, 1977].

[c] This transition (the second cathedral peak) was originally unidentified by [*Ogawa*, 1964] and has recently been given three different assignments by various investigators (see Tables 2.3 and 2.4). We favor the assignment listed here based on the measured and calculated isotope shifts.

[d] While this transition was not identified by *Ogawa* [1964], *Lefebvre-Brion and Yoshino* [1993] have since assigned it, and we follow their assignment here.

Table 2.3. Measured and predicted isotope shifts for the second cathedral peak at 15.677 eV

Proposed State Assignment	$E(^{14}N_2) - E(^{15}N^{14}N)$ (eV)	$E(^{14}N_2) - E(^{15}N_2)$ (eV)
$(A\ ^2\Pi_u\ v'=2)4s\sigma_g\ ^1\Pi_u$ [*McCormack et al.*, 1990]	0.0071[a]	0.0143[a]
$(A\ ^2\Pi_u\ v'=1)3d\sigma_g\ ^1\Pi_u$ [*Lefebvre-Brion and Yoshino*, 1993; *Lefebvre-Brion*, 2005a; b]	0.0034[a]	0.0068[a]
$b'\ ^1\Sigma_u^+\ v'=44$ [*Sommavilla et al.*, 2002; *Sommavilla and Merkt*, 2006]	--	0.035[b]
Measured (this work)[c]	**0.008 ± 0.001**	**0.015 ± 0.001**

[a] Calculated as detailed in Table 2.2 using Equation 2.1 from Herzberg.[*Herzberg*, 1950]
[b] Calculated by *Lefebvre-Brion* [2005a] by solving the coupled-channel Schrödinger equations for the relevant states: the b' valence state and two Rydberg states, c' ($X\ ^2\Sigma_g^+\ v'=0$)3pσ and e' ($X\ ^2\Sigma_g^+\ v'=0$)4pσ, using the parameters of *Spelsberg and Meyer* [2001] and using the Fox-Goodwin propagator with matching outgoing and ingoing solutions.
[c] See Section 2.2 for a discussion of the reported uncertainties.

Table 2.4. Previous assignments of the second cathedral peak at 15.677 eV in $^{14}N_2$.

Assignment	References	Evidence
(A $^2\Pi_u$ v'=2)4sσ_g $^1\Pi_u$	*McCormack et al.* [1990]	The transition showed high intensity when excited from the ground state of N_2 (X $^1\Sigma_g^+$ v"=0) but was not observed in double resonance spectra via the a $^1\Pi_g$ v"=5 state, indicating a low Franck-Condon factor for transitions from the a $^1\Pi_g$ v"=5 state.
(A $^2\Pi_u$ v'=1)3dσ_g $^1\Pi_u$	*Lefebvre-Brion and Yoshino* [1993]	The authors claim the transition assigned by *McCormack et al.* [1990] would be weak, in conflict with the strength of the peak at 15.677 eV. They therefore favor assignment to (A $^2\Pi_u$ v'=1)3dσ_g $^1\Pi_u$, which is expected to be intense.
	Lefebvre-Brion [2005a; b]	Ruling out the transition to b' $^1\Sigma_u^+$ v'=44: (1) The width of this peak is large (5 cm^{-1}; 6 x 10^{-4} eV) and more compatible with a calculated width for (A $^2\Pi_u$ v'=1)3dσ_g $^1\Pi_u$ of 27.8 cm^{-1} (3.45 x 10^{-3} eV) than that for b' $^1\Sigma_u^+$ v'=44 of 0.01 cm^{-1} (1.24 x 10^{-6} eV). (2) Coupled-channel Schrödinger equation calculations for transitions to the b' $^1\Sigma_u^+$ v'=44 state predict a rotational constant of 0.66 cm^{-1} (8.18 x 10^{-5} eV), which is incompatible with the experimentally derived value of 1.5 cm^{-1} (1.86 x 10^{-4} eV). (3) *McCormack et al.* [1990] observed transitions to the b' $^1\Sigma_u^+$ v'=42 and 43 states in the double resonance spectra; if this transition were to the b' $^1\Sigma_u^+$ v'=44 state, they should have observed this transition too but did not.
b' $^1\Sigma_u^+$ v'=44	*Sommavilla et al.* [2002]	Simulations of the peak width, shape, and height assuming $^1\Sigma_u^+$ symmetry gave significantly better agreement with experiment than simulations assuming $^1\Pi_u$ symmetry.
	Sommavilla and Merkt [2006]	More detailed simulations of the peak width, shape, and height showed that $^1\Pi_u$ symmetry gave a far less satisfactory match with measurements than simulations with $^1\Sigma_u^+$ symmetry. This transition is still considered "tentative," however, since a transition to a Rydberg state with $^1\Pi_u$ symmetry could still be viable if it were highly perturbed by channel coupling/mixing.

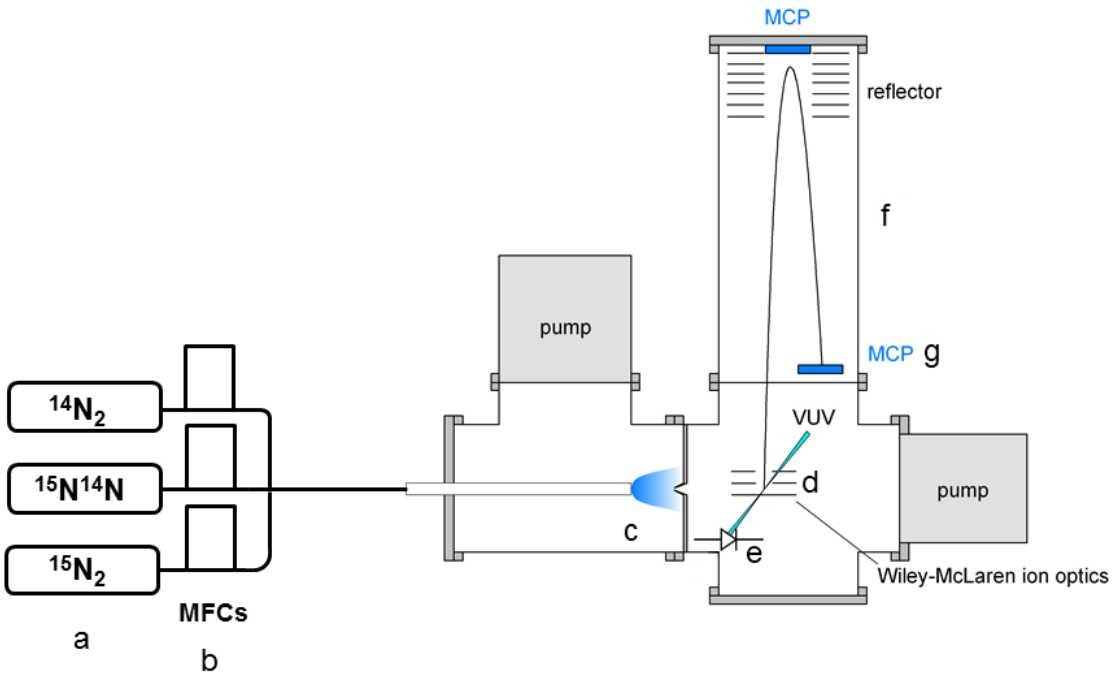

Figure 2.1. Schematic of the apparatus used to determine the relative photoionization cross-sections as a function of energy for the three isotopologues of N_2. The apparatus includes (a) source gas cylinders, (b) mass-flow controllers (MFCs), (c) supersonic expansion to form a molecular beam of N_2, (d) molecule-photon interaction region, (e) Si-photodiode for monitoring photon intensity throughout the experiment, (f) time-of-flight (TOF) tube, and (g) microchannel plate (MCP) detector.

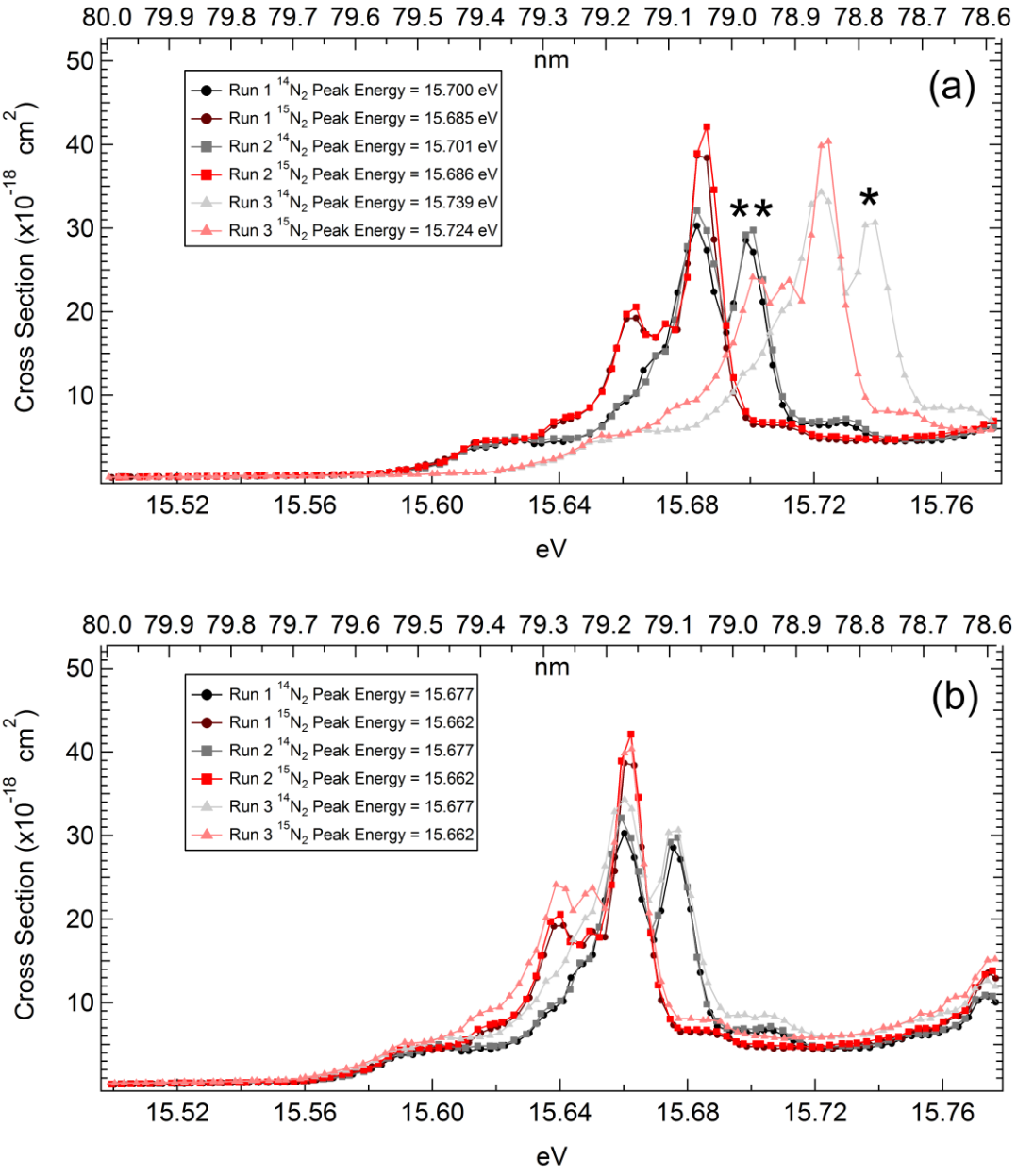

Figure 2.2. Photoionization spectra for $^{14}N_2$ and $^{15}N_2$ in individual experimental runs near 15.6 eV. (a) Data from three different runs for $^{14}N_2$ (gray) and $^{15}N_2$ (red) are shown as a function of monochromator reading; the peaks with asterisks result from the same spectroscopic transition but are displaced from run to run due to mechanical imprecision in the monochromator. (b) A constant was added to the energy scale of each of the three experimental runs such that the marked peaks were set to exactly 15.677 eV; the remaining spectral features then line up to within 1 meV. The 1σ standard deviation (N=3) of the resulting shifted energy of the second cathedral peak is 2.2 x 10^{-4} eV for $^{14}N_2$, 1.7 x 10^{-4} eV for $^{15}N^{14}N$, and 1.3 x 10^{-4} eV for $^{15}N_2$ (see text).

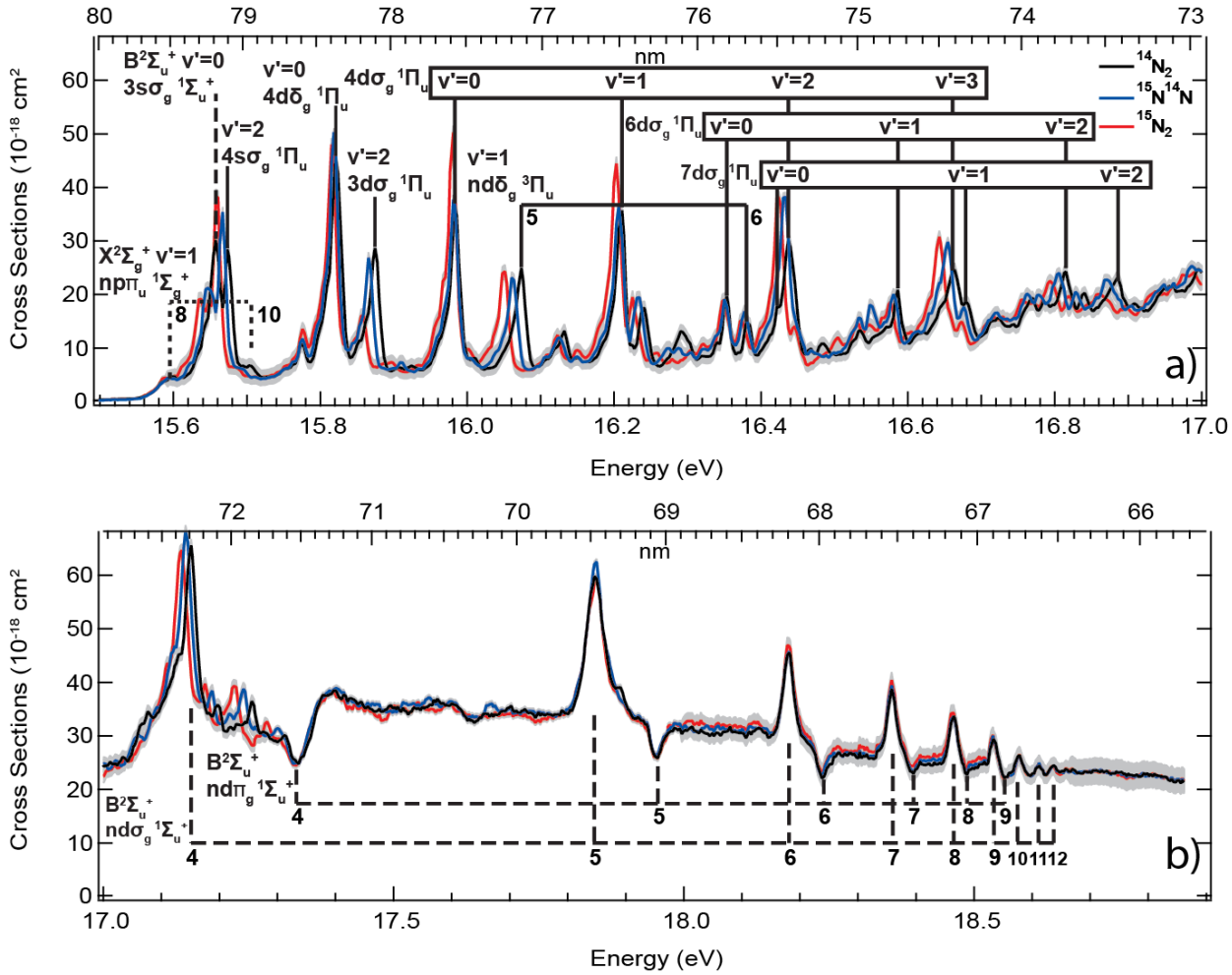

Figure 2.3. Photoionization efficiency spectra for $^{14}N_2$ (black line), $^{15}N^{14}N$ (blue line), and $^{15}N_2$ (red line). The shaded area represents the 1σ standard deviation of the average intensity of the two or three runs over each individual energy region (see Section 2.2). (a) Spectra for 15.5 – 17.0 eV and (b) Spectra for 17.0 – 18.9 eV. Most of the auto-ionizing Rydberg states belong to series that are converging to the A $^2\Pi_u$ state of N_2^+ and are marked with solid vertical lines. States from one series converging to the X $^2\Sigma_g^+$ state are marked with a dotted vertical line, and states from series converging to B $^2\Sigma_u^+$ are marked with dashed vertical lines.

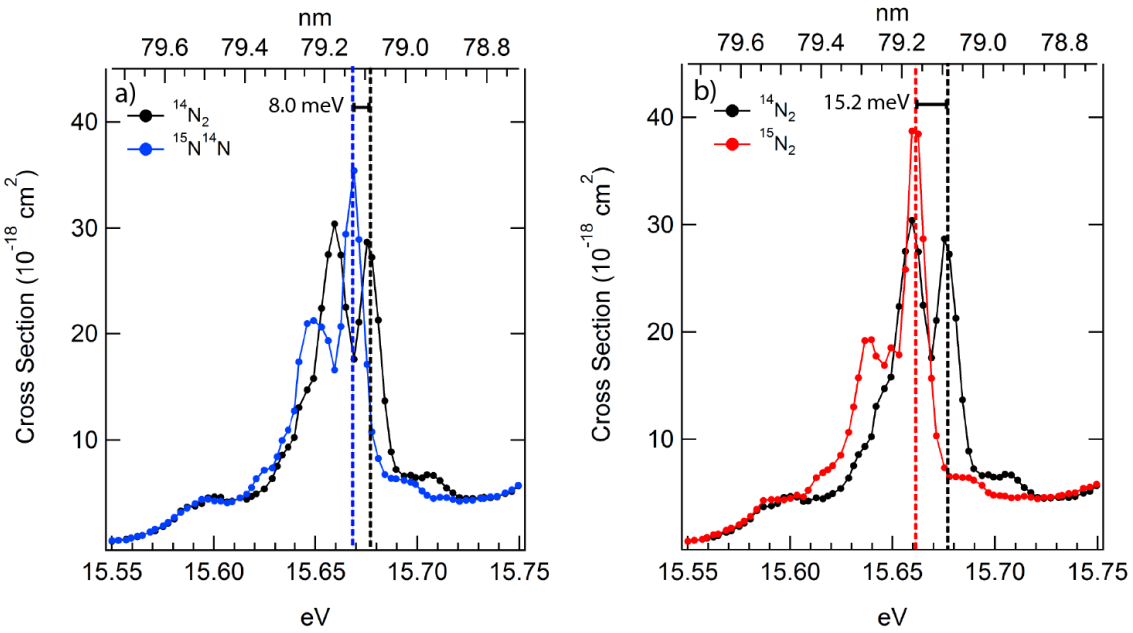

Figure 2.4. PIE spectra from 15.55 to 15.75 eV showing isotope shifts of the second cathedral peak of (a) 0.008 eV (8 meV) for $^{15}N^{14}N$ and (b) 0.015 eV (15 meV) for $^{15}N_2$. Dashed lines indicate peak centers based on Lorentzian-profile fits.

Aikin, A.C. (2001) Isotope identification in NO as a chemical tracer in the middle atmosphere, *Phys. Chem. Earth Part C-Sol.-Terrestial Planet. Sci.*, *26*, 527–532.

Aoiz, F.J., T. Diez-Rojo, V.J. Herrero, B. Martinez-Haya, M. Menendez, P. Quintana, L. Ramonat, I. Tanarro, and E. Verdasco (1999) Low-temperature rotational relaxation of N_2 studied with resonance-enhanced multiphoton ionization, *J. Phys. Chem. A*, *103*, 823–832, doi:10.1021/jp983850y.

Bayes, K.D., and G.B. Kistiakowsky (1960) On the mechanism of the Lewis-Rayleigh nitrogen afterglow, *J. Chem. Phys.*, *32*, 992–1000, doi:10.1063/1.1730909.

Berg, L.E., P. Erman, E. Kallne, S. Sorensen, and G. Sundstrom (1991) Studies of photoionization and photodissociation of N_2 in the 15-30 eV region using intense sychrotron radiation, *Phys. Scr.*, *44*, 131–137, doi:10.1088/0031-8949/44/2/003.

Burridge, J.C., and I.J. Hewitt (1984) Isotope shifts in the N_2($C\ ^3\Pi_u$-$B\ ^3\Pi_g$) Second Positive system, *Spectrochim. Acta Part B-At. Spectrosc.*, *39*, 605–608, doi:10.1016/0584-8547(84)80069-5.

Carroll, P.K., and D. Mahon-Smith (1963) Isotopic shifts in some ultraviolet systems of N_2, *J. Chem. Phys.*, *39*, 237–&, doi:10.1063/1.1734010.

Cook, G.R., and P.H. Metzger (1964) Photoionization and absorption cross sections of O_2 and N_2 in 600- to 100-Å region, *J. Chem. Phys.*, *41*, 321–&.

Cook, G.R., and M. Ogawa (1965) Photo-ionization of N_2 in 734-805 Å region, *Can. J. Phys.*, *43*, 256.

Cremaschi, P., A. Chattopadhyay, P.V. Madhavan, and J.L. Whitten (1986) A theoretical study of the Rydberg states of N_2 obtained from excitations of the valence $3\sigma_g$, $1\pi_u$, and $2\sigma_u$ levels, *Chem. Phys.*, *109*, 117–124.

Croteau, P., J.B. Randazzo, O. Kostko, M. Ahmed, M.C. Liang, Y.L. Yung, and K.A. Boering (2011) Measurements of isotope effects in the photoionization of N_2 and implications for Titan's atmosphere, *Astrophys. J. Lett.*, *728*.

Dehmer, P.M., P.J. Miller, and W.A. Chupka (1984) Photoionization of N_2 $X\ ^1\Sigma_g^+$, $v''=0$ and 1 near threshold. Preionization of the Worley-Jenkins Rydberg series, *J. Chem. Phys.*, *80*, 1030–1038.

Erman, P., E. Rachlew-Källne, and S.L. Sorensen (1994) Synchrotron radiation induced photoionization and photodissociation of carbon monoxide in the 14-35 eV region, *Z. Phys. -At. Mol. Clust.*, *30*, 315–321.

Fox, J.L. (1993) The production and escape of nitrogen atoms on Mars, *J. Geophys. Res.-Planets*, *98*, 3297–3310, doi:10.1029/92JE02289.

Fox, J.L., and A. Dalgarno (1980) Production of nitrogen atoms on Mars and their escape, *Planet. Space Sci.*, *28*, 41–46, doi:10.1016/0032-0633(80)90102-6.

Fox, J.L., and A. Dalgarno (1983) Nitrogen escape from Mars, *J. Geophys. Res.-Space Phys.*, *88*, 9027–9032, doi:10.1029/JA088iA11p09027.

Fox, J.L., and A. Hać (1997) The $^{15}N/^{14}N$ isotope fractionation in dissociative recombination of N_2^+, *J. Geophys. Res.-Planets*, *102*, 9191–9204.

Giusti-Suzor, A., and H. Lefebvre-Brion (1984) Theoretical study of complex resonances near ionization thresholds: Application to the N_2 photoionization spectrum, *Phys. Rev. A*, *30*, 3057–3065.

Gürtler, P., V. Saile, and E.E. Koch (1977) High resolution absorption spectrum of nitrogen in the vacuum ultraviolet, *Chem. Phys. Lett.*, *48*, 245–250.

Gurwell, M.A. (2004) Submillimeter observations of Titan: Global measures of stratospheric temperature, CO, HCN, HC_3N, and the isotopic ratios $^{12}C/^{13}C$ and $^{14}N/^{15}N$, *Astrophys. J.*, *616*, L7–L10, doi:10.1086/423954.

Hajim, K.I., and P.K. Carroll (1987) The calculation of the interaction energies of the $b'\ ^1\Sigma^+_u$ and $c'\ ^1\Sigma^+_u$ states of $^{15}N_2$, *J. Phys. B-At. Mol. Opt. Phys.*, *20*, 6233–6241, doi:10.1088/0022-3700/20/23/015.

Herzberg, G. (1950) Molecular Spectra and Molecular Structure. I. Spectra of Diatomic Molecules. Van Nostrand-Reinhold, New York.

Hily-Blant, P., L. Bonal, A. Faure, and E. Quirico (2013) The ^{15}N-enrichment in dark clouds and Solar System objects, *Icarus*, *223*, 582–590, doi:10.1016/j.icarus.2012.12.015.

Holland, D.M.P., E.A. Seddon, S. Daly, C. Alcaraz, C. Romanzin, L. Nahon, and G.A. Garcia (2013) The effect of autoionization on the $N_2^+\ X\ ^2\Sigma^+_g$ state vibrationally resolved photoelectron anisotropy parameters and branching ratios, *J. Phys. B-At. Mol. Opt. Phys.*, *46*, 095102, doi:10.1088/0953-4075/46/9/095102.

Huber, K.P., and C. Jungen (1990) High-resolution jet absorption study of nitrogen near 800 Å, *J. Chem. Phys.*, *92*, 850–861.

Imanaka, H., and M.A. Smith (2007) Role of photoionization in the formation of complex organic molecules in Titan's upper atmosphere, *Geophys. Res. Lett.*, *34*.

Imanaka, H., and M.A. Smith (2009) EUV photochemical production of unsaturated hydrocarbons: Implications to EUV photochemistry in Titan and jovian planets, *J. Phys. Chem. A*, *113*, 11187–11194.

Imanaka, H., and M.A. Smith (2010) Formation of nitrogenated organic aerosols in the Titan upper atmosphere, *Proc. Natl. Acad. Sci. U. S. A.*, *107*, 12423–12428.

Itikawa, Y., M. Hayashi, A. Ichimura, K. Onda, K. Sakimoto, K. Takayanagi, M. Nakamura, H. Nishimura, and T. Takayanagi (1986) Cross sections for collisions of electrons and photons with nitrogen molecules, *J. Phys. Chem. Ref. Data*, *15*, 985–1010.

Kaiser, R.I., P. Maksyutenko, C. Ennis, F. Zhang, X. Gu, S.P. Krishtal, A.M. Mebel, O. Kostko, and M. Ahmed (2010) Untangling the chemical evolution of Titan's atmosphere and surface from homogeneous to heterogeneous chemistry, *Faraday Discuss.*, *147*, 429–478, doi:10.1039/c003599h.

Kaye, J.A. (1987) Mechanisms and observations for isotope fractionation of molecular species in planetary atmospheres, *Rev. Geophys., 25*, 1609–1658.

Kosman, W.M., and S. Wallace (1985) Complete dipole oscillator strength distribution and its moments for N_2, *J. Chem. Phys., 82*, 1385–1399.

Kostko, O., L. Belau, K.R. Wilson, and M. Ahmed (2008) Vacuum-ultraviolet (VUV) photoionization of small methanol and methanol-water clusters, *J. Phys. Chem. A, 112*, 9555–9562.

Lefebvre-Brion, H. (2005a) Assignment in the near-threshold absorption spectrum of N_2, *J. Chem. Phys., 122*.

Lefebvre-Brion, H. (2005b) The "cathedral" in the near-threshold absorption spectrum of N_2, *J. Electron Spectrosc. Relat. Phenom., 144*, 109–111.

Lefebvre-Brion, H., and K. Yoshino (1993) Tentative interpretation of the Rydberg series converging to the $A^2\Pi_u$ state of N_2^+, *J. Mol. Spectrosc., 158*, 140–146.

Liang, M.-C., A.N. Heays, B.R. Lewis, S.T. Gibson, and Y.L. Yung (2007) Source of nitrogen isotope anomaly in HCN in the atmosphere of Titan, *Astrophys. J., 664*, L115–L118.

Lofthus, A., and P.H. Krupenie (1977) Spectrum of molecular nitrogen, *J. Phys. Chem. Ref. Data, 6*, 113–307.

Lunine, J.I., Y.L. Yung, and R.D. Lorenz (1999) On the volatile inventory of Titan from isotopic abundances in nitrogen and methane, *Planet. Space Sci., 47*, 1291–1303, doi:10.1016/S0032-0633(99)00052-5.

Mahon-Smith, D., and P.K. Carroll (1964) Isotope shifts and the vibrational structure in some weaker systems of N_2, *J. Chem. Phys., 41*, 1377–&, doi:10.1063/1.1726076.

Marten, A., T. Hidayat, Y. Biraud, and R. Moreno (2002) New millimeter heterodyne observations of Titan: Vertical distributions of nitriles HCN, HC_3N, CH_3CN, and the isotopic ratio $^{15}N/^{14}N$ in its atmosphere, *Icarus, 158*, 532–544, doi:10.1006/icar.2002.6897.

McCormack, E.F., S.T. Pratt, J.L. Dehmer, and P.M. Dehmer (1990) Double-resonance spectroscopy of autoionizing states of N_2 near the ionization threshold, *Phys. Rev. A, 42*, 5445–5451.

McCormack, E.F., S.T. Pratt, J.L. Dehmer, and P.M. Dehmer (1991) Analysis of the 8f, 9f, and 10f, v=1 Rydberg states of N_2, *Phys. Rev. A, 44*, 3007–3015.

McCormack, E.F., S.T. Pratt, P.M. Dehmer, and J.L. Dehmer (1992) Double-resonance spectroscopy of a complex resonance in molecular nitrogen, *Phys. Rev. A, 45*, 4697–4705.

McLean, W.J., and R.F. Sawyer (1974) Molecular-beam sampling from high-pressure sources, *Acta Astronaut., 1*, 523–540.

Mori, H., T. Niimi, I. Akiyama, and T. Tsuzuki (2005) Experimental detection of rotational non-Boltzmann distribution in supersonic free molecular nitrogen flows, *Phys. Fluids*, *17*, 117103, doi:10.1063/1.2130752.

Muskatel, B.H., F. Remacle, M.H. Thiemens, and R.D. Levine (2011) On the strong and selective isotope effect in the UV excitation of N_2 with implications toward the nebula and Martian atmosphere, *Proc. Natl. Acad. Sci. U. S. A.*, *108*, 6020–6025.

Nicolas, C., J.N. Shu, D.S. Peterka, M. Hochlaf, L. Poisson, S.R. Leone, and M. Ahmed (2006) Vacuum ultraviolet photoionization of C3, *J. Am. Chem. Soc.*, *128*, 220–226.

Niemann, H., S. Atreya, S. Bauer, G. Carignan, J. Demick, R. Frost, D. Gautier, J. Haberman, D. Harpold, D. Hunten, G. Israel, J. Lunine, W. Kasprzak, T. Owen, M. Paulkovich, F. Raulin, E. Raaen, and S. Way (2005) The abundances of constituents of Titan's atmosphere from the GCMS instrument on the Huygens probe, *Nature*, *438*, 779–784, doi:10.1038/nature04122.

O'Keeffe, P., P. Bolognesi, A. Moise, R. Richter, Y. Ovcharenko, and L. Avaldi (2012) Vibrationally resolved photoionization of N_2 near threshold, *J. Chem. Phys.*, *136*, 104307.

Ogawa, M. (1964) Vibrational isotope shifts of absorption bands of N_2 in spectral region 720-830 Å, *Can. J. Phys.*, *42*, 1087.

Ogawa, M., A.S. Jursa, and Y. Tanaka (1964) Isotope shift of nitrogen absorption bands in vacuum ultraviolet region, *Can. J. Phys.*, *42*, 1716.

Ogawa, M., and S. Ogawa (1972) Absorption spectrum of CO in the Hopfield heliium continuum region, 600-1020 Å, *J. Mol. Spectrosc.*, *41*, 393, doi:10.1016/0022-2852(72)90212-3.

Ogawa, M., and Y. Tanaka (1962) Rydberg absorption series of N_2, *Can. J. Phys.*, *40*, 1593.

Samson, J.A.R., G.N. Haddad, and J.L. Gardner (1977) Total and partial photoionization cross-sections of N_2 from threshold to 100 Å, *J. Phys. B-At. Mol. Opt. Phys.*, *10*, 1749–1759.

Shaw, D.A., D.M.P. Holland, M.A. MacDonald, A. Hopkirk, M.A. Hayes, and S.M. McSweeney (1992) A study of the absolute photoabsorption cross-section and the photoionization quantum efficiencty of nitrogen from the ionization threshold to 485 Å, *Chem. Phys.*, *166*, 379–391, doi:10.1016/0301-0104(92)80097-F.

Sommavilla, M., U. Hollenstein, G.M. Greetham, and F. Merkt (2002) High-resolution laser absorption spectroscopy in the extreme ultraviolet, *J. Phys. B-At. Mol. Opt. Phys.*, *35*, 3901–3921.

Sommavilla, M., and F. Merkt (2006) On the rotational structure of a prominent band in the vacuum-ultraviolet spectrum of molecular nitrogen, *J. Electron Spectrosc. Relat. Phenom.*, *151*, 31–33.

Spelsberg, D., and W. Meyer (2001) Dipole-allowed excited states of N_2: Potential energy curves, vibrational analysis, and absorption intensities, *J. Chem. Phys.*, *115*, 6438–6449.

Sprengers, J.P., W. Ubachs, and K.G.H. Baldwin (2005) Isotopic variation of experimental lifetimes for the lowest $^1\Pi_u$ states of N_2, *J. Chem. Phys.*, *122*.

Sprengers, J.P., W. Ubachs, K.G.H. Baldwin, B.R. Lewis, and W.-Ü.L. Tchang-Brillet (2003) Extreme ultraviolet laser excitation of isotopic molecular nitrogen: The dipole-allowed spectrum of $^{15}N_2$ and $^{14}N^{15}N$, *J. Chem. Phys.*, *119*, 3160–3173.

Stahel, D., M. Leoni, and K. Dressler (1983) Non-adiabatic representations of the $^1\Sigma_u^+$ and $^1\Pi_u$ states of the N_2 Molecule, *J. Chem. Phys.*, *79*, 2541–2558.

Terzieva, R., and E. Herbst (2000) The possibility of nitrogen isotopic fractionation in interstellar clouds, *Mon. Not. R. Astron. Soc.*, *317*, 563–568.

Vieitez, M.O., T.I. Ivanov, C.A. de lange, W. Ubachs, A.N. Heays, B.R. Lewis, and G. Stark (2008) Interactions of the $3p\pi_u$ $c^1\Pi_u(v=2)$ Rydberg-complex member in isotopic N_2, *J. Chem. Phys.*, *128*.

Vinatier, S., B. Bezard, and C.A. Nixon (2007) The Titan $^{14}N/^{15}N$ and $^{12}C/^{13}C$ isotopic ratios in HCN from Cassini/CIRS, *Icarus*, *191*, 712–721, doi:10.1016/j.icarus.2007.06.001.

Waite, J.H., H. Niemann, R.V. Yelle, W.T. Kasprzak, T.E. Cravens, J.G. Luhmann, R.L. McNutt, W.-H. Ip, D. Gell, V. De La Haye, I. Muller-Wordag, B. Magee, N. Borggren, S. Ledvina, G. Fletcher, E. Walter, R. Miller, S. Scherer, R. Thorpe, J. Xu, B. Block, and K. Arnett (2005) Ion Neutral Mass Spectrometer results from the first flyby of Titan, *Science*, *308*, 982–6.

Waite, J.H., D.T. Young, T.E. Cravens, A.J. Coates, F.J. Crary, B. Magee, and J. Westlake (2007) The process of tholin formation in Titan's upper atmosphere, *Science*, *316*, 870–875.

Wilson, E.H., and S.K. Atreya (2004) Current state of modeling the photochemistry of Titan's mutually dependent atmosphere and ionosphere, *J. Geophys. Res.-Planets*, *109*.

Yoshino, K., and Y. Tanaka (1977) High resolution vuv absorption spectrum of N_2, homogeneous perturbation between $c'(0)$ $^1\Sigma^+_u$ and $b'(1)$ $^1\Sigma^+_u$ levels, *J. Mol. Spectrosc.*, *66*, 219–232, doi:10.1016/0022-2852(77)90212-0.

Yoshino, K., Y. Tanaka, P.K. Carroll, and P. Mitchell (1975) High resolution absorption spectrum of N_2 in the vacuum-uv region, $o_{3,4}$ $^1\Pi_u \leftarrow X\ ^1\Sigma_g^+$ bands, *J. Mol. Spectrosc.*, *54*, 87–109, doi:10.1016/0022-2852(75)90011-9.

Supplementary figures

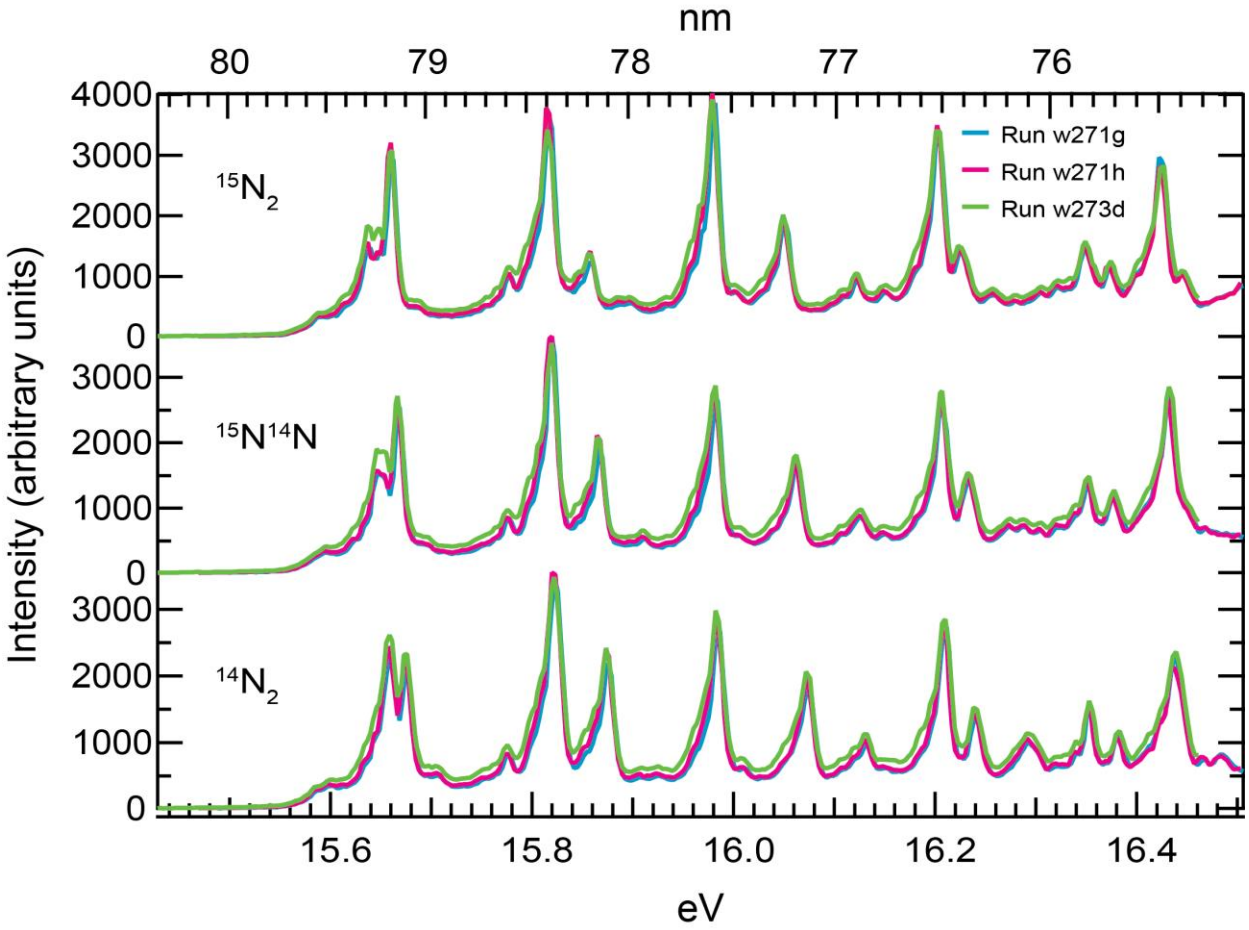

Figure 2.S1. Three experimental runs measuring the photoionization efficiency spectra of $^{14}N_2$, $^{15}N^{14}N$, and $^{15}N_2$ from 15.5 eV to 16.5 eV. The plotted data are available digitally in supplementary text files.

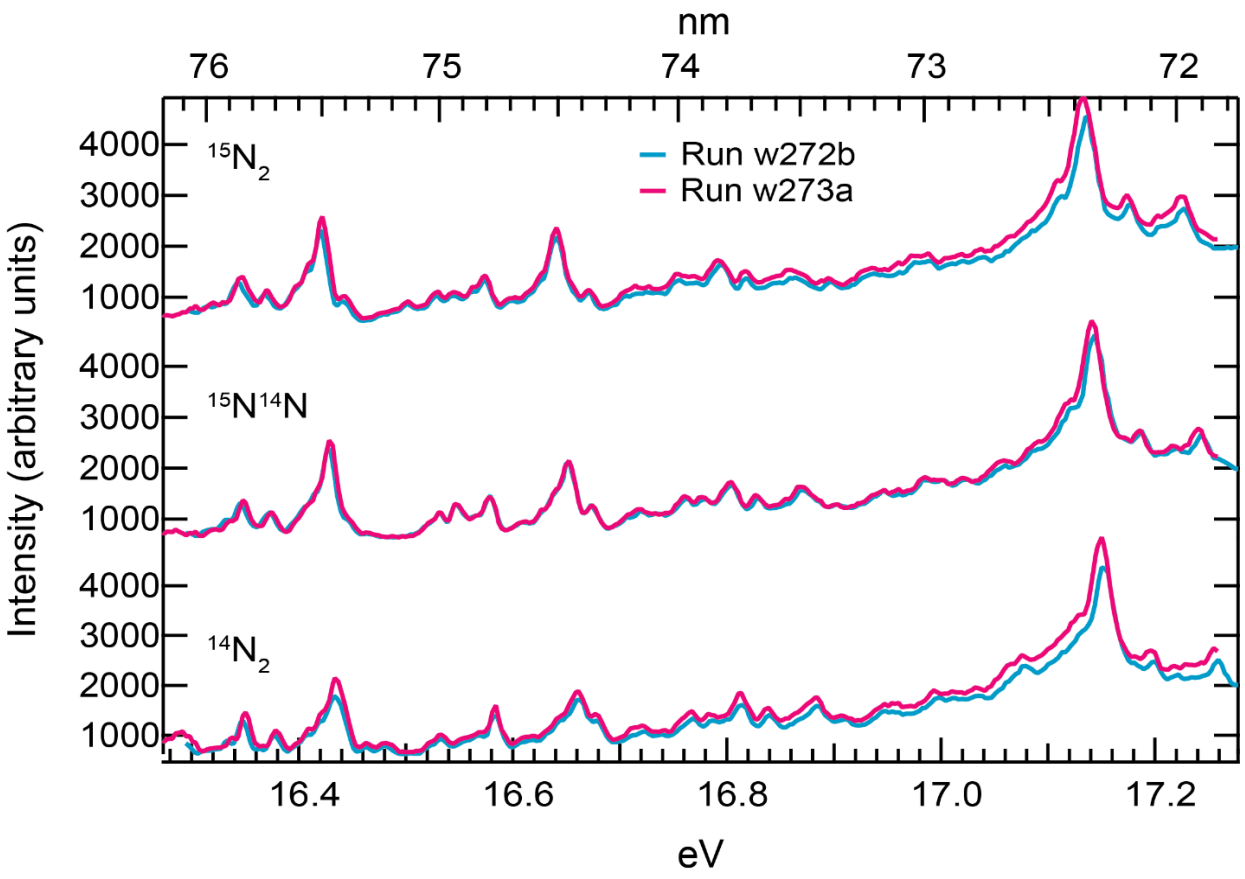

Figure 2.S2. Two experimental runs measuring the photoionization efficiency spectra of $^{14}N_2$, $^{15}N^{14}N$, and $^{15}N_2$ from 16.35 eV to 17.3 eV. The plotted data are available digitally in supplementary text files.

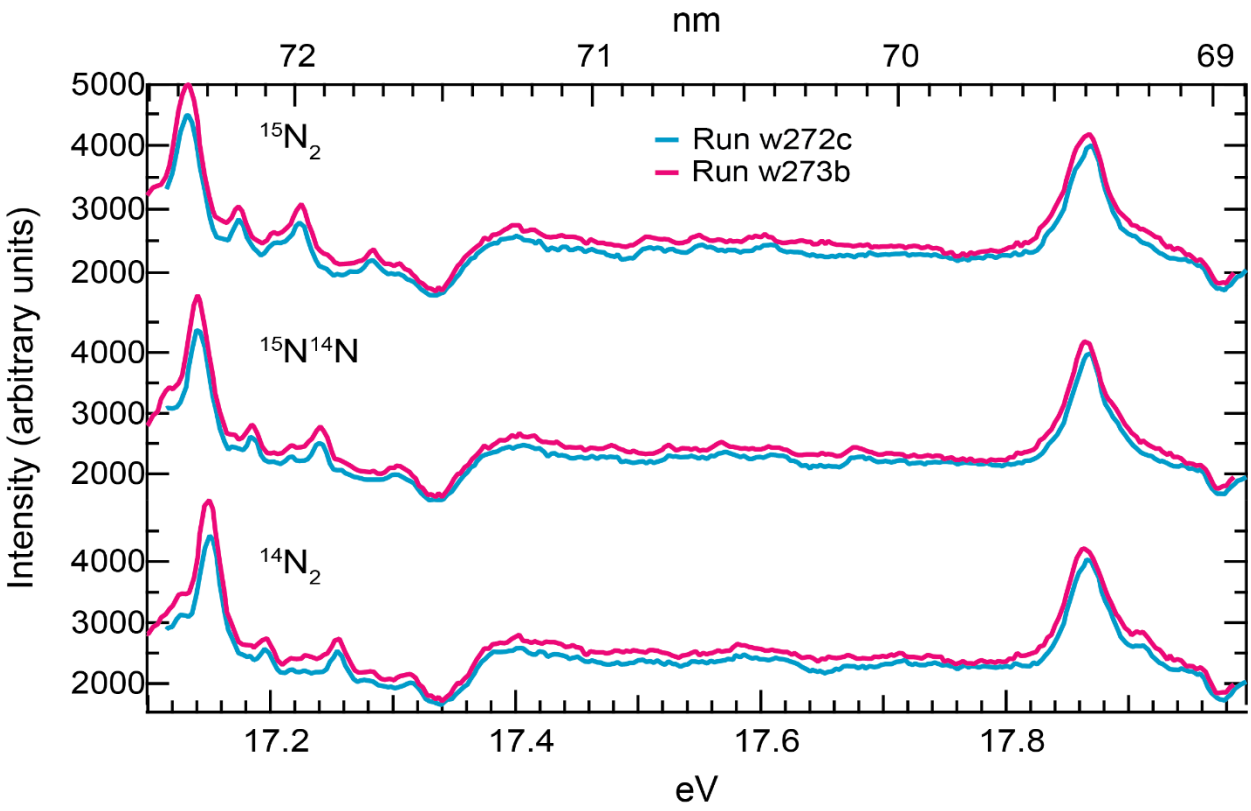

Figure 2.S3. Two experimental runs measuring the photoionization efficiency spectra of $^{14}N_2$, $^{15}N^{14}N$, and $^{15}N_2$ from 17.15 eV to 18.0 eV. The plotted data are available digitally in supplementary text files.

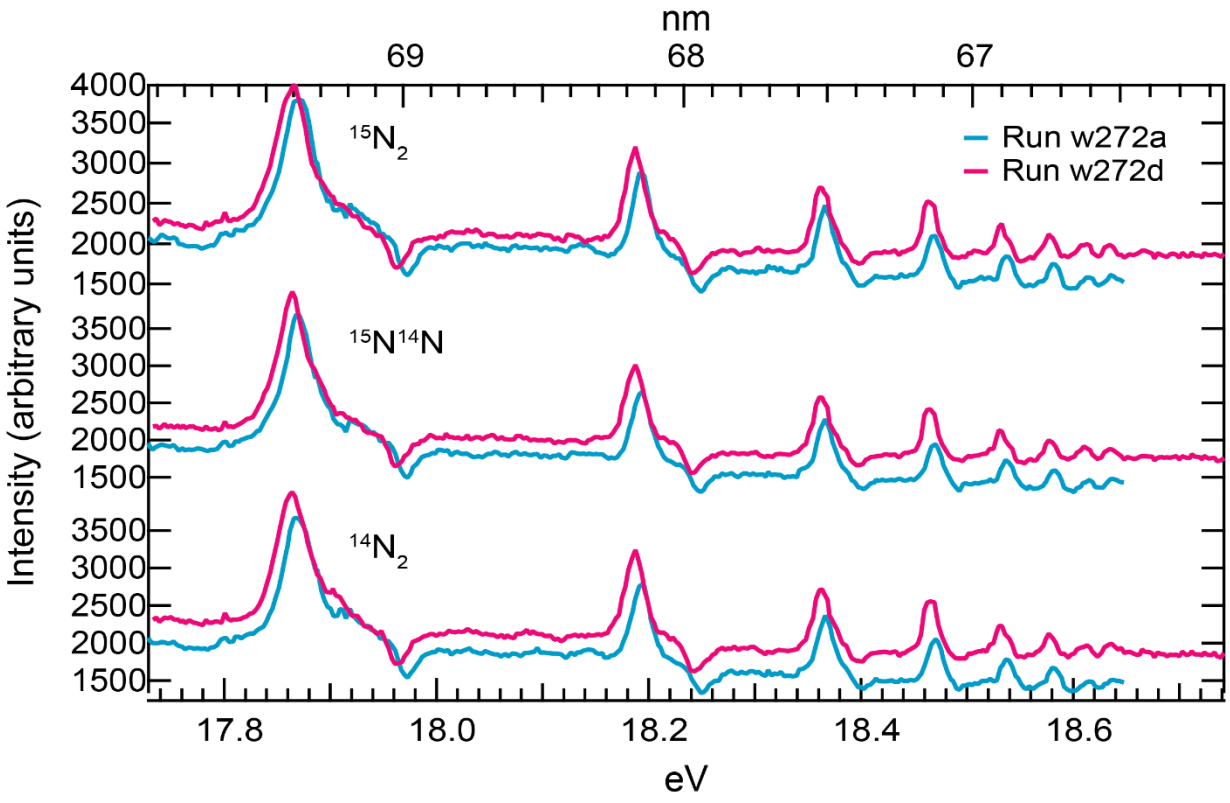

Figure 2.S4. Two experimental runs measuring the photoionization efficiency spectra of $^{14}N_2$, $^{15}N^{14}N$, and $^{15}N_2$ from 17.75 eV to 18.9 eV. The plotted data are available digitally in supplementary text files.

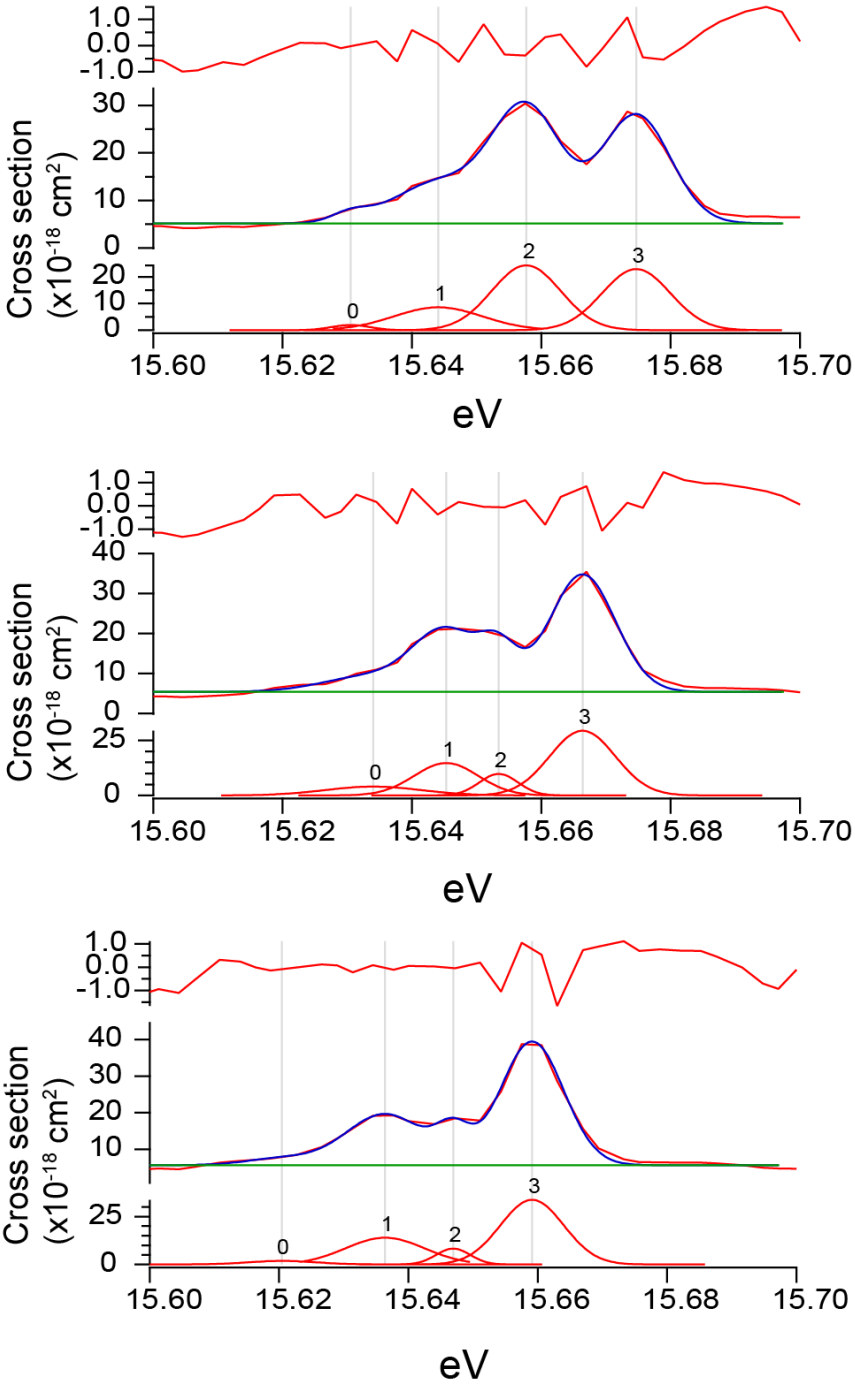

Figure 2.S5. Photoionization spectra of $^{14}N_2$, $^{15}N^{14}N$, and $^{15}N_2$ in the energy region containing the cathedral peaks, along with the peak fitting analysis from Igor Pro. Data shown here are from the run labeled 'w271g' in the supplementary digital data files. The top panels show the residuals (red); the middle panels show the experimental data (red) and their fits (blue); and the bottom panels show the deconvolved fitted peaks. Chi-squared values for the overall fits in this multiple peak region are 9.05 for $^{14}N_2$, 11.12 for $^{15}N^{14}N$, and 9.45 for $^{15}N_2$.

Chapter 3

Measurements of isotope effects in the non-dissociative photoionization of CO_2 and applications to spectroscopy and planetary atmospheres

3.1 Introduction

Isotopic substitution can result in measureable changes in absorption spectra, reaction rates, and atmospheric escape velocities, which can in turn lead to measurable differences in the relative abundances of the isotopologues of an atmospheric species in a planetary atmosphere on both short and long timescales. As a result, studying the isotopic composition of atmospheric species through ground-based, satellite, and *in situ* measurements, for example, can be an important tool in investigating a planetary atmosphere – from discovering its basic composition, to inferring current rates of radiative transfer and photochemical processes as well as the evolution of its composition over time. While some examples of how isotope effects in the photoionization of N_2 are applicable to the photochemistry and the history of the dense atmosphere on Saturn's moon, Titan, were discussed in *Croteau et al.* [2011] and in Chapter 2 of this dissertation, this chapter focuses on isotope effects in the photoionization of CO_2, a common component of the atmospheres of terrestrial planets.

Several recent discoveries for both Mars and Venus – both CO_2-rich atmospheres – provide motivation for a better understanding of the isotopic composition of CO_2 in planetary atmospheres and how it may have changed over time. In the first example, a new atmospheric absorption band was discovered on Mars (via ground based measurements [*Villanueva et al.*, 2008]) and on Venus (via solar occultation measurements by the Venus Express satellite [*Bertaux et al.*, 2008]), which corresponds to a transition of the $\nu_2+\nu_3$ combination vibrational transition for $^{12}C^{16}O^{18}O$. This isotopic band is important for two reasons: (1) the location of this band overlaps with absorption bands for C-H stretches; thus, the magnitude of absorption by $^{12}C^{16}O^{18}O$ must be accounted for in order to accurately detect trace organics in planetary atmospheres, such as CH_4 and C_2H_6, which in some cases may serve as organic biomarkers [*Villanueva et al.*, 2008]; and (2) the location and strength of this isotopic CO_2 band are important in determining the magnitude of the greenhouse effect from CO_2 in CO_2-rich atmospheres [*Villanueva et al.*, 2008]. A second example is recent *in situ* measurements of the isotopic composition of CO_2 from the martian rover, Curiosity, by the tunable diode laser [*Webster et al.*, 2013] and the quadrupole mass spectrometer [*Mahaffy et al.*, 2013] instruments in the Sample Analysis at Mars (SAM) suite. These measurements show that CO_2 is enriched in ^{13}C, more so than most previous measurements from, e.g., the Phoenix lander, by the Viking spacecraft, and by Earth telescopes had indicated [e.g., *Niles et al.*, 2010, 2013]. Such isotopic enrichment in CO_2 is more consistent with theories of atmospheric loss over time (which leaves remaining gases in the atmosphere enriched relative to the lighter isotopes which escape more easily) [e.g., *McElroy et al.*, 1976; *Owen et al.*, 1988; *Niles et al.*, 2013]. Together, these two examples show that understanding the isotopic composition of CO_2 in a planetary atmosphere and what processes determine it provide important constraints on atmospheric radiative transfer, the ability to detect other species, and on the history of their atmospheres, provided that the sign and magnitude of the isotope effects for all the underlying processes are known.

Of particular relevance to this study, we note that isotope effects in the photoionization of CO_2 have not been measured, so it is not known to what extent possible isotope effects in the photoionization of CO_2 might contribute to enrichments in ^{13}C and ^{18}O in CO_2 on Mars, Venus, or

Earth. Isotope effects in photoionization could potentially affect the isotopic composition of CO_2 directly by preferentially ionizing the light (or heavy) isotopologues, thereby isotopically enriching (or depleting) the CO_2 remaining in the atmosphere. Isotope effects in CO_2 photoionization might also affect the isotopic composition of CO_2 remaining in the atmosphere on longer timescales by further skewing the differences in the isotopologues which have enough energy to escape the atmosphere. Specifically, atmospheric escape can occur when the velocity of an atom or molecule is greater than the escape velocity at the exobase, the level of the atmosphere above which the mean free path of a molecule is greater than the scale height; many thermal and non-thermal processes can contribute to these high velocities, including photodissociation, photoionization, dissociative recombination, sputtering, ion pickup by solar wind, collisions of ions and molecules, and others (See, for example, the review by *Lammer et al.* [2008]). Significant isotopic fractionation may occur during atmospheric escape due to diffusive separation between the homopause (above which the scale height of a molecule is based on mass, instead of the scale height of all molecules being equal due to turbulent mixing), and exobase, thus enhancing the loss rate of lighter species via all loss processes (see, e.g., *Fox and Haćˊ* [1997], *Lammer et al.* [2008], *Gillmann et al.* [2011], and references therein). Isotope effects in the processes that produce these high velocity species could thus further enhance the isotopic fractionation. For example, isotope effects in photoionization ($AB + h\nu \rightarrow AB^+ + e^-$) could further increase isotopic fractionation by atmospheric escape since a number of atmospheric loss processes involve ions – e.g., dissociative recombination [*Fox and Haćˊ*, 1997; *Fox and Paxton*, 2005; *Fox and Haćˊ*, 2010], ion pickup by solar wind [*Fox*, 1997, 2009], sputtering [*Krasnopolsky et al.*, 2007], and collisions of ions and molecules (for a review of several nonthermal loss processes, see *Lammer et al.* [2008], *Dubinin et al.* [2011], *Gillmann et al.* [2011], and *Lammer et al.* [2013]). Since isotope effects in the photoionization of CO_2 have not been previously reported, the extent to which they might contribute to determining the isotopic composition of CO_2 on Mars and Venus today and how this may or may not have changed over the history of the solar system has not been estimated.

Another phenomenon that can lead to isotopic fractionation in a planetary atmosphere is self-shielding, which occurs when the atmosphere is optically thick for the common isotopologue ($^{12}C^{16}O_2$ in the case of CO_2) but not for the rare isotopologues (e.g., $^{13}C^{16}O_2$ and $^{12}C^{16}O^{18}O$), thus allowing photoionization or photodissociation of the rare isotopologues to continue to much lower altitudes [e.g., *Clayton*, 2002; *Yurimoto and Kuramoto*, 2004; *Lyons and Young*, 2005; *Lyons*, 2007; *Ono et al.*, 2013]. We previously showed [*Croteau et al.*, 2011] that self-shielding in N_2 photoionization leads to a ratio of photoionization rate coefficients $J(^{15}N^{14}N) / J(^{14}N_2)$ as high as 1.17 in Titan's atmosphere and that these isotopic differences may be important for resolving previous conundrums in understanding the differences in isotopic compositions measured for HCN [*Marten et al.*, 2002; *Gurwell*, 2004] versus those for N_2 [*Niemann et al.*, 2005; *Waite et al.*, 2005; *Vinatier et al.*, 2007]. The degree of self-shielding depends on how sharp the transitions are and how isolated the isotopic bands are from each other [e.g., *Lyons*, 2007, 2008]. As noted above, isotope effects in the photoionization of CO_2 have not been previously reported, so the extent to which self-shielding may affect the isotopic composition of CO_2 in planetary atmospheres has also not yet been estimated.

In addition to applications to planetary atmospheres, measured isotope effects in the photoionization spectra of CO_2 will be useful in addressing remaining uncertainties in the spectroscopic assignments just above the ionization threshold at 13.7 eV, similar to the advances presented and discussed in Chapter 2 for N_2. The photoionization spectra for $^{12}C^{16}O_2$, $^{13}C^{16}O_2$, $^{12}C^{16}O^{18}O$, $^{13}C^{16}O^{18}O$, $^{12}C^{18}O_2$, and $^{13}C^{18}O_2$, which are reported here for the first time, may also

prove to be useful as benchmarks for theoretical calculations to, for example, provide new constraints on how different states of CO_2 above the ionization threshold mix together and interact with the ionization continuum.

In this chapter, measurements of the photoionization efficiency (PIE) spectra for CO_2 isotopologues made using synchrotron radiation at the Advanced Light Source (ALS) from 13.7 eV to 20 eV are reported, including the first reported PIE measurements for $^{13}C^{16}O_2$, $^{12}C^{16}O^{18}O$, $^{13}C^{16}O^{18}O$, $^{12}C^{18}O_2$, and $^{13}C^{18}O_2$. The experimental setup used at the ALS is described in Section 3.2, along with methods for calibrating the intensity and energy scales of the measured spectra; results are discussed in Section 3.3, including an accompanying discussion of spectroscopic and atmospheric applications; and a brief summary is provided in Section 3.4.

3.2 Methods

Photoionization efficiency spectra for $^{12}C^{16}O_2$, $^{13}C^{16}O_2$, $^{12}C^{16}O^{18}O$, $^{13}C^{16}O^{18}O$, $^{12}C^{18}O_2$, and $^{13}C^{18}O_2$ were obtained using synchrotron radiation at the Chemical Dynamics Beamline at the Advanced Light Source using the experimental setup shown in Figure 3.1. Two source cylinders were used to create the CO_2 gas mixture used during the experiment. One cylinder contained natural abundance CO_2 (99.99% pure; Praxair, Danbury, CT), which is comprised of ~99% $^{12}C^{16}O_2$, ~1% $^{13}C^{16}O_2$, and ~0.2% $^{12}C^{16}O^{18}O$. The second cylinder (Spectra Gases, Stewartsville, NJ) contained CO_2 isotopically enriched in ^{18}O, stated by the manufacturer as "85% ^{18}O CO_2." Based on our spectra (see below), 69% of the CO_2 in the cylinder was $^{12}C^{18}O_2$, with smaller proportions of $^{12}C^{16}O^{18}O$ (26%), $^{13}C^{18}O_2$ (3%), $^{13}C^{16}O^{18}O$ (1%), and $^{12}C^{16}O_2$ (1%). Gases flowing from the two source cylinders were controlled through two calibrated mass-flow controllers ("MFCs"; Model 1179, 10 sccm full range, 1% full scale accuracy, MKS Instruments, Andover, MA) each set to a flow rate of 5 sccm and joined together with a T-fitting. Next, the mixture was expanded into a vacuum chamber through a 100 μm diameter orifice and passed through a 2 mm skimmer forming a collimated molecular beam. Vacuum ultraviolet (VUV) light from the synchrotron was first monochromatized with a bandwidth of 6 meV FWHM and then passed through a He-gas filter. The gas filter consisted of 4.5″ long tubing filled to ~30 Torr with He, which strongly absorbs light from higher harmonics generated by the undulator of the beamline. The filtered VUV light then intersected the molecular beam of CO_2. The intensity of the VUV beam was monitored throughout the experiment with a NIST-calibrated Si-photodiode.

The CO_2 molecules ionized by the VUV light were directed to a time-of-flight mass spectrometer using Wiley-McLaren ion optics pulsed at 30 kHz. The potential applied to the ion optics imparted different velocities to each species with different mass-to-charge ratios, which were then separated in the time-of-flight tube and detected with a microchannel plate with a multichannel-scaler card and then integrated with a PC. The peaks corresponding to $^{12}C^{16}O_2^+$, $^{13}C^{16}O_2^+$, $^{12}C^{16}O^{18}O^+$, $^{13}C^{16}O^{18}O^+$, $^{12}C^{18}O_2^+$, and $^{13}C^{18}O_2^+$ were each integrated for each 3 meV energy step.

Individual experimental runs (which took about 1 hour to acquire) were limited to approximately 1 eV (with each 1 eV energy region measured once) due to file size limitations of the PC used for data acquisition, and therefore had to be "stitched" together to create a single dataset ranging from 13.7 eV to 20.0 eV, which involved several steps. First, the intensity scale was normalized by the measured photon flux recorded by the Si-photodiode at each 3 meV energy step. Then, the intensity scales for individual runs, which varied from run to run due to small differences in detector efficiency, were normalized to the runs adjacent in energy in order to put all runs on the same intensity scale. By design, each 1 eV run contained some measurements which

overlapped with the adjacent energy regions. Starting with the lowest energy run (i.e., the run starting at 13.7 eV), each run and any runs at lower energies were normalized to the maximum intensity measured in the range of data overlapping with the next highest energy run, thus forcing the runs to the same intensity scale. The overlapping data from the higher energy run was then removed, and the process repeated until all runs were on a self-consistent intensity scale.

Once the intensity scales were normalized and the runs were combined, the energy scale was then calibrated due to concern that the limited mechanical precision of the monochromator and/or a possible compression or expansion of the experimentally measured energy scale (for example, if the energy step size was inaccurately recorded during the experiment) could lead to inaccuracies in the reported energy scale. The first step in calibrating the energy scale was to select several prominent peaks in the measured spectrum and to fit them to Lorentz profiles using the Multi-Peak Fit package in Igor Pro (version 6.3; WaveMetrics, Lake Oswego, OR). The second step was to compare the peak energies from the Lorentz fit with the peak energies reported by *Tanaka and Ogawa* [1962] (and shown here in Table 3.1), and a linear regression of our experimental energies versus the *Tanaka and Ogawa* [1962] energies was then used to convert the experimental energy scale to that reported by *Tanaka and Ogawa* [1962].

Because each isotopologue of CO_2 in the gas mixture had a different mixing ratio, the intensity for each isotopologue mass-to-charge ratio was also scaled by its mixing ratio (i.e., the relative proportion of an individual gas in the overall mixture). To estimate the mixing ratio of each CO_2 isotopologue, the intensity for each isotopologue was integrated over the full spectral range, and divided by the total for all isotopologues, resulting in mixing ratios of 0.475 for $^{12}C^{16}O_2$, 0.010 for $^{13}C^{16}O_2$, 0.134 for $^{12}C^{16}O^{18}O$, 0.016 for $^{13}C^{16}O^{18}O$, 0.360 for $^{12}C^{18}O_2$, and 0.006 for $^{13}C^{18}O_2$ (mixing ratios are also given in Table 3.2). The calculated mixing ratios are consistent with the approximately equal flow rates from the two source cylinders: $^{12}C^{16}O_2$ and $^{13}C^{16}O_2$ came mostly from the cylinder of natural abundance CO_2 (Praxair) and have a combined mixing ratio of 0.485, while $^{12}C^{16}O^{18}O$, $^{13}C^{16}O^{18}O$, $^{12}C^{18}O_2$, and $^{13}C^{18}O_2$ came mostly from the second cylinder of isotopically labeled CO_2 (Spectra Gases) and have a combined mixing ratio of 0.516. This procedure for determining the mixing ratio of each isotopologue differs from the approach taken in the spectra of N_2 discussed in Chapter 2, where the "flat" regions of the spectra were used to empirically derive the mixing ratios. The spectrum of CO_2 does not have any obvious "flat" regions, and so the entire spectral range was used instead.

3.3 Results and Discussion

Figure 3.2 shows the measured photoionization efficiency spectra for $^{12}C^{16}O_2$, $^{12}C^{16}O^{18}O$, and $^{12}C^{18}O_2$, whereas Figure 3.3 shows the spectra of all six isotopologues measured – those shown in Figure 3.2 with $^{13}C^{16}O_2$, $^{13}C^{16}O^{18}O$, and $^{13}C^{18}O_2$ added. The intensity scales for Figures 3.2 and 3.3 are in arbitrary units, with the intensity for each isotopologue normalized (1) by the experimentally measured photon flux, (2) sequentially by the highest intensity in regions of overlapping data during the "stitching together" procedure, and (3) by the mixing ratio for each isotopologue. Much like the photoionization spectrum of N_2 discussed in Chapter 2, the photoionization spectrum of CO_2 shows multiple progressions or series of peaks beginning just above the ionization threshold at 13.7 eV related by a sequential increase in principle quantum number (n) or vibrational quantum number (v′) of the final state in the transition. In Figure 3.2, we have followed the peak labeling used by *Shaw et al.* [1995] in their photoionization efficiency spectrum obtained with synchrotron radiation, which includes several series of peaks named for the authors that first reported them for the $^{12}C^{16}O_2$ spectrum, some of them over 50 years ago, (e.g.,

the Tanaka-Ogawa series and the Lindholm series) as well as other series which do not have a conventional "name" associated with them (e.g., "bent valence state" and "unidentified Rydberg state"). However, despite a long history of experimental and theoretical studies, the CO_2 PIE spectrum still has many peaks for which the assignment has remained uncertain or unknown.

Table 3.3 gives our measured peak energies and isotope shifts relative to $^{12}C^{16}O_2$ for a number of peaks in the measured CO_2 isotopologue photoionization spectra for which the spectroscopic assignments are fairly certain, while Table 3.4 shows similar information for the weak so-called "bent valence state" vibrational progression. In both tables, many peaks show the general trend that the (absolute) magnitude of the isotope shifts relative to $^{12}C^{16}O_2$ increase as the mass of the molecule increases due to isotopic substitution (i.e., $^{12}C^{18}O_2$ tends to show a larger isotope shift than $^{12}C^{16}O^{18}O$). Furthermore, for a given isotopologue, the magnitude of the isotope shifts tend to increase as the final vibrational level in the transition increases (i.e., $v'=2$ tends to show a larger shift than $v'=1$); for example, the isotope shifts measured for $^{12}C^{18}O_2$ relative to $^{12}C^{16}O_2$ for the Tanaka-Ogawa n=4 peaks are 0.004 eV for $v'=0$, -0.007 eV for $v'=1$, and -0.011 eV for $v'=2$. The trend that the magnitude of the isotope shifts increases with increasing vibrational level can also be seen visually in Figure 3.4, which shows the "bent valence state" on an expanded energy scale; in Figure 3.4, the peaks labeled a and $a^{\dagger}$, which correspond to transitions to a low vibrational level of the bent valence state according to *Baer and Guyon* [1986], have an isotope shift of -0.004 eV, whereas the peaks labeled f and $f^{\dagger}$, which correspond to transitions to a high vibrational level of the bent valence state, have an isotope shift of -0.029 eV. This trend results from the fact that the vibrational spacing is smaller for the heavier isotopologues due to their smaller zero point energies, and are similar to the trends in the spectra of N_2 isotopologues discussed in Chapter 2. The magnitude of the isotope shifts as well as whether the progressions follow or do not follow these trends provide information on the excited states involved, similar to N_2 in Chapter 2.

In the subsections below, these experimental results for isotope shifts are discussed with a focus on potential applications to CO_2 spectroscopy above the ionization threshold (in Section 3.3.1) and to CO_2-rich planetary atmospheres such as Mars and Venus (in Section 3.3.2).

3.3.1 CO_2 spectroscopy above the ionization threshold

In considering spectroscopic assignments for the CO_2 photoionization spectra and how isotope shifts may aid in identifying controversial or unassigned transitions, recall that the ground-state electronic configuration of CO_2 is

$$(1\sigma_g)^2(1\sigma_u)^2(2\sigma_g)^2(3\sigma_g)^2(2\sigma_u)^2(4\sigma_g)^2(3\sigma_u)^2(1\pi_u)^4(1\pi_g)^4$$

and that CO_2 has four normal vibrational modes – the symmetric stretch (ν_1), two degenerate bends (ν_2), and the asymmetric stretch (ν_3). Transitions from ground state molecular orbitals to valence states (e.g., $1\pi_u \rightarrow 5\sigma_g$ or $4\sigma_g \rightarrow 2\pi_u$) or transitions to Rydberg states converging to a state of the CO_2^+ ion (e.g., $1\pi_u \rightarrow (A\ ^2\Pi_u)\ nd\delta_g$ or $3\sigma_u \rightarrow (B\ ^2\Sigma_u^+)\ ns\sigma_g$) are energetically possible above the ionization threshold; see, e.g., theoretical calculations of photoabsorption and photoionization cross-sections involving both valence and Rydberg states by *Padial et al.* [1981] (using static-exchange and moment-theory calculations) and *Dittman et al.* [1983] (using a multiple-scattering model).

The photoionization spectrum of CO_2 above the ionization threshold has a long history of both theoretical and experimental investigations by a number of groups. Just above the ionization

threshold at 13.7 eV, the photoionization intensity undergoes a sharp increase followed by a decline from ~14.0 eV to 15.0 eV. This region of the spectrum contains some unassigned low intensity progressions just visible above the background continuum. Above ~15.0 eV, another progression becomes visible. *Tanaka and Ogawa* [1962] assigned this progression to the valence transition $\pi_g \rightarrow \sigma_g$ while *Lindholm* [1969] assigned it to the $1\pi \rightarrow 3p\sigma_u$ valence transition. Both assignments are to dipole forbidden transitions, and both assignments remain uncertain. *Baer and Guyon* [1986] used threshold photoelectron spectroscopy (TPES) and determined that the spacing of vibrational peaks in this progression were consistent with excitation to a bent valence state. The experimental investigations of photoionization efficiency spectra of $^{12}C^{16}O_2$ using synchrotron radiation by *Berg et al.* [1994] and *Shaw et al.* [1995] have followed the suggestion that this series comes from the transition to a bent state in the labeling of their figures, and in Figure 3.2 we also label this progression "bent valence state." A bent valence state appears to be consistent with either the Tanaka-Ogawa assignment or the Lindholm assignment but might also be a different series.

Beginning at ~15.2 eV, there is another unidentified series, which we have labeled "Unidentified Rydberg state." *Lindholm* [1969] assigned it to the dipole forbidden valence transition $1\pi_u \rightarrow 3p\pi_u$. According to *Baer and Guyon* [1986], the spacing between peaks in this (vibrational) progression corresponds to excitation of the symmetric stretch of a Rydberg series converging to the A $^2\Pi_u$ state of CO_2^+, but the specific Rydberg orbitals involved are unknown. Starting near 15.8 eV, the "Tanaka-Ogawa series" is observed. *Parr et al.* [1994] used spin-orbit selectivity of angle-resolved photoelectron spectra of CO_2 to investigate electronic structure, symmetry, and decay dynamics of the Tanaka-Ogawa series. Based on this information and calculations of the intensity of ionization via discrete and continuum ionization channels, *Parr et al.* [1994] assigned this series to transitions to the (A $^2\Pi_u$) $nd\delta_g$ Rydberg states, and the numbering of n for this series in Figure 3.2 follows their assignment. However, *Furch et al.* [2013] (in their investigation of $^{12}C^{16}O_2$ using photoelectron spectroscopy and velocity map imaging) and *Shaw et al.* [1995] state that uncertainty still remains and that assignment to the (A $^2\Pi_u$) $nd\sigma_g$ Rydberg states is another possibility, which would decrease the numbering of the quantum number, n, by 1 from that in Figure 3.2. From 15.8 to 16.3 eV, the low intensity Lindholm series can be seen. Lindholm originally [1969] assigned this series to transitions to the (A $^2\Pi_u$) $nd\delta_g$ Rydberg states, which would be in conflict with the assignment of the Tanaka-Ogawa series to transitions to the (A $^2\Pi_u$) $nd\delta_g$ Rydberg states. *Fridh et al.* [1978], who used semi-empirical quantum-chemical calculations to calculate excitation energies for electronic transitions of CO_2, simply assigned this series to transitions to the (A $^2\Pi_u$) nd_g Rydberg states, and *West et al.* [1996], who performed measurements of vibrational branching ratios and photoelectron angular distributions in the Lindholm series region of the spectrum, suggested it could be transitions to the (A $^2\Pi_u$) $nd\pi_g$ Rydberg states. No definitive assignment has been made thus far. Finally, beginning at 16.2 eV, two Rydberg series converging to the B $^2\Sigma_u^+$ state of CO_2^+ are observed – the Henning diffuse and the Henning sharp series, which give rise to the highest intensity peaks measured over our measured energy range. The assignment of these series are well established as transitions to the (B $^2\Sigma_u^+$) $ns\sigma_g$ $^1\Sigma_u^+$ Rydberg states for the Henning diffuse series and (B $^2\Sigma_u^+$) nsd_g $^1\Sigma_u^+$ states for the Henning sharp series.

Given the remaining substantial uncertainties in spectroscopic assignments in the CO_2 photoionization spectrum, our new direct measurements of the relative photoionization spectra for $^{12}C^{16}O_2$, $^{13}C^{16}O_2$, $^{12}C^{16}O^{18}O$, $^{13}C^{16}O^{18}O$, $^{12}C^{18}O_2$, and $^{13}C^{18}O_2$ in principle provide important new constraints on spectroscopic assignments and new benchmarks for theoretical calculations, as was demonstrated in Chapter 2 for N_2. In part because the isotope effects expected for the heteronuclear

triatomic CO_2 spectra are much less straightforward to interpret than those for the homonuclear diatomic N_2, it is beyond the scope of this chapter to explicitly resolve uncertainties in the spectroscopic assignments here. Instead, we present a brief overview of our measured isotope effects and how they might be used in conjunction with theoretical calculations of the CO_2 spectra (such as those performed by *Padial et al.* [1981] and *Dittman et al.* [1983]) and quantum interactions of different states of CO_2 with one another and with the ionization continuum.

Baer and Guyon [1986], in their threshold photoelectron spectra (TPES) measurements noted earlier, were able to measure several isotope shifts between $^{12}C^{16}O_2$ and $^{13}C^{16}O_2$ and to use this information to make several new positive assignments for transitions to specific vibrational levels, including highly excited vibrational levels and combination bands. Isotope shifts were useful in assigning several peaks in their TPES spectrum because for a transition to a final state involving excitation of the symmetric stretch (ν_1), no isotope shift would be expected for $^{13}C^{16}O_2$ relative to $^{12}C^{16}O_2$ since the central C atom does not move during a symmetric stretch; however, for transitions involving excitation of either bends (ν_2) or asymmetric stretches (ν_3), an isotope shift is expected. For example, *Baer and Guyon* [1986] measured a peak at 18.660 eV with no isotope shift, and were able to assign it to the ν_1=10 level of the A $^2\Pi_u$ state of CO_2^+ In another example, they observed a peak at 19.749 eV, which had previously been assigned by three different groups to three different vibrational levels of the C $^2\Sigma_g^+$ state of CO_2^+: the ν_3=1 vibrational level, the $\nu_2+\nu_3$ combination band, and the $\nu_1+\nu_3$ combination band. Based on their measured isotope shift of 5.5 meV, *Baer and Guyon* [1986] favored the assignment of this peak to the $\nu_1+\nu_3$ combination band.

In the same study, *Baer and Guyon* [1986] also used the spacing of $^{12}C^{16}O_2$ peaks in the progression starting at 15 eV to assign this progression to a bent valence state, as noted earlier. However, the signal-to-noise ratio in their experiment over this energy range was insufficient to determine the magnitude of the isotope shift between $^{12}C^{16}O_2$ and $^{13}C^{16}O_2$. Thus, no isotope shift measurements have yet been used to address the uncertainty in the spectroscopic assignment of this progression, and therefore, our measured spectra and isotope shifts shown in Figure 3.4 and Table 3.4 represent the first isotopic data for the bent valence state progression. These new data, coupled with theoretical calculations of the isotope shifts expected for excitations to bent valence states, should provide new information to make a definitive assignment of this progression.

3.3.2. Atmospheric applications

CO_2 is the most abundant gas in the atmospheres of Mars and Venus, and it has a large influence on radiative forcing and climate on these planets, as well as on Earth. On Mars, an ongoing question has been whether or not a thick atmosphere was ever present, as for Venus and Earth, and if so, what happened to it and when [*Lammer et al.*, 2008, 2013]. As noted earlier, newer measurements from the Curiosity rover show CO_2 enriched in $^{13}C^{16}O_2$ relative to $^{12}C^{16}O_2$, [*Webster et al.*, 2013; *Mahaffy et al.*, 2013], more so than most previous measurements from, e.g., the Phoenix lander, by the Viking spacecraft, and by Earth telescopes [e.g., *Niles et al.*, 2010, 2013]. These new results are consistent with atmospheric loss, since various escape processes over time are expected to enrich the CO_2 remaining in the atmosphere in ^{13}C. However, isotope effects in other processes, such as photoionization, may also affect the isotopic composition of CO_2, and thus enrichments in ^{13}C may not be solely related to atmospheric escape. These first full-spectrum measurements of the isotope-specific photoionization cross-sections starting at the photoionization threshold can now be incorporated into atmospheric models to check for the magnitude of isotope fractionation due to CO_2 photoionization.

Figure 3.5 shows the ratios of the photoionization efficiencies for $^{13}C^{16}O_2$, $^{12}C^{16}O^{18}O$, $^{13}C^{16}O^{18}O$, $^{12}C^{18}O_2$, and $^{13}C^{18}O_2$ relative to $^{12}C^{16}O_2$ as a function of photon energy. The largest ratios are 1.3 near the most intense peak – the Henning sharp n=3 transition near 16.5 eV (or 75.25 nm) – yielding a fractionation constant of 300 per mil. At this wavelength, then, photoionization of the isotopically-substituted (or "heavy") isotopologues is favored over photoionization of $^{12}C^{16}O_2$, which would result in an isotopic depletion of the heavy isotopes in the remaining CO_2. In a planetary atmosphere, however, the magnitude of isotopic fractionation depends not on the fractionation constant over a narrow energy range, but over the wide range of available photon energies. This can be evaluated by taking the ratio of photoionization rate coefficients, *J*, for the different isotopologues. For a given isotopologue, *J* can be calculated using Equation 3.1, which is a convolution of the radiation intensity as a function of energy, *I(E)*, with the photoionization cross section, *σ(E)*, for a given isotopologue:

$$J = \int_{E_i}^{E_f} \sigma(E) I(E) dE, \qquad \text{Eq. 3.1}$$

where the integral is over the energies E_i to E_f. Using our measurements for the relative ionization efficiencies along with the solar spectrum for *I(E)* [*Woods et al.*, 1998; *Ribas et al.*, 2005] yields $J(^{13}C^{16}O_2)/J(^{12}C^{16}O_2) = 0.97 \pm 0.02$, $J(^{12}C^{16}O^{18}O)/J(^{12}C^{16}O_2) = 0.97 \pm 0.02$, $J(^{13}C^{16}O^{18}O)/J(^{12}C^{16}O_2) = 0.97 \pm 0.02$, $J(^{12}C^{18}O_2)/J(^{12}C^{16}O_2) = 0.99 \pm 0.02$, and $J(^{13}C^{18}O_2)/J(^{12}C^{16}O_2) = 0.98 \pm 0.02$. The results for the first two singly-substituted isotopologues, $^{13}C^{16}O_2$ and $^{12}C^{16}O^{18}O$, are statistically different from 1 (unlike results for N_2 in Chapter 2 and in *Croteau et al.* [2011], for example) and large enough to be of interest for planetary applications. While not as large as the 300 per mil at a specific energy of 16.5 eV, when the relative ionization efficiencies are integrated over the solar energy spectrum, photoionization of CO_2 results in a fractionation constant of 30 per mil in the direction of enriching the remaining CO_2 in the atmosphere in the heavy isotopes ^{13}C and ^{18}O. A 30 per mil fractionation constant is an isotope effect of sufficient magnitude that it is likely to make a contribution to determining the isotopic composition of CO_2 on Mars, and goes in the direction of the recent observations from the martian rover, Curiosity. These new fractionation constants should be tested in atmospheric models of the isotopic composition of CO_2 on Mars and Venus to assess their effect on the isotopic composition of CO_2 and whether such photoionization isotope effects may compete with atmospheric escape processes on long time scales to isotopically enrich atmospheric CO_2 in carbon and oxygen. (Note that the fractionation constants for doubly substituted CO_2 isotopologues are unlikely to be immediately useful for studies on Mars and Venus in the near future due to their very small abundances and hence difficulty of detection. However, there is interest in these so-called "clumped" isotopes in Earth's atmosphere and in laboratory experiments where very small changes in isotopologues at very small abundances can be detected and interpreted. (See, e.g., *Yeung et al.* [2009] for measurements of $^{13}C^{16}O^{18}O$ in earth's stratosphere.) Furthermore, since formation of CO_2^+ ions is an important first step in many atmospheric loss processes, such as sputtering, ion pickup by solar wind, collisions of ions and molecules, and dissociative recombination (see, e.g., reviews by *Lammer et al.* [2008], *Dubinin et al.* [2011], *Gillmann et al.* [2011], and *Lammer et al.* [2013]), isotope effects in the formation of CO_2^+ may serve to further enhance the isotopic fractionation induced by atmospheric escape and loss.

Finally, these new measurements on the relative photoionization efficiencies for the isotopologues of CO_2 can be used to test the extent to which isotopic shielding may also affect the isotopic composition of CO_2 in a planetary atmosphere. A good candidate for a self-shielding

transition is that near the Henning sharp n=3 transition, which has a large isotope shift in cross-section as well as isotope shift in energy. In the atmosphere of Titan, isotopic self-shielding of N_2 can alter the photoionization and photodissociation rates of N_2 isotopologues as a function of altitude, which can in turn alter the isotopic composition of HCN formed via photochemically formed N atoms and N_2^+ ions [*Liang et al.*, 2007; *Croteau et al.*, 2011]. The ratios of photoionization efficiencies for CO_2 shown in Figure 3.5 are smaller than those for N_2 discussed by *Croteau et al.* [2011] in part because the peaks in the CO_2 photoionization spectrum are wider and overlap to a greater extent, and therefore the effects of self-shielding of CO_2 in CO_2 photoionization may be small compared to that for N_2 in N_2 photoionization. However, now that these experimental results for isotope effects in the photoionization of CO_2 are available, they can be incorporated into atmospheric models of Mars and Venus to assess whether self-shielding may also be a contributor to determining the isotopic composition of CO_2 in their atmospheres.

3.4. Summary

In this chapter, the first isotope specific photoionization efficiency spectra were presented. The photoionization isotope shifts in both energy and intensity can be used to address uncertainties in the spectroscopic assignments of the CO_2 spectrum and as new benchmarks for theoretical calculations of interferences between the Rydberg and valence states involved in photoionization. The measured isotope effects also have potential applications to CO_2-rich atmospheres, such as on Mars and Venus, where the isotope effects we report here may be large enough to induce isotopic fractionation directly or by enhancing isotopic fractionation due to various other CO_2 loss mechanisms that begin with formation of CO_2^+ ions, such as sputtering, ion pickup by solar wind, collisions of ions and molecules, and dissociative recombination. The magnitude of the isotope effects are large enough to warrant inclusion in models of the isotopic composition of CO_2 in planetary atmospheres. The new isotope-specific measurements will also be immediately useful in interpreting isotopic observations of CO_2 currently available from the Mars rover, Curiosity [*Webster et al.*, 2013; *Mahaffy et al.*, 2013], as well as those expected for the upcoming Mars Atmosphere and Volatile EvolutioN (MAVEN) mission arriving in orbit around Mars in 2014 [e.g., *Atreya et al.*, 2013].

Table 3.1. Prominent peaks in the $^{12}C^{16}O_2$ spectrum and locations given by *Tanaka and Ogawa* [1962] used in the energy scale calibration for all measured isotopologues

Peak label	Assignment	Tanaka-Ogawa location (eV)
Henning Diffuse 3	(B $^2\Sigma_u^+$) 3sσ_g $^1\Sigma_u^+$	16.2139
Henning Sharp 3	(B $^2\Sigma_u^+$) 3sd$_g$ $^1\Sigma_u^+$	16.4871
Henning Diffuse 4	(B $^2\Sigma_u^+$) 4sσ_g $^1\Sigma_u^+$	17.0699
Henning Sharp 4	(B $^2\Sigma_u^+$) 4sd$_g$ $^1\Sigma_u^+$	17.2832
Henning Diffuse 5	(B $^2\Sigma_u^+$) 5sσ_g $^1\Sigma_u^+$	17.4580
Henning Sharp 5	(B $^2\Sigma_u^+$) 5sd$_g$ $^1\Sigma_u^+$	17.5396
Henning Diffuse 6	(B $^2\Sigma_u^+$) 6sσ_g $^1\Sigma_u^+$	17.6572
Henning Sharp 6	(B $^2\Sigma_u^+$) 6sd$_g$ $^1\Sigma_u^+$	17.7019

Table 3.2. Mixing ratio of each isotopologue in the photoionized gas mixture

Isotopologue	Mass	Mixing ratio*	Source cylinder	Total for cylinder
$^{12}C^{16}O_2$	44	0.475	Praxair	0.485
$^{13}C^{16}O_2$	45	0.010		
$^{12}C^{16}O^{18}O$	46	0.134	Spectra Gas	0.516
$^{13}C^{16}O^{18}O$	47	0.016		
$^{12}C^{18}O_2$	48	0.360		
$^{13}C^{18}O_2$	49	0.006		

* – Mixing ratio is defined as the abundance of one isotopologue in the mixture relative to the total of all isotopologues, with values derived from experiment as described in Section 3.2.

Table 3.3. Peaks in the CO_2 photoionization spectra and their isotope shifts

Series/member	$^{12}C^{16}O_2$ (eV)	+/-* (eV)	$^{13}C^{16}O_2$ (eV)	+/- (eV)	Shift from $^{12}C^{16}O_2$ (eV)	$^{12}C^{16}O^{18}O$ (eV)	+/- (eV)	Shift from $^{12}C^{16}O_2$ (eV)	$^{13}C^{16}O^{18}O$ (eV)	+/- (eV)	Shift from $^{12}C^{16}O_2$ (eV)	$^{12}C^{18}O_2$ (eV)	+/- (eV)	Shift from $^{12}C^{16}O_2$ (eV)	$^{13}C^{18}O_2$ (eV)	+/- (eV)	Shift from $^{12}C^{16}O_2$ (eV)
Tanaka-Ogawa																	
n=4 v′=0	15.763	0.002	15.760	0.001	-0.003	15.762	0.002	-0.001	15.765	0.002	0.002	15.767	0.001	0.004	15.769	0.002	0.006
n=4 v′=1	15.900	0.001	15.901	0.004	0.001	15.896	0.001	-0.004	15.894	0.001	-0.006	15.893	0.001	-0.007	15.893	0.001	-0.007
n=4 v′=2	16.037	0.001	16.035	0.001	-0.002	16.032	0.001	-0.005	16.029	0.002	-0.008	16.026	0.001	-0.011	16.024	0.002	-0.013
n=4 v′=3	N/A†		N/A†			N/A†			N/A†			N/A†			N/A†		
n=4 v′=4	16.309	0.002	16.304	0.001	-0.005	N/A†			N/A†			N/A†			N/A†		
n=5 v′=0	16.459	0.004	16.454	0.003	-0.005	16.457	0.002	-0.001	16.459	0.003	0.000	16.455	0.002	-0.003	16.456	0.002	-0.002
n=5 v′=1	16.585	0.001	16.584	0.001	-0.001	16.581	0.001	-0.004	16.577	0.001	-0.008	16.576	0.001	-0.009	16.576	0.002	-0.009
n=5 v′=2	16.720	0.001	16.719	0.001	-0.001	16.715	0.001	-0.005	16.715	0.001	-0.005	16.712	0.001	-0.008	N/A‡		
n=5 v′=3	16.862	0.003	16.858	0.002	-0.003	16.852	0.002	-0.010	16.845	0.001	-0.017	16.838	0.001	-0.023	N/A‡		
n=6 v′=0	16.736	0.001	16.733	0.002	-0.002	16.729	0.002	-0.007	N/A†			N/A†			N/A†		
n=6 v′=1	16.897	0.001	16.898	0.001	0.000	16.893	0.001	-0.005	N/A‡			16.892	0.001	-0.005	N/A‡		
n=6 v′=2	17.041	0.001	17.042	0.003	0.001	17.033	0.001	-0.008	N/A†			N/A†			N/A†		
Lindholm																	
v′=0	15.811	0.002	15.822	0.034	0.011	15.812	0.004	0.001	N/A‡			15.817	0.006	0.006	N/A‡		
v′=1	N/A†		N/A†			N/A†			N/A†			N/A†			N/A†		
v′=2	16.083	0.001	16.082	0.001	-0.001	16.077	0.004	-0.006	N/A‡			N/A‡			N/A‡		
Henning Diffuse																	
n=3	16.215	0.001	16.214	0.001	-0.001	16.207	0.001	-0.008	16.204	0.001	-0.011	16.200	0.001	-0.015	16.202	0.003	-0.013
n=4	17.072	0.001	17.071	0.002	-0.001	17.071	0.005	0.000	17.072	0.001	0.001	17.074	0.003	0.003	17.076	0.002	0.004
n=5	17.451	0.001	17.451	0.001	-0.001	17.456	0.001	0.005	17.453	0.006	0.002	17.454	0.002	0.003	17.455	0.002	0.004
n=6	17.657	0.001	17.657	0.001	0.000	17.657	0.001	0.000	17.656	0.001	0.000	17.657	0.001	0.000	17.657	0.001	0.001
Henning Sharp																	
n=3	16.476	0.001	16.477	0.001	0.001	16.476	0.001	0.000	16.476	0.001	0.000	16.477	0.001	0.001	16.476	0.001	0.000
n=4	N/A†		N/A†			N/A†			N/A†			N/A†			N/A†		
n=5	17.538	0.001	17.538	0.001	0.000	17.537	0.001	-0.001	17.538	0.001	0.000	17.536	0.001	-0.002	17.539	0.002	0.001
n=6	17.702	0.001	17.703	0.001	0.000	17.702	0.001	-0.001	17.702	0.001	0.000	17.703	0.001	0.000	17.703	0.002	0.001

* +/- values are given by the 1σ uncertainty in the peak fitting procedure using Igor Pro

N/A† - peak positions were are not reported because peaks were too close to other nearby peaks to obtain a satisfactory peak fitting result

N/A‡ - peak positions were not reported because the signal-to-noise ratio was too low to obtain a satisfactory peak fitting result

Table 3.4. Peak energies and isotope shifts from the "bent valence state" region of the CO_2 spectrum

Peak**	$^{12}C^{16}O_2$ (eV)	+/-* (eV)	$^{12}C^{16}O^{18}O$ (eV)	+/- (eV)	Shift from $^{12}C^{16}O_2$ (eV)	$^{12}C^{18}O_2$ (eV)	+/- (eV)	Shift from $^{12}C^{16}O_2$ (eV)
a	15.007	0.001	15.004	0.003	-0.003	15.003†	0.001	-0.004
b	15.067	0.001	15.058	0.005	-0.009	15.058	0.002	-0.009
c	15.133	0.001	15.129	0.003	-0.004	15.122	0.002	-0.011
d	15.206	0.001	15.199	0.002	-0.006	15.196	0.001	-0.010
e	15.503	0.001	15.488	0.002	-0.015	N/A‡		
f	15.606	0.002	15.590	0.004	-0.016	15.577††	0.000	-0.029

* +/- values are given by the 1σ uncertainty in the peak fitting procedure using Igor Pro.

** as labeled in Figure 3.4

† labeled as $a^{\dagger}$ in Figure 3.4

†† labeled as $f^{\dagger}$ in Figure 3.4

N/A‡ - peak positions were are not reported because peaks were too close to other nearby peaks to obtain a satisfactory peak fitting result

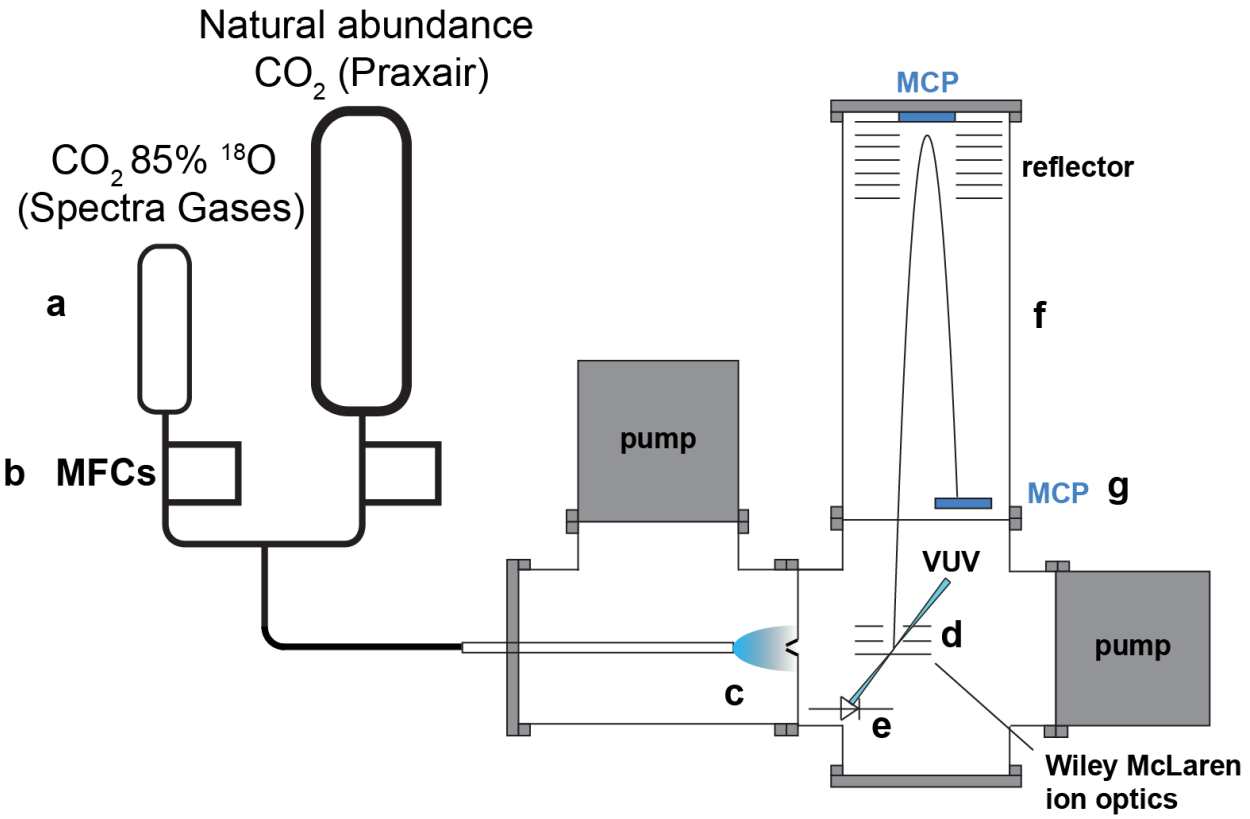

Figure 3.1. Schematic of the apparatus used to determine the relative photoionization cross-sections of CO_2 isotopologues as a function of energy. The apparatus includes (a) two source cylinders: the cylinder of natural abundance CO_2 (Praxair) containing ~99% $^{12}C^{16}O_2$ and ~1% $^{13}C^{16}O_2$, and the cylinder of "85% ^{18}O CO_2" (Spectra Gases) contained 69% $^{12}C^{18}O_2$, 26% $^{12}C^{16}O^{18}O$, 3% $^{13}C^{16}O^{18}O$, 1% $^{13}C^{18}O_2$, and 1% $^{12}C^{16}O_2$, (b) mass-flow controllers (MFCs), (c) supersonic expansion to form a molecular beam of CO_2, (d) molecular beam-photon interaction region, (e) Si-photodiode for monitoring photon intensity, (f) time-of-flight (TOF) tube, and (g) microchannel plate (MCP) detector.

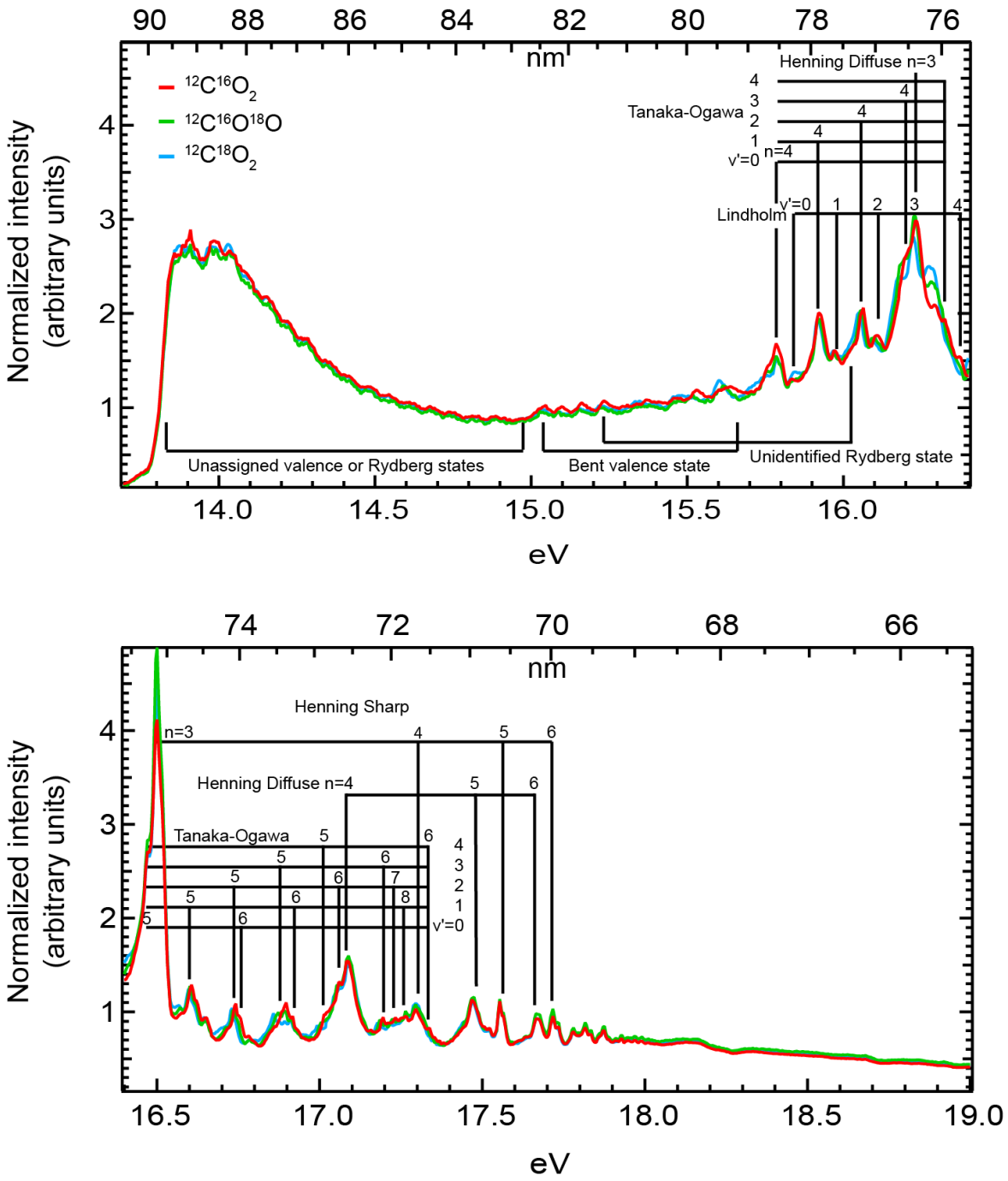

Figure 3.2. Photoionization efficiency spectra for $^{12}C^{16}O_2$ (red), $^{12}C^{16}O^{18}O$ (green), and $^{12}C^{18}O_2$ (blue) along with labels for many valence and Rydberg series. The spectra were taken in ~1 eV sections, with each section measured once and then "stitched" together. The intensity scale is in arbitrary units, with the intensity for each isotopologue normalized (1) by the experimentally measured photon flux, (2) sequentially by the highest intensity in regions of overlapping data during the "stitching together" procedure, and (3) by the mixing ratio for each isotopologue shown in Table 3.2. See text for description of series and proposed assignments.

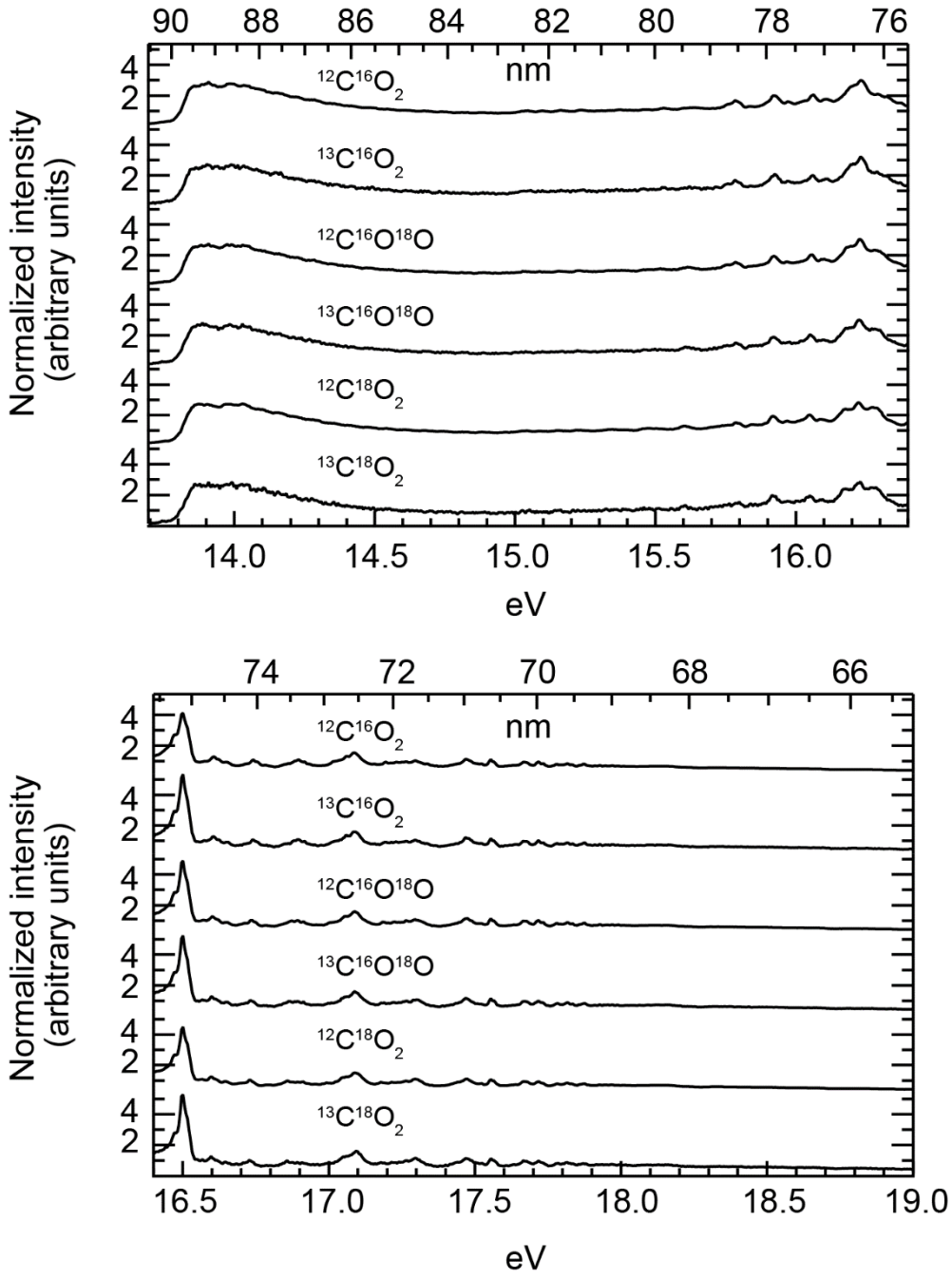

Figure 3.3. Photoionization efficiency spectra for all isotopic species measured: $^{12}C^{16}O_2$, $^{13}C^{16}O_2$, $^{12}C^{16}O^{18}O$, $^{13}C^{16}O^{18}O$, $^{12}C^{18}O_2$, and $^{13}C^{18}O_2$. The intensity scale is in arbitrary units with the intensity for each isotopologue normalized (1) by the experimentally measured photon flux, (2) sequentially by the highest intensity in regions of overlapping data during the "stitching together" procedure, and (3) by the mixing ratio for each isotopologue shown in Table 3.2.

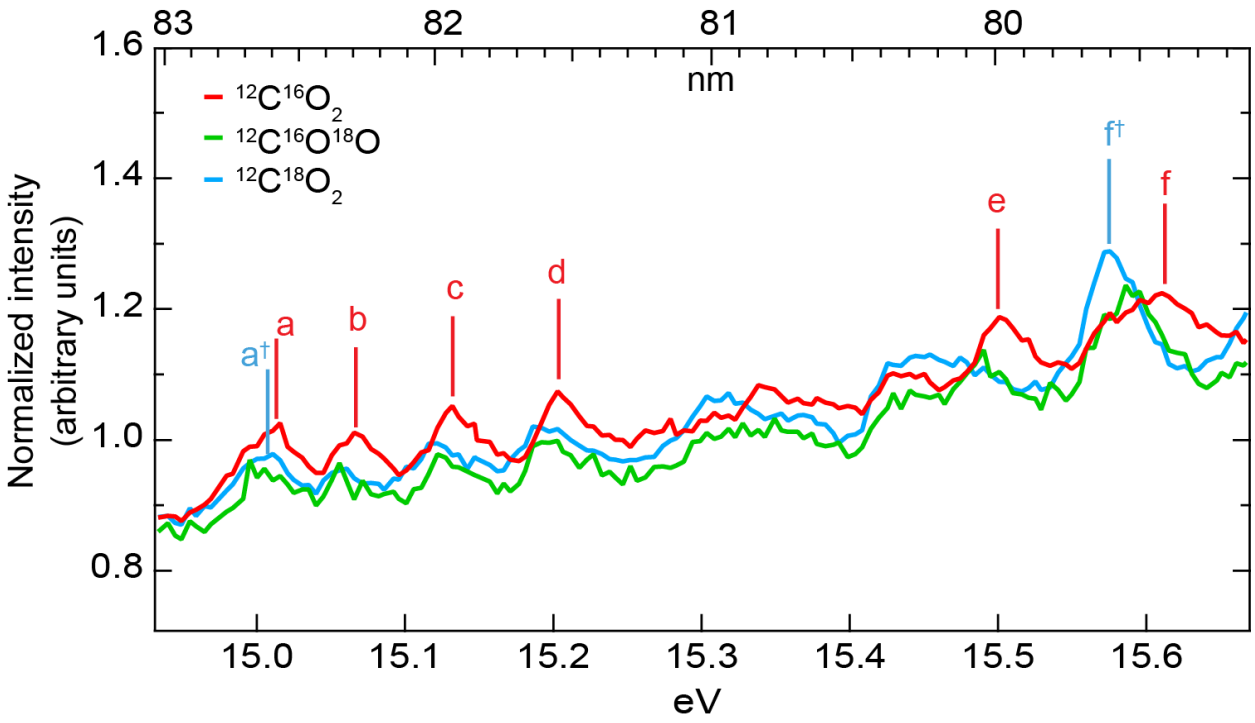

Figure 3.4. CO_2 photoionization data from Figure 3.2 on an enlarged scale for $^{12}C^{16}O_2$, $^{12}C^{16}O^{18}O$, and $^{12}C^{18}O_2$ for the "bent valence state" region of the spectrum. Because of the low intensity of this progression and the small mixing ratios of $^{13}C^{16}O_2$, $^{13}C^{16}O^{18}O$, and $^{13}C^{18}O_2$ in our experiment, peak positions for these isotopologues could not be measured. Peak energies and isotope shifts calculated by fitting the labeled peaks to Lorentz profiles are given in Table 3.4. Peaks a and f in the $^{12}C^{16}O_2$ spectrum correspond to a transition to a low vibrational level and a high vibrational level, respectively, of the bent valence state according to *Baer and Guyon* [1986], and peaks a† and f† correspond to the same transitions in the $^{12}C^{18}O_2$ spectrum.

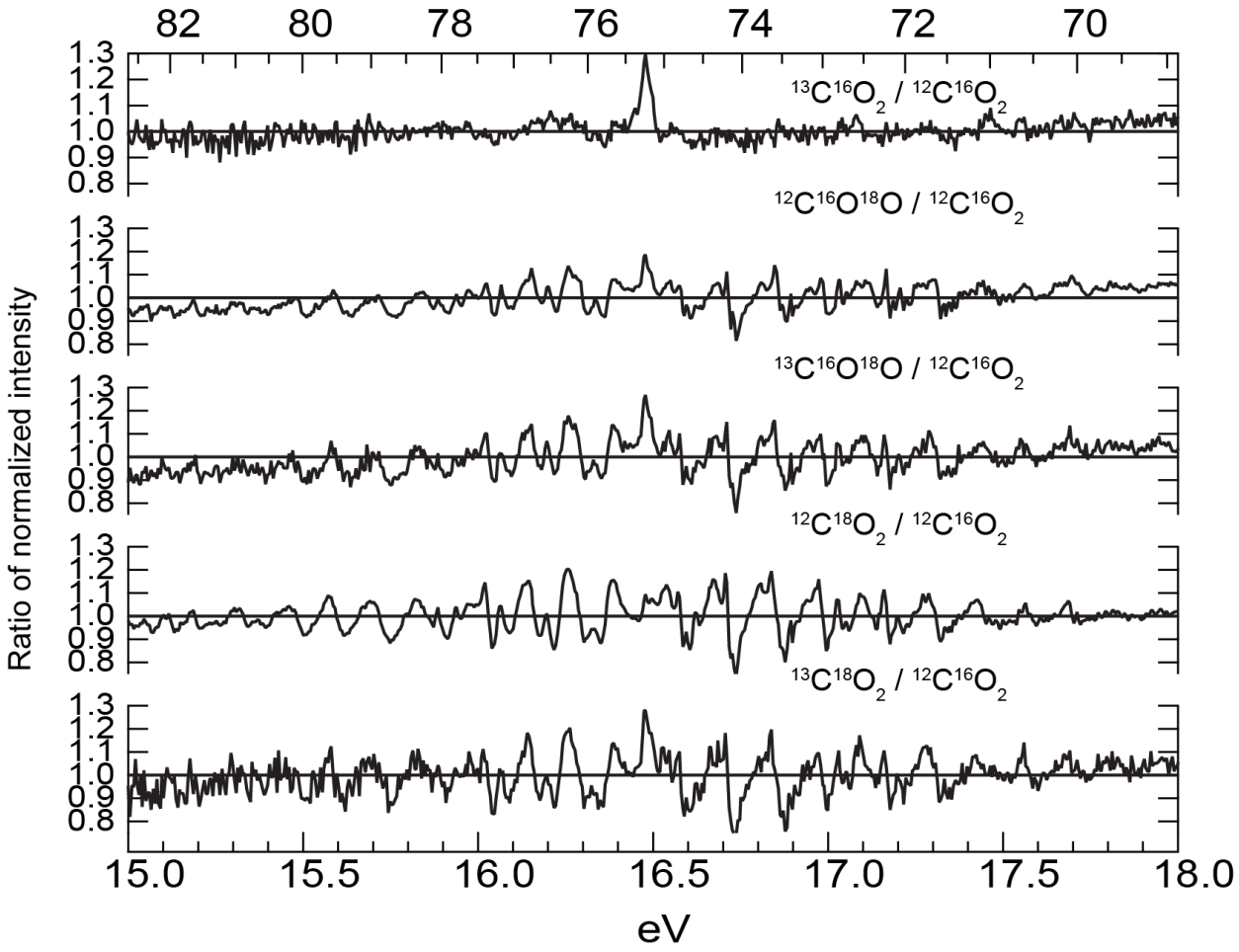

Figure 3.5. Relative photoionization intensities as a function of photon energy for each CO_2 isotopologue relative to $^{12}C^{16}O_2$.

.

Atreya, S.K., M.G. Trainer, H.B. Franz, M.H. Wong, H.L.K. Manning, C.A. Malespin, P.R. Mahaffy, P.G. Conrad, A.E. Brunner, L.A. Leshin, J.H. Jones, C.R. Webster, T.C. Owen, R.O. Pepin, and R. Navarro-Gonzalez (2013) Primordial argon isotope fractionation in the atmosphere of Mars measured by the SAM instrument on Curiosity and implications for atmospheric loss, *Geophys. Res. Lett.*, *40*, 5605–5609, doi:10.1002/2013GL057763.

Baer, T., and P.M. Guyon (1986) Autoionization and isotope effect in the threshold photoelectron-spectrum of $^{12}CO_2$ and $^{13}CO_2$, *J. Chem. Phys.*, *85*, 4765–4778, doi:10.1063/1.451736.

Berg, L.E., A. Karawajczyk, and C. Stromholm (1994) Synchrotron radiation study of photoionization processes of CO_2 in the 13-21 eV region, *J. Phys. B-At. Mol. Opt. Phys.*, *27*, 2971–2980, doi:10.1088/0953-4075/27/14/030.

Bertaux, J.-L., A.C. Vandaele, V. Wilquet, F. Montmessin, R. Dahoo, E. Villard, O. Korablev, and A. Fedorova (2008) First observation of 628 CO_2 isotopologue band at 3.3 μm in the atmosphere of Venus by solar occultation from Venus Express, *Icarus*, *195*, 28–33, doi:10.1016/j.icarus.2008.01.001.

Clayton, R.N. (2002) Solar System - Self-shielding in the solar nebula, *Nature*, *415*, 860–861, doi:10.1038/415860b.

Croteau, P., J.B. Randazzo, O. Kostko, M. Ahmed, M.-C. Liang, Y.L. Yung, and K.A. Boering (2011) Measurements of isotope effects in the photoionization of N_2 and implications for Titan's atmosphere, *Astrophys. J. Lett.*, *728*, L32, doi:10.1088/2041-8205/728/2/L32.

Dittman, P.M., D. Dill, and J.L. Dehmer (1983) Valence-shell photo-absorption by CO_2 and its connections with electron-CO_2 scattering, *Chem. Phys.*, *78*, 405–423, doi:10.1016/0301-0104(83)85127-1.

Dubinin, E., M. Fraenz, A. Fedorov, R. Lundin, N. Edberg, F. Duru, and O. Vaisberg (2011) Ion Energization and Escape on Mars and Venus, *Space Sci. Rev.*, *162*, 173–211, doi:10.1007/s11214-011-9831-7.

Fox, J.L. (1997) Upper limits to the outflow of ions at Mars: Implications for atmospheric evolution, *Geophys. Res. Lett.*, *24*, 2901–2904, doi:10.1029/97GL52842.

Fox, J.L. (2009) Morphology of the dayside ionosphere of Mars: Implications for ion outflows, *J. Geophys. Res.-Planets*, *114*, E12005, doi:10.1029/2009JE003432.

Fox, J.L., and A. Hać (1997) The $^{15}N/^{14}N$ isotope fractionation in dissociative recombination of N_2^+, *J. Geophys. Res.-Planets*, *102*, 9191–9204.

Fox, J.L., and A. Hać (2010) Isotope fractionation in the photochemical escape of O from Mars, *Icarus*, *208*, 176–191, doi:10.1016/j.icarus.2010.01.019.

Fox, J.L., and L.J. Paxton (2005) C and C^+ in the Venusian thermosphere/ionosphere, *J. Geophys. Res.-Space Phys.*, *110*, A01311, doi:10.1029/2004JA010813.

Fridh, C., L. Asbrink, and E. Lindholm (1978) Valence excitation of linear molecules 2. Excitation and UV spectra of C_2N_2, CO_2 and N2O, *Chem. Phys.*, *27*, 169–181, doi:10.1016/0301-0104(78)88002-1.

Furch, F.J., S. Birkner, J.H. Jungmann, F. Kelkensberg, C.P. Schulz, A. Rouzee, and M.J.J. Vrakking (2013) Photoelectron imaging of XUV photoionization of CO_2 by 13-40 eV synchrotron radiation, *J. Chem. Phys.*, *139*, 124309, doi:10.1063/1.4820947.

Gillmann, C., P. Lognonne, and M. Moreira (2011) Volatiles in the atmosphere of Mars: The effects of volcanism and escape constrained by isotopic data, *Earth Planet. Sci. Lett.*, *303*, 299–309, doi:10.1016/j.epsl.2011.01.009.

Gurwell, M.A. (2004) Submillimeter observations of Titan: Global measures of stratospheric temperature, CO, HCN, HC_3N, and the isotopic ratios $^{12}C/^{13}C$ and $^{14}N/^{15}N$, *Astrophys. J.*, *616*, L7–L10, doi:10.1086/423954.

Krasnopolsky, V.A., J.P. Maillard, T.C. Owen, R.A. Toth, and M.D. Smith (2007) Oxygen and carbon isotope ratios in the martian atmosphere, *Icarus*, *192*, 396–403, doi:10.1016/j.icarus.2007.08.013.

Lammer, H., E. Chassefiere, O. Karatekin, A. Morschhauser, P.B. Niles, O. Mousis, P. Odert, U.V. Moestl, D. Breuer, V. Dehant, M. Grott, H. Groeller, E. Hauber, and L.B.S. Pham (2013) Outgassing history and escape of the martian atmosphere and water inventory, *Space Sci. Rev.*, *174*, 113–154, doi:10.1007/s11214-012-9943-8.

Lammer, H., J.F. Kasting, E. Chassefiere, R.E. Johnson, Y.N. Kulikov, and F. Tian (2008) Atmospheric escape and evolution of terrestrial planets and satellites, *Space Sci. Rev.*, *139*, 399–436, doi:10.1007/s11214-008-9413-5.

Liang, M.-C., A.N. Heays, B.R. Lewis, S.T. Gibson, and Y.L. Yung (2007) Source of nitrogen isotope anomaly in HCN in the atmosphere of Titan, *Astrophys. J.*, *664*, L115–L118.

Lindholm, E. (1969) Rydberg serires in small molecules V. Rydberg series in CO_2, *Ark. Fys.*, *40*, 125.

Lyons, A.R. (2008) Photolysis of long-lived predissociative molecules as a source of mass-independent isotope fractionation: The example of SO_2. *In* Advances in Quantum Chemistry, Vol 55: Applications of Theoretical Methods to Atmospheric Science. J.R. Sabin and E. Brandas, editors. 57–74.

Lyons, J.R. (2007) Mass-independent fractionation of sulfur isotopes by isotope-selective photodissociation of SO_2, *Geophys. Res. Lett.*, *34*, L22811, doi:10.1029/2007GL031031.

Lyons, J.R., and E.D. Young (2005) CO self-shielding as the origin of oxygen isotope anomalies in the early solar nebula, *Nature*, *435*, 317–320, doi:10.1038/nature03557.

Mahaffy, P.R., C.R. Webster, S.K. Atreya, H. Franz, M. Wong, P.G. Conrad, D. Harpold, J.J. Jones, L.A. Leshin, H. Manning, T. Owen, R.O. Pepin, S. Squyres, and M. Trainer (2013) Abundance and isotopic composition of gases in the martian atmosphere from the Curiosity rover, *Science*, *341*, 263–266, doi:10.1126/science.1237966.

Marten, A., T. Hidayat, Y. Biraud, and R. Moreno (2002) New millimeter heterodyne observations of Titan: Vertical distributions of nitriles HCN, HC_3N, CH_3CN, and the isotopic ratio $^{15}N/^{14}N$ in its atmosphere, *Icarus*, *158*, 532–544, doi:10.1006/icar.2002.6897.

McElroy, M.B., Y.L. Yung, and A.O. Nier (1976) Isotopic composition of nitrogen - Implications for past history of Mars atmosphere, *Science*, *194*, 70–72, doi:10.1126/science.194.4260.70.

Niemann, H., S. Atreya, S. Bauer, G. Carignan, J. Demick, R. Frost, D. Gautier, J. Haberman, D. Harpold, D. Hunten, G. Israel, J. Lunine, W. Kasprzak, T. Owen, M. Paulkovich, F. Raulin, E. Raaen, and S. Way (2005) The abundances of constituents of Titan's atmosphere from the GCMS instrument on the Huygens probe, *Nature*, *438*, 779–784, doi:10.1038/nature04122.

Niles, P.B., W.V. Boynton, J.H. Hoffman, D.W. Ming, and D. Hamara (2010) Stable isotope measurements of martian atmospheric CO2 at the Phoenix landing site, *Science*, *329*, 1334–1337, doi:10.1126/science.1192863.

Niles, P.B., D.C. Catling, G. Berger, E. Chassefiere, B.L. Ehlmann, J.R. Michalski, R. Morris, S.W. Ruff, and B. Sutter (2013) Geochemistry of carbonates on Mars: Implications for climate history and nature of aqueous environments, *Space Sci. Rev.*, *174*, 301–328, doi:10.1007/s11214-012-9940-y.

Ono, S., A.R. Whitehill, and J.R. Lyons (2013) Contribution of isotopologue self-shielding to sulfur mass-independent fractionation during sulfur dioxide photolysis, *J. Geophys. Res.-Atmospheres*, *118*, 2444–2454, doi:10.1002/jgrd.50183.

Owen, T., J.P. Maillard, C. Debergh, and B.L. Lutz (1988) Deuterium on Mars - The abundance of HDO and the value of D/H, *Science*, *240*, 1767–1770, doi:10.1126/science.240.4860.1767.

Padial, N., G. Csanak, B.V. McKoy, and P.W. Langhoff (1981) Photoexcitation and ionization in carbon dioxide: Theoretical studies in the separated-channel static-exchange approximation, *Phys. Rev. A*, *23*, 218–235, doi:10.1103/PhysRevA.23.218.

Parr, A., P.M. Dehmer, J.L. Dehmer, K. Ueda, J. West, M.R.F. Siggel, and M.A. Hayes (1994) Selective population of spin-orbit levels in the autoionization of a polyatomic molecule: branching ratios and asymmetry parameters for the Tanaka-Ogawa Rydberg series in CO_2, *J. Chem. Phys.*, *100*, 8768–8779, doi:10.1063/1.466731.

Ribas, I., E.F. Guinan, M. Gudel, and M. Audard (2005) Evolution of the solar activity over time and effects on planetary atmospheres. I. High-energy irradiances (1-1700 Å), *Astrophys. J.*, *622*, 680–694, doi:10.1086/427977.

Shaw, D.A., D.M.P. Holland, M.A. Hayes, M.A. MacDonald, A. Hopkirk, and S.M. McSweeney (1995) A study of the absolute photoabsorption, photoionization and photodissociation cross-sections and the photoionization quantum efficiency of carbon-dioxide from the ionization threshold to 345 Å, *Chem. Phys.*, *198*, 381–396, doi:10.1016/0301-0104(95)00159-L.

Tanaka, Y., and M. Ogawa (1962) Rydberg absorption series of CO_2 converging to $^2\Pi_u$ state of CO_2^+, *Can. J. Phys.*, *40*, 879–886.

Villanueva, G.L., M.J. Mumma, R.E. Novak, and T. Hewagama (2008) Discovery of multiple bands of isotopic CO_2 in the prime spectral regions used when searching for CH_4 and

HDO on Mars, *J. Quant. Spectrosc. Radiat. Transf.*, *109*, 883–894, doi:10.1016/j.jqsrt.2007.12.016.

Vinatier, S., B. Bezard, and C.A. Nixon (2007) The Titan $^{14}N/^{15}N$ and $^{12}C/^{13}C$ isotopic ratios in HCN from Cassini/CIRS, *Icarus*, *191*, 712–721, doi:10.1016/j.icarus.2007.06.001.

Waite, J.H., H. Niemann, R.V. Yelle, W.T. Kasprzak, T.E. Cravens, J.G. Luhmann, R.L. McNutt, W.-H. Ip, D. Gell, V. De La Haye, I. Muller-Wordag, B. Magee, N. Borggren, S. Ledvina, G. Fletcher, E. Walter, R. Miller, S. Scherer, R. Thorpe, J. Xu, B. Block, and K. Arnett (2005) Ion Neutral Mass Spectrometer results from the first flyby of Titan, *Science*, *308*, 982–6.

Webster, C.R., P.R. Mahaffy, G.J. Flesch, P.B. Niles, J.H. Jones, L.A. Leshin, S.K. Atreya, J.C. Stern, L.E. Christensen, T. Owen, H. Franz, R.O. Pepin, and A. Steele (2013) Isotope ratios of H, C, and O in CO_2 and H_2O of the martian atmosphere, *Science*, *341*, 260–263, doi:10.1126/science.1237961.

West, J.B., M.A. Hayes, M.R.F. Siggel, J.L. Dehmer, P.M. Dehmer, A.C. Parr, and J.E. Hardis (1996) Vibrationally resolved photoelectron angular distributions and branching ratios for the carbon dioxide molecule in the wavelength region 685-795 Å, *J. Chem. Phys.*, *104*, 3923–3934, doi:10.1063/1.471249.

Woods, T.N., G.J. Rottman, S.M. Bailey, S.C. Solomon, and J.R. Worden (1998) Solar extreme ultraviolet irradiance measurements during solar cycle 22, *Sol. Phys.*, *177*, 133–146, doi:10.1023/A:1004912310883.

Yeung, L.Y., H.P. Affek, K.J. Hoag, W. Guo, A.A. Wiegel, E.L. Atlas, S.M. Schauffler, M. Okumura, K.A. Boering, and J.M. Eiler (2009) Large and unexpected enrichment in stratospheric $^{16}O^{13}C^{18}O$ and its meridional variation, *Proc. Natl. Acad. Sci. U. S. A.*, *106*, 11496–11501, doi:10.1073/pnas.0902930106.

Yurimoto, H., and K. Kuramoto (2004) Molecular cloud origin for the oxygen isotope heterogeneity in the solar system, *Science*, *305*, 1763–1766, doi:10.1126/science.1100989.

Chapter 4

Demonstration of a new *in situ* technique for measuring light scattering by aerosols suspended in the gas phase

4.1 Introduction

Aerosols are present in the atmospheres of many planetary bodies, including Jupiter (e.g., *Kim et al.* [1985]; see also *Zhang et al.* [2013]), Saturn (e.g., *Gillett and Forrest* [1974]; see also *Roman et al.*, 2013]), Uranus (e.g., *Burgdorf et al.* [2006]; see also *Kostogryz* [2013]), Neptune (e.g., *Moses et al.* [1995]; see also *Karkoschka* [2011]), Titan (e.g., *Smith et al.* [1981]; see also *Kim and Courtin* [2013]), and, most likely, the atmospheres of early Earth and Mars (e.g., *Kasting et al.* [1983]; see also *Trainer* [2013]), and have a profound effect on atmospheric radiative transfer. For example, the aerosol 'haze' on Titan, which is comprised of carbon-, hydrogen-, and nitrogen-containing organic compounds produced from the dissociation of CH_4 by UV photolysis and impact by high energy electrons produced by interactions with Saturn's magnetosphere, cools the surface by about 10 K [*McKay et al.*, 1991].

On early Earth, a haze produced via CH_4 photolysis and similar to the haze on Titan may have been present (e.g., see the recent review by *Trainer* [2013] and references therein). Although it is widely thought that this haze would have a cooling effect [*Pavlov et al.*, 2001; *Haqq-Misra et al.*, 2008], as it does on Titan [*McKay et al.*, 1991], *Wolf and Toon* [2010] suggested that the haze may have been composed of fractal particles which were optically thin to visible and IR radiation but optically thick to UV radiation. Such optical properties would have allowed enough visible and IR radiation through to warm the surface yet would have acted as a UV shield, which would decrease the rate of photochemical destruction of UV-labile greenhouse gases, such as CH_4 and NH_3, lower in the atmosphere, and therefore increase the warming potential of these gases [*Pavlov et al.*, 2001]. The presence of a UV-shielding haze is thus one possible solution proposed for the "Faint Young Sun Paradox." The paradox is a contradiction between geological evidence for the presence of liquid water on Earth's surface 2 to 3.8 billion years ago and lack of geochemical evidence that CO_2 levels were high enough in Earth's early atmosphere to have compensated for the fact that the sun was 30% less luminous than compared to present day and hence could not have kept the global surface temperature of Earth above the freezing point of water [e.g., *Sagan and Chyba*, 1997 *Kasting*, 2005; *Haqq-Misra et al.*, 2008; *Kasting*, 2013].

The extent to which aerosols in a planetary atmosphere warm or cool the atmosphere or surface depends on their optical properties, which are determined by the microphysical properties of the aerosol such as size distribution, shape, and index of refraction. For Titan, knowledge of the likely index of refraction of the haze as a function of the wavelength of light is crucial for accurately interpreting spacecraft observations used to estimate aerosol properties such as particle size, density, optical depth, and single scattering albedo, which in turn provide information on radiative transfer as well as constraints on aerosol formation mechanisms [*de Kok et al.*, 2007; *Tomasko et al.*, 2008; *Bellucci et al.*, 2009; *Rannou et al.*, 2010; *Vinatier et al.*, 2010; *Lavvas et al.*, 2010; *Anderson and Samuelson*, 2011; *Vinatier et al.*, 2012]. For early Earth, knowledge of the likely index of refraction as a function of wavelength of any aerosols present, along with particle density, particle shape, and size distribution, is needed to accurately model radiative transfer in early Earth's atmosphere and to predict whether such aerosols would have had a net warming or net cooling effect on the surface [*Pavlov et al.*, 2001; *Domagal-Goldman et al.*, 2008].

The index of refraction of laboratory-generated analogs for Titan aerosol (sometimes referred to as "tholin") has been measured in a number of laboratory studies, including Titan haze analogs generated by electrical discharge [*Khare et al.*, 1984; *Ramirez et al.*, 2002; *Imanaka et al.*, 2004; *Sciamma-O'Brien et al.*, 2012; *Mahjoub et al.*, 2012; *Imanaka et al.*, 2012; *Hadamcik et al.*, 2013] or UV photolysis [*Tran et al.*, 2003, 2005; *Vuitton et al.*, 2009; *Hasenkopf et al.*, 2010] in mixtures of gases such as CH_4, N_2, and sometimes other hydrocarbons known to be present in Titan's atmosphere. Most studies have used transmittance, reflectance, and absorption measurements on thin films of the aerosols collected on slides to determine the index of refraction. Recently, however, *Hasenkopf et al.* [2010] developed a cavity-ring-down aerosol extinction spectroscopy instrument ("CRD-AES") to measure the optical properties of aerosols while still suspended in the gas phase at a wavelength of 532 nm, and found differences between their *in situ* measurements and the earlier thin film measurements of the index of refraction at 532 nm [e.g., *Khare et al.*, 1984] that were large enough to affect interpretations of spacecraft data from Titan. They also measured a much larger index of refraction for early Earth aerosol analogs than that for their Titan aerosol analogs, which has implications for how large an anti-Greenhouse effect may have been present on early Earth given that all recent modeling studies have used the smaller refractive indices for Titan-like aerosols measured on collected films [*Hasenkopf et al.*, 2010]. Due to the short residence time of the aerosol generation apparatus described by *Hasenkopf et al.* [2010], however, only spherical particles can be studied – that is, the particles leave their reaction chamber before the small spherical particles have had a chance to aggregate into fractal particles. Thus, optical properties of fractal particles suspended in the gas phase, which are likely to be important on both Titan [*Tomasko et al.*, 2005] and early Earth [*Wolf and Toon*, 2010], have not been determined experimentally.

In this chapter, the development and preliminary testing of a custom polarimeter deployed on a combination of computer-controlled rotating stages that allow *in situ* measurements of both the polarization and phase function (i.e., angular dependence) of laser light scattered from aerosol particles generated photochemically in the laboratory in a 13 L reaction chamber are presented and discussed. In principle, elements of the scattering matrix for the free-floating aerosol particles can be derived from the measured polarization and phase function of light scattered off the aerosol particles and ultimately inverted to attain the size distribution and index of refraction of the aerosol particles at the laser wavelength of each experiment. Such measurements are expected to be complementary to the technique of CRD-AES used by the Tolbert group and described in *Hasenkopf et al.* [2010], which measures the extinction coefficient of size-selected aerosol particles from which the index of refraction can be derived. Furthermore, the aerosol residence time in our reaction chamber can be long enough (~1-5 days in steady-state for CH_4 photolysis) to produce fractal aerosol particles from aggregation of the smaller spherical particles, demonstrated by field effect scanning electron microscopy (FESEM) showing the fractal shapes of particles collected from the CH_4 photolysis experiments [*Ádámkovics and Boering*, 2003] and consisting of large polyaromatic hydrocarbons as determined by microprobe laser-desorption laser-ionization mass spectrometry [*Ádámkovics*, 2004]. Thus, once optimized, this technique should allow for the first *in situ* light scattering measurements on fractal particles that will yield information on the optical properties of these aerosols needed for both Titan and early Earth studies. In Section 4.2, details of the experimental design as well as calculations for determining the Stokes parameters for light scattering in the experiment are discussed; in Section 4.3, results from light scattering experiments on (1) size-calibrated polystyrene microspheres in aqueous suspensions and (2) photochemically-generated hydrocarbon aerosols produced and suspended in the 13 L reaction

chamber are presented; and in Sections 4.4 and 4.5, the results are discussed and summarized, respectively.

4.2 Methods

We have previously studied the formation of C2 to C4 hydrocarbons in the gas phase and organic aerosols formed via the photolysis of CH_4 with a deuterium lamp in a 13 L stainless steel reaction chamber using a quadrupole mass spectrometer to measure the time evolution of stable gas phase species and a sensitive laser light scattering and detection scheme to detect and monitor the formation of aerosol particles [*Ádámkovics and Boering*, 2003; *Chu*, 2013], as shown schematically in Figure 4.1. These earlier experiments, in which the non-polarized laser beam was scattered by the aerosol in the chamber and detected by a photodiode placed at 90° with respect to the laser beam, demonstrated that our apparatus and approach provide a very sensitive means of detecting photochemically-generated aerosol particles. In an important new extension reported here, we have designed, constructed, and begun to test a means of measuring elements of the light scattering matrix of the photochemically-generated aerosol suspended in the gas phase *in situ* in the reaction chamber, rather than just monitoring the presence of aerosol by the total amount of light scattered at 90°; the scattering matrix can then be inverted to obtain information on the size distribution and/or index of refraction of the scattering medium – i.e., the aerosols in the chamber. In this case, both the polarization state and the angular dependence of the intensity of scattered light must be measured. To do so, we designed and built a custom polarimeter consisting of a quarter-wave plate on a computer-controlled rotating stage followed by a linear polarizer and photodiode, which in turn are mounted on another computer-controlled rotating stage in the reaction chamber; thus, both the polarization and the angular dependence with respect to the incident laser beam of the light scattered by the aerosol can be measured *in situ* in the chamber (See Figure 4.1 and further details below). In Section 4.2.1 below, the custom polarimeter and how it is used to determine elements of the light scattering matrix when aerosol scatters the incident laser beam are described. In Section 4.2.2, the experimental setup for tests of the custom polarimeter outside of the reaction chamber using aqueous suspensions of size-calibrated polystyrene microspheres are described, as well as the Mie theory calculations used to compare with the experimental results. In Section 4.2.3, further details of the photochemical apparatus, how it has been modified from previous experiments, how aerosols are generated photochemically, and the typical experimental protocol are described.

4.2.1 Polarimeter design and calculating Stokes vectors and scattering matrix elements

The custom polarimeter consists of a quarter-wave plate (WPQ05M-633, ThorLabs, Newton, NJ) mounted in a rotating stage (AG-PR100V6, Newport, Irvine, CA), followed by a linear polarizer (5511, New Focus, Santa Clara, CA), with the light intensity passing through the polarimeter monitored by a sensitive Si photodiode detector (PDA55, responsivity of 633 nm of ~0.4 A/W, ThorLabs). (These components and their orientation are shown schematically in Figure 4.1 for the reaction chamber and in Figure 4.2 for tests performed outside the chamber.) As the quarter-wave plate rotates around to different angles, ϕ, the polarization state of light passing through the quarter-wave plate is altered, which in turn alters the intensity of light passing through the linear polarizer and detected by the photodiode. The functional form of light intensity as a function of quarter-wave plate angle ($I(\phi)$) is characteristic of the initial polarization state of light entering the polarimeter which was scattered off the scattering medium [*Goldstein*, 2003], which is what we wish to determine.

More specifically, the polarization state of the light entering the polarimeter is described by the Stokes vector, which has four components, as shown in Equation 4.1.

$$\vec{S} = \begin{pmatrix} S_0 \\ S_1 \\ S_2 \\ S_3 \end{pmatrix} \quad \text{Eq. 4.1}$$

S_0 is the overall intensity of the light, S_1 is the difference between linear horizontally and linear vertically polarized components, S_2 is the difference between linear +45° and linear –45° polarized components, and S_3 is the difference between right-hand circularly and left-hand circularly polarized components. The overall polarization is given by Equation 4.2.

$$P = \frac{\sqrt{{S_1}^2 + {S_2}^2 + {S_3}^2}}{S_0} \quad \text{Eq. 4.2}$$

P = 0 for completely unpolarized light and P = 1 for completely polarized light. Some examples of Stokes vectors describing various polarization states of light are shown in Table 4.1 (Note that S_0 is normalized to 1 in each of the examples). The Stokes vectors of an incident and scattered beam of light are then related by the 16-element scattering matrix for the scattering medium given by Equation 4.3,

$$\begin{pmatrix} S_{0s} \\ S_{1s} \\ S_{2s} \\ S_{3s} \end{pmatrix} = const. \begin{pmatrix} F_{11} & F_{12} & F_{13} & F_{14} \\ F_{21} & F_{22} & F_{23} & F_{24} \\ F_{31} & F_{32} & F_{33} & F_{34} \\ F_{41} & F_{42} & F_{43} & F_{44} \end{pmatrix} \begin{pmatrix} S_{0i} \\ S_{1i} \\ S_{2i} \\ S_{3i} \end{pmatrix}, \quad \text{Eq. 4.3}$$

where the subscript *s* describes scattered light and the subscript *i* describes the incident light (and the 'constant' is proportional to the square of the wavelength of light and inversely proportional to the square of the distance from the scattering region to the detector). Thus, if the Stokes vectors of the incident and scattered light are known, then elements of the scattering matrix can be calculated [*Goldstein*, 2003].

For the new *in situ* aerosol chamber experiments reported here, the incident laser beam was not prepared in a particular polarization state, in part because doing so would decrease the signal-to-noise ratio and in part because taking measurements first with a parallel polarized incident light beam and then repeating with a perpendicularly polarized incident light beam would require a long period of time in which the aerosol steady-state in the chamber would have to remain constant, and determining under what conditions this is the case was beyond the scope of this initial work. For the light scattering experiments with polystyrene microspheres described in Section 4.2.2 below, however, the initial light beam was polarized in either the parallel or perpendicular planes, giving the Stokes vectors in Equations 4.4 and 4.5, respectively.

$$\begin{pmatrix} S_{0i} \\ S_{1i} \\ S_{2i} \\ S_{3i} \end{pmatrix} = \begin{pmatrix} 1 \\ 1 \\ 0 \\ 0 \end{pmatrix}, \text{ parallel} \quad \text{Eq. 4.4}$$

$$\begin{pmatrix} S_{0i} \\ S_{1i} \\ S_{2i} \\ S_{3i} \end{pmatrix} = \begin{pmatrix} 1 \\ -1 \\ 0 \\ 0 \end{pmatrix}, \text{ perpendicular} \qquad \text{Eq. 4.5}$$

Combining Equations 4.3, 4.4, and 4.5 gives the following:

$$F_{11} + F_{12} = S_{0s,parallel} \qquad \text{Eq. 4.6}$$

$$F_{11} - F_{12} = S_{0s,perpendicular} \qquad \text{Eq. 4.7}$$

$$F_{21} + F_{22} = S_{1s,parallel} \qquad \text{Eq. 4.8}$$

$$F_{21} - F_{22} = S_{1s,perpendicular} \qquad \text{Eq. 4.9}$$

Equations 4.6 through 4.9 represent four equations with four unknowns, which can be solved for each of the four matrix elements for the incident light beam [*Goldstein*, 2003].

After scattering by the scattering medium, the intensity of light passing through the polarimeter as a function of quarter-wave plate angle, ϕ, with respect to the linear polarizer is given by Equation 4.10, which is derived from multiplying the Mueller matrices of the quarter-wave plate and linear polarizer, which describe how these components transform the polarization state of the light passing through them.

$$I(\phi) = \frac{1}{2}(S_0 + S_1\cos^2(2\phi) + S_3\sin(2\phi)\cos(2\phi) - S_3\sin 2\phi) \qquad \text{Eq. 4.10}$$

Equation 4.10 can be rewritten in terms of measurable parameters after various trigonometric transformations and variable substitutions:

$$I(\phi) = \frac{1}{2}(A - B\sin(2\phi) + C\cos(4\phi) + D\sin(4\phi)), \qquad \text{Eq. 4.11}$$

where

$$A = S_0 + \frac{S_1}{2}, \qquad \text{Eq. 4.12}$$

$$B = S_3, \qquad \text{Eq. 4.13}$$

$$C = \frac{S_1}{2}, \qquad \text{Eq. 4.14}$$

$$D = \frac{S_2}{2}. \qquad \text{Eq. 4.15}$$

Since Equation 4.11 describes a truncated Fourier series, a Fourier analysis then yields expressions for A, B, C, and D:

$$A = \frac{1}{\pi}\int_0^{2\pi} I(\phi)\, d\phi, \qquad \text{Eq. 4.16}$$

$$B = \frac{2}{\pi}\int_0^{2\pi} I(\phi)\sin(2\phi)\, d\phi, \qquad \text{Eq. 4.17}$$

$$C = \frac{2}{\pi}\int_0^{2\pi} I(\phi)\cos(4\phi)\, d\phi, \qquad \text{Eq. 4.18}$$

$$D = \frac{2}{\pi}\int_0^{2\pi} I(\phi)\sin(4\phi)\, d\phi. \qquad \text{Eq. 4.19}$$

In the experiments reported here for scattering from both the polystyrene spheres performed outside the chamber and the photochemically-generated aerosol inside the chamber, note that the quarter-wave plate is not rotated continuously about ϕ, but rather moved in N discrete steps of $\Delta\phi$ (so that N $\Delta\phi$ is 360°), and the intensity of light passing through the polarimeter to the detector is measured for each step, N. The trapezoid method can then be used to replace the integrals in Equations 4.16 to 4.19 with sums over N [*Goldstein*, 2003; see also *Croteau*, 2010], and the Stokes vector for the scattered light can then be calculated using Equations 4.12 through 4.15. This was the method used to calculate the Stokes vector for the light scattered from the polystyrene spheres outside the chamber. For the preliminary *in situ* aerosol scattering measurements reported here, we used a curve fitting procedure in Igor Pro (Wave Metrics, v. 6.3.4.1) to fit the measured intensity as a function of ϕ to Equation 4.11, rather than approximating the integrals in Equations 4.16 to 4.19.

4.2.2. Test measurements with polystyrene spheres outside the chamber

In order to test the polarimeter, laser light scattering experiments were performed using aqueous suspensions of two different NIST-traceable sizes of polystyrene microspheres diluted in 20 mL Pyrex scintillation vials as the scattering medium. The first suspension was created by placing 0.3 mL of a particle counting standard solution (Duke Scientific, Palo Alto, CA, 4K-02, diameter=1.998±0.020μm, $5x10^8$ spheres mL^{-1}, refractive index=1.59 at 589 nm) consisting of 0.994±0.010 (1σ) μm radius polystyrene microspheres (referred to as '1.0 μm radius spheres' in Section 4.3) in a Pyrex vial and diluting it to 20 mL to yield a final concentration of ~7.5 x 10^6 spheres per mL. The second suspension was created by placing 1 mL of a second particle counting standard solution (Duke Scientific, 3K-990, diameter=0.994±0.010μm, 10^9 spheres mL^{-1}, refractive index=1.59 at 589 nm) consisting of 0.497±0.005 (1σ) μm radius microspheres (referred to as '0.5 μm radius spheres' in Section 4.3) in a Pyrex vial and diluting it to 20 mL to yield to yield a final concentration of approximately ~5 x 10^7 spheres mL^{-1}. The second suspension was created with a higher concentration because the smaller radius spheres scatter light less effectively than larger radius spheres so that a higher concentration is needed to observe comparable scattering intensities. These particle radii were selected as most relevant for the scattering tests since they are within the range of the particle sizes generated by CH_4 photolysis in earlier experiments in this apparatus of radii between ~0.2 and 3 μm by *Ádámkovics and Boering* [2003] as determined by FESEM of collected particles.

A schematic of the light scattering experiments using the aqueous suspensions of size-calibrated polystyrene spheres is shown in Figure 4.2. Light from a HeNe laser (Melles Griot, λ=633 nm, 15 mW, Albuquerque, NM) was chopped at 600 Hz with a mechanical chopper (ThorLabs) coupled to a lock-in amplifier (SR830, Stanford Research Systems, Sunnyvale, CA)

with a time constant of 0.1 seconds. The laser light was then reflected off a mirror and directed to a linear polarizer (LP1) to give it a defined initial polarization state. The linear polarizer LP1 was configured to be either parallel or perpendicular to the linear polarizer that was part of the polarimeter (LP2). Next, the laser light passed through the scattering medium, and some of the light was scattered towards the polarimeter, which was set to some laboratory angle, θ, with respect to the incident laser beam. The intensity of light passing through the polarimeter was detected by the photodiode and then amplified through the lock-in amplifier. The quarter-wave plate angle, ϕ, was incremented in 5° steps by a custom LabWindows/CVI (v. 9.0.1, National Instruments, Austin, TX) program, and the signal from the lock-in amplifier was averaged for 0.2 seconds at each step and recorded by a PC. Four full revolutions of the quarter-wave plate (i.e., 4x360° =1440°) were made at each laboratory angle, θ, and the Stokes parameters derived from the measurements of light intensity as a function of quarter-wave plate angle, ϕ, and laboratory angle, θ, that are presented in Section 4.3 are the averages of the four revolutions. After four full revolutions of the quarter-wave plate for a given laboratory angle, θ, the polarimeter unit was then manually rotated by 5° to the next laboratory angle, θ, until a range of laboratory angles from 10° to 110° was measured.

To compare the scattering results for the polystyrene sphere standard suspensions with Mie theory, MiePlot (v. 4.2.03; *Laven* [2003]) was used, which performs Mie theory calculations using the algorithm published by *Bohren and Huffman* [2007]. For these calculations, the refractive index of the medium (water) was set to 1.33, the real refractive index of the spheres was set to 1.59, and the imaginary refractive index was set to 0. Calculations were performed for spheres of either monodisperse radii (i.e., all spheres in the suspension had equal radii specified by the manufacturer) or, for comparison, polydisperse radii (i.e., the spheres in the suspension had Gaussian distributions of radii with an assumed standard deviation of 10%, well above the 1% specified by the manufacturer).

In some additional tests of the polarimeter performed outside the reaction chamber but not shown here, we note that the accuracy with which the custom polarimeter can retrieve the Stokes vector for laser light of known polarization in the absence of a scattering medium was also tested. For these tests, a parallel or perpendicularly polarized laser light beam was passed through the polarimeter, the light intensity as a function of quarter-wave plate angle, ϕ, with respect to the linear polarizer of the polarimeter unit was measured, amplified, and recorded, and then the measurements were used to calculate the polarization state of the incident laser light. The tests yielded excellent agreement between the Stokes vector for the incident light calculated by the polarimeter measurements and the actual Stokes vector, as discussed in detail in *Croteau* [2010]. The successful retrieval of the initial polarization of light demonstrates that the polarimeter and the associated data analysis can be expected to retrieve precise polarization state information, at least under the conditions which these tests were performed.

4.2.3 *In situ* aerosol measurements in the reaction chamber

4.2.3.1 Details of the aerosol chamber and light-scattering setup

To measure light scattered by photochemically-generated aerosols suspended in the gas phase *in situ*, the entire polarimeter unit was mounted on a computer-controlled horizontal rotating stage (PR50cc, Newport) offset from the axis of rotation by ~5 cm, and placed into the 13 L reaction chamber (recall Figure 4.1). The chamber is equipped with electrical feedthroughs to control the horizontal rotating stage (i.e., to rotate the polarimeter unit to different laboratory

angles, θ, with respect to the incident laser beam) and to control the quarter-wave plate of the polarimeter (i.e., to rotate the quarter-wave plate to different angles, ϕ, with respect to the linear polarizer) from outside the chamber and to record the photodiode signal from the lock-in amplifier through a custom LabWindows/CVI (v. 9.0.1, National Instruments) program without breaking vacuum. In the scattering results presented here, aerosol was formed in the chamber by UV photolysis of acetylene (C_2H_2) using a deuterium lamp (L2D2 L7292, Hamamatsu, Bridgewater, NJ), which emits broadband radiation between 115 nm and 400 nm through a MgF_2 window into the chamber, including Lyman-α radiation at 121.6 nm. The UV light photolyzes some of the C_2H_2 forming hydrocarbon and hydrogen radicals, which then react with additional C_2H_2 molecules and undergo various radical recombination reactions. These radical reactions lead to the formation of new and larger hydrocarbons, which can be undergo photolysis and/or react with radicals, thus creating a complex mixture of hydrocarbons [e.g., *Yung and Demore*, 1999]. Typically within ~5 to 10 minutes of the start of irradiation of C_2H_2, some of the higher molecular weight gases in the mixture exceed their vapor pressure and condense into aerosols, and within ~10 to 20 minutes, the aerosol number density reaches a steady state; this timing is based on the magnitude of laser light scattering at θ=90° (and without the polarimeter) in earlier experiments. After ~60 minutes, a hydrocarbon film clouds the MgF_2 window of the deuterium lamp, decreasing the photon flux and stopping the aerosol formation reactions, which causes the aerosol density to then decrease as aerosols gravitationally settle to the bottom of the chamber. (Note that the experiments on aerosol formed during CH_4 photolysis occur on much longer timescales, from 1 to 5 days, than for C_2H_2 photolysis, as documented in *Ádámkovics and Boering* [2003] and *Chu* [2013], due in large part to the small photon flux of the deuterium lamp at wavelengths that photodissociate CH_4 versus the much larger photon flux at wavelengths that photodissociate C_2H_2, as well as the larger photodissociation cross-sections for C_2H_2.

The optical setup used to detect light scattered by the aerosols is similar to that used for polystyrene microspheres described in Section 4.2.2 except that the components have been placed in the reaction chamber (Figure 4.1). Unpolarized light from a HeNe laser (Melles Griot, λ=613 nm, 8 mW) is reflected off two mirrors and then chopped at 600 Hz with a mechanical chopper, which is coupled to the lock-in amplifier receiving the photodiode signal with a time constant of 0.1 seconds. The chopped laser beam is then directed through a glass viewport into the chamber, where it passes directly over the axis of rotation of the horizontal rotating stage for the polarimeter unit (thus defining θ, the angle between the incident laser beam and the polarimeter unit, including the photodiode detector), through the photochemically-generated aerosol suspended in the gas phase, if present, and is finally terminated by a beam dump. Aerosols formed by the UV photolysis of C_2H_2 which are in the path of the laser beam scatter light, some of which passes through the polarimeter at a laboratory angle θ with respect to the incident laser beam, and the intensity of light passing through the polarimeter as a function of laboratory angle θ and of ϕ (the angle between the quarter-wave plate and the linear polarizer of the polarimeter) is detected by the photodiode, amplified, and recorded.

4.2.3.2 Experimental procedure and data analysis

Prior to running each experiment, the rotating stage, polarimeter, and photodiode are removed from the chamber, and the chamber is baked out and pumped down with a turbomolecular pump (TMU 261, Pfeiffer Vacuum, Nashua, NH) overnight to a pressure of ~1 x 10^{-7} Torr. The chamber is then filled with a positive pressure of argon and then opened in order to place the rotating stage, polarimeter, and photodiode inside the chamber while minimizing the amount of

air (and especially ambient water vapor) the inside of the chamber was exposed to. This part of the procedure is necessary to avoid damaging the computer-controlled rotation stages, which cannot withstand high temperatures at all nor high vacuum for extended periods of time. Once the rotating stage with the polarimeter and the photodiode are placed in the chamber, the polarimeter and photodiode on the rotating stage are set to a laboratory angle, θ, of 60° relative to the incident laser beam. The chamber is then closed and pumped down again overnight with the turbomolecular pump to a pressure of ~5 x 10^{-7} Torr. The gate valve separating the turbomolecular pump and the main part of the chamber is then closed, and the chamber is filled with 200 Torr of C_2H_2 gas (dissolved, >99% purity, Praxair), measured with a capacitance manometer (Baratron, 1000 Torr range, MKS Instruments, Andover, MA). Next, the room lights are switched off in order to decrease the background light reaching the photodiode, and the deuterium lamp is switched on. After approximately 5 minutes of irradiation, aerosols typically start to form, which are detected by an increasing scattering signal from the lock-in amplifier (via the photodiode), and which are also visible to the eye through one of the glass viewports. After approximately 10 minutes, the scattered light signal from the photodiode/lock-in amplifier reaches a steady state, and the Stokes vector measurements of light scattering are then started.

To measure the light scattering intensity as a function of quarter-wave plate angle (i.e., $I(\phi)$) at several lab angles, θ, LabWindows software was used to automatically control the horizontal rotating stage containing the polarimeter (to vary θ) and the quarter-wave plate angle with respect to the linear polarizer on the polarimeter (ϕ). The quarter-wave plate angle, ϕ, was rotated in 10° steps, and the signal from the lock-in amplifier was averaged for 1 second at each step. At each laboratory angle, θ, the quarter wave-plate was rotated two full revolutions (i.e., ϕ=720°), which took ~5 minutes. Then, the horizontal rotating stage was rotated 5°, setting the polarimeter and photodiode to the next lab angle, θ. Measurements for the full range of laboratory angles, from 60° to 95°, took ~45 minutes to acquire.

To calculate the four Stokes parameters of the Stokes vector for the scattered light, the measurements for one full revolution of the quarter-wave plate (ϕ =360°) at each lab angle, θ, was fit to Equation 4.11 using the curve fitting procedure in Igor Pro (Wave Metrics, v. 6.3.4.1), for which the measured intensity is the dependent variable, the quarter-wave plate angle, ϕ, is the independent variable, and S_0, S_1, S_2, and S_3 are constants determined by the curve fitting.

4.3 Results

4.3.1 Scattering measurements on calibrated polystyrene spheres outside the chamber

Figures 4.3 and 4.4 show the intensity of scattered light detected by the photodiode and lock-in amplifier as a function of quarter-wave plate angle (i.e., I vs. ϕ) for the aqueous suspension of 1.0 μm radius polystyrene spheres at laboratory angles, θ, ranging from 10° to 110° using parallel and perpendicular polarized light, respectively. The Stokes parameters for the light scattered by the 1.0 μm radius spheres derived from the measurements shown in Figures 4.3 and 4.4 using Equations 4.16 to 4.19 for all laboratory angles, θ, are given in Table 4.2. As the scattering angle, θ, increases from 0° (with 0° defined as forward scattering) two trends are measured: first, all (unnormalized) Stokes parameters decrease, indicating a decrease in the intensity of scattered light, and second, the overall polarization (P in equation 4.2, which is given by S_1, S_2, and S_3) generally (although not monotonically) decreases for both parallel and perpendicular configurations of incident light. These trends are expected for scattering from spherical particles, as discussed in Section 4.4 below. Similar results for scattered light intensity

measured as a function of ϕ and θ were obtained for the aqueous suspension of 0.5 μm radius polystyrene spheres (not shown), and the Stokes parameters for the light scattered by the 0.5 μm radius polystyrene spheres are given in Table 4.3.

With the Stokes parameters calculated from the measurements, the results can be compared with Mie theory calculations as a function of scattering angle, θ. Both the experimental values and the Mie theory calculations of the intensity of scattered light (given by S_0 for the experimental data) vs. scattering angle, θ, for both the parallel and perpendicular incident laser beams are shown in Figures 4.5 and 4.6 for the 1.0 μm spheres and the 0.5 μm spheres, respectively. While the measured intensity of scattered light was recorded as the voltage from the photodiode and lock-in amplifier, the Mie theory calculations of scattered light intensity given by MiePlot are given in arbitrary units. Therefore, the experimental values were scaled by an arbitrary constant to put them roughly on the same scale as the Mie theory calculations. In general, the measured intensity as a function of laboratory scattering angle is as predicted by Mie theory: the scattered intensity decreases as the scattering angle, θ, increases from 10 to ~80°, then levels off. Comparing on a finer scale, however, the measured scattering intensity does not show the oscillations superimposed on the general trend predicted by Mie theory. A possible explanation for the discrepancy is that the aqueous suspensions of monodisperse spheres are not as monodisperse as the manufacturer claims (or as a result of our dilution procedure). Indeed, the same Mie calculations run for a Gaussian size distribution of 10% around the mean radius of the polystyrene spheres in the aqueous suspensions are also shown in Figures 4.5 and 4.6, and these do show a substantial reduction in the oscillations in scattering intensity as a function of laboratory angle, θ, and are arguably more in line with the measurements. This will be discussed further in the discussion section below.

In addition to comparisons of scattered intensity (i.e., S_0), elements of the scattering matrix derived from the measurements on the polystyrene sphere suspensions can also be compared with Mie theory. Experimental results for the matrix element F_{11} and the ratio of matrix elements F_{12}/F_{11} (as defined in Equation 4.3) are shown in Figures 4.7 and 4.8 for 1.0 μm spheres and Figures 4.9 and 4.10 for 0.5 μm spheres, along with Mie theory calculations for both monodisperse and polydisperse aqueous suspensions. Similar to the results shown in Figures 4.5 to 4.6, the Mie theory calculations for a monodisperse suspension show similar trends as a function of scattering angle but larger oscillations than the experimental results, while the Mie theory calculations for a Gaussian distribution of radii of 10% about the mean show reduced oscillations and appear to better capture the measured dependence on scattering angle.

4.3.2 *In situ* scattering measurements on photochemically-generated hydrocarbon aerosols

Figure 4.11 shows the measured scattered light intensity from the time the deuterium lamp is turned on to the time when the measured intensity drops to near zero. Between 100 and 200 seconds, the intensity fluctuates sharply, presumably due in part to a non-steady state aerosol distribution as aerosol settle from likely formation near the deuterium lamp at the top of the chamber down to the laser interaction region ~12 cm below the deuterium lamp. At ~300 seconds, the signal rises more uniformly as a higher density of larger, aggregate particles starts to form and/or a more steady-state distribution of aerosol within the chamber is achieved. At ~500 seconds, the light scattering measurements as a function of ϕ and θ were started and the intensity starts to oscillate as the quarter-wave plate is rotated to different angles, ϕ. In between steps of the horizontal rotating stage, the overall intensity remains nearly constant. As the lab angle, θ, is

changed with each step of the horizontal stage, however, the intensity drops by a discrete amount since less light is scattered in total at larger angles, as expected.

Figure 4.12 shows the measured *in situ* scattering intensity as a function of ϕ and θ (analogous to Figures 4.3 and 4.4 for the 1 μm radius polystyrene spheres outside the chamber). As noted in the Methods section, the scattering measurements as a function of ϕ are curve fit to Equation 4.11 in order to obtain the Stokes parameters for the scattered light. The fits are also shown in Figure 4.12, and the resulting Stokes parameters from the curve fits along with uncertainties from the curve fitting procedure are shown in Table 4.4. As the scattering angle, θ, increases, the intensity of scattered light (S_0) decreases since less light is scattered at larger angles, similar to the trend measured for the polystyrene sphere suspension outside the chamber and as predicted by Mie theory. In contrast, the polarization state of light (S_1, S_2, and S_3) generally increases with scattering angle, θ, for the *in situ* scattering results, while it decreased for the polystyrene sphere solution results. This difference is simply due to the fact that, in the polystyrene sphere experiments, the incident laser light was initially polarized either parallel or perpendicular to the linear polarizer in the polarimeter (i.e., P=1 for the incident beam of light), and the polarization of scattered light decreased with larger scattering angles. In the *in situ* scattering experiments on photochemically-generated aerosol, the incident laser light was initially unpolarized (i.e., P=0), and polarization of scattered light increased with larger scattering angles. Both are consistent with Mie theory, and the differences merely represent the choice of not polarizing the incident laser beam for the *in situ* measurements due to complications of (1) a possible change in polarization during passage through the glass viewport or placing and remotely controlling another polarizer within the chamber, (2) the time constraints to perform both parallel and perpendicularly polarized through all values of ϕ and θ before the aerosol distribution in the reaction chamber changed significantly, and (3) the decrease in the signal-to-noise ratio due to fewer photons in the incident laser beam when, in fact, all the scattering matrix information desired is in principle attained without polarization of the incident laser beam in any case.

Figure 4.13 shows a comparison of the measurements with polystyrene spheres with the *in situ* measurements of photochemically-generated aerosols, along with Mie theory calculations with a Gaussian size distribution of 10% around the mean radius of the spheres (as shown in Figures 4.5(b) and 4.6(b). For the *in situ* results, Mie theory calculations were done using 0.2 μm spheres (which is the lower end of the range of particles measured by FESEM in *Ádámkovics and Boering* [2003] and the higher end of the range of particles size-selected in *Hasenkopf et al.* [2010]), a real refractive index of n=1.70 and an imaginary refractive index of k=0.016 taken from the study by *Khare et al.* [1984] at 613 nm, in which the index of refraction of Titan-analog aerosols deposited as a thin film was measured over a broad range of wavelengths. Each set of measurements was scaled by an arbitrary constant (one constant for 0.5 μm spheres, one constant for 1.0 μm spheres, and one constant for the *in situ* data) to put them roughly on the same scale as their corresponding Mie theory calculations. Notably, the trends as a function of laboratory angle, θ, for S_0, for F_{11} and for the ratio F_{11}/F_{12} for scattering by the polystyrene sphere suspensions are similar to those predicted by Mie theory (for the polydisperse distribution of spheres, with perhaps the exception of F_{11}/F_{12} for the 0.5 μm spheres at small θ), while the trend as a function of θ for the *in situ* scattering by the aerosol is at smaller θ similar to the Mie theory predictions and then deviates substantially at larger θ – with much larger deviations than those between the polystyrene sphere measurements and their Mie theory predictions. This difference is consistent with the aerosol concentration or, more interestingly, the aerosol properties changing over time in the experiment, which is discussed further below.

4.4 Discussion

The discrepancy between the measurements of scattering intensity from the size-calibrated polystyrene sphere suspensions as a function of scattering angle and the Mie theory calculations – i.e., of the smaller oscillations in the measured data than expected from Mie theory for a monodisperse suspension – is of interest as we characterize the new custom polarimeter. Is an oscillatory signal that we should be detecting being damped out by a problem in the detection scheme or are there other issues with aspects of the test experiment that can explain this discrepancy? For example, one possibility was discussed above in the results section: if the distribution of radii reported by the manufacturer is incorrect (or affected as we implemented it in our experiment after our manipulation of the standard) and wider than its nominal value, then, as shown in the results section above, the oscillations expected for a monodisperse sample of spheres would not be present. Indeed, the experimental data show reasonable agreement with the trends of the Mie theory calculations with a polydisperse distribution of radii. In support of this explanation, other investigators have reported wider than nominal size distributions for the polystyrene sphere standards obtained from Duke Scientific [e.g., *Maltsev et al.*, 1996]. It is also possible that other non-ideal experimental issues may contribute to not observing oscillations, however, including (1) refraction and scattering from the glass vial containing the sample of spheres which was not accounted for, as no effort was made to use optical-quality material or to ensure that laser light was passing through the glass surface of the vial with perfectly normal incidence; any absorption, refraction, or scattering by the glass, especially if it alters the polarization state of the incident light beam, could offset the measured intensity, or (2) non-ideality of any of the optical components (either of the two linear polarizers or the quarter-wave plate) that would affect the intensity of polarized light passing through the polarimeter and would introduce error in the Stokes parameters calculated via Equations 4.16 to 4.19; the tests performed by *Croteau* [2010] on retrieving the known polarization of light from this polarimeter in the absence of a scattering medium were promising and suggest such an effect should be small. Overall, the results for scattering by the polystyrene sphere suspensions are promising and suggest that further testing and optimization of the experimental setup may ultimately allow accurate determinations of the optical properties of scattering media to be made with this apparatus.

The results shown here for determining elements of the scattering matrix for aerosols suspended in the gas phase demonstrate that a remotely-controlled rotating quarter-wave plate polarimeter mounted on rotating stage within a reaction chamber can be used to measure the polarization and phase function of light scattered by aerosol particles *in situ* while still suspended in the gas phase. Clearly, additional work is required to characterize the apparatus enough to warrant intensive calculations to invert the scattering matrix to retrieve the deconvolution of the index of refraction and size distribution of the particles from the *in situ* measurements, but these initial results suggest that we are indeed measuring polarization and phase function signals from aerosol and perhaps even properties of the aerosol in the reaction chamber as it evolves over time. For example, it was noted above that, the intensity of the *in situ* scattering shown in Figure 4.13 at smaller values of θ – data which also correspond to earlier times in the experiment –follow the Mie theory predictions, before deviating substantially at higher values of θ (data which correspond to later times in the experiment). One possibility to explain this discrepancy could be the changing aerosol properties as the irradiation time increases. Although the scattering intensity reaches a steady state within ~10 minutes of irradiation, as time elapses, the aerosol particles formed may be growing larger or aggregating to form fractal particles, which would be consistent with the

decrease in intensity. Of course, decreases in the number density of particles may also be occurring, so additional experiments controlling for this will need to be performed. In addition, changes in the experimental design may also provide other means to investigate the time evolution of aerosol particle size and morphology in future experiments. For example, improving the signal-to-noise by either increasing laser power or increasing the aerosol density could allow for measurements to be taken more quickly since less signal integration at each quarter-wave plate angle, ϕ, would be needed. Previous experience has shown that higher densities of aerosols are formed when contamination of the chamber by residual atmospheric air and water is minimized; although the chamber is pumped down and baked out before each experiment, the chamber must be vented and opened to place the polarimeter unit inside the chamber and then pumped down again for a shorter period without baking out (in order to protect sensitive electronic components of the rotating stages, which could be damaged by high temperatures or long exposure to high vacuum). Scattering experiments done without the polarimeter in the chamber (not shown here) typically showed a stronger scattering signal than the experiments presented here, possibly due to the chamber not needing to be vented and opened after pumping down and baking out. The polarimeter can also be tested in a photochemical system that takes place on a longer time scale, such as the irradiation of CH_4 done previously by our group [*Ádámkovics and Boering*, 2003; *Chu*, 2013]. The irradiation of C_2H_2 discussed here takes place over ~60 minutes before the deuterium lamp becomes clouded with an aerosol film and the photon flux decreases, eventually stopping the aerosol formation reactions, whereas irradiation experiments done with CH_4 take place over 1 to 5 days, which may allow a much longer experimental time scale to be investigated in which many cycles of measurements of scattering as a function of ϕ and θ can occur. In this manner, the time-dependence of aerosol optical properties can in principle be measured as gases condense to form small spherical particles and these small spherical particles then aggregate for form fractals.

4.5 Summary

In this chapter, polarization measurements of light scattered by polystyrene microspheres and by photochemically-generated aerosols using a custom-designed polarimeter mounted on a rotating stage were presented. From the measured light scattering intensity as a function of the quarter-wave plate angle, ϕ, and as a function of laboratory scattering angle, θ, the Stokes parameters of the scattered light and scattering matrix elements could then be calculated. For light scattering measurements on size-calibrated polystyrene spheres in aqueous suspensions, the scattering showed generally good agreement with Mie theory calculations but with the intriguing result that the suspensions may not be monodisperse in the sphere radii and/or that further optimizations need to be done for our custom polarimeter. For light scattering measurements on photochemically-generated hydrocarbon aerosols suspended in the gas phase within our 13 L reaction chamber, the *in situ* Stokes parameters have been successfully measured. With a fully operational computer-controlled setup, work can now be done to improve the signal-to-noise ratio and component alignment of the *in situ* light scattering apparatus, with the ultimate goal of deriving the index of refraction and size distribution of photochemically-generated aerosols as a function of time and initial gas composition for applications to radiative transfer in planetary atmospheres, such as early Earth and Titan.

Table 4.1. Examples of Stokes vectors describing various polarization states of light. (Note that S_0, representing the overall intensity of light, is normalized to 1 in each of the examples.)

$\begin{pmatrix}1\\0\\0\\0\end{pmatrix}$ Unpolarized	$\begin{pmatrix}1\\1\\0\\0\end{pmatrix}$ Linearly polarized (horizontal)	$\begin{pmatrix}1\\-1\\0\\0\end{pmatrix}$ Linearly polarized (vertical)
	$\begin{pmatrix}1\\0\\1\\0\end{pmatrix}$ Linearly polarized (+45°)	$\begin{pmatrix}1\\0\\-1\\0\end{pmatrix}$ Linearly polarized (-45°)
	$\begin{pmatrix}1\\0\\0\\1\end{pmatrix}$ Left hand circularly polarized	$\begin{pmatrix}1\\0\\0\\-1\end{pmatrix}$ Right hand circularly polarized

Table 4.2. Stokes parameters calculated from the light scattering experiments on the 1.0 μm polystyrene sphere suspensions using Equations 4.16 to 4.19 for both parallel and perpendicular polarized light.

1.0 μm radius spheres - Parallel polarization

Angle	Calculated Stokes parameters				Normalized to S_0			
	S_0	S_1	S_2	S_3	S_0	S_1	S_2	S_3
10	5.9138	5.5550	-0.0361	0.6847	1.0000	0.9393	-0.0061	0.1158
15	3.9384	3.6650	0.0363	0.4690	1.0000	0.9306	0.0092	0.1191
20	2.6901	2.5048	0.0223	0.3226	1.0000	0.9311	0.0083	0.1199
25	1.6616	1.5377	0.0024	0.1873	1.0000	0.9254	0.0014	0.1127
30	1.1320	1.0416	0.0055	0.1244	1.0000	0.9202	0.0049	0.1099
35	0.8181	0.7359	0.0037	0.0959	1.0000	0.8995	0.0045	0.1172
40	0.5179	0.4680	0.0052	0.0575	1.0000	0.9036	0.0101	0.1111
45	0.3437	0.3174	0.0036	0.0373	1.0000	0.9235	0.0103	0.1084
50	0.2514	0.2230	0.0033	0.0275	1.0000	0.8869	0.0132	0.1095
55	0.1588	0.1380	0.0021	0.0171	1.0000	0.8690	0.0133	0.1074
60	0.1020	0.0876	0.0026	0.0110	1.0000	0.8594	0.0252	0.1079
65	0.0753	0.0627	0.0012	0.0076	1.0000	0.8330	0.0156	0.1005
70	0.0537	0.0431	0.0003	0.0050	1.0000	0.8024	0.0049	0.0933
75	0.0459	0.0337	0.0006	0.0036	1.0000	0.7349	0.0124	0.0790
80	0.0411	0.0301	0.0020	0.0034	1.0000	0.7325	0.0475	0.0823
85	0.0357	0.0238	0.0006	0.0027	1.0000	0.6670	0.0166	0.0764
90	0.0285	0.0192	0.0011	0.0021	1.0000	0.6745	0.0394	0.0741
95	0.0276	0.0169	0.0014	0.0015	1.0000	0.6127	0.0502	0.0528
100	0.0245	0.0156	0.0002	0.0015	1.0000	0.6381	0.0065	0.0617
105	0.0237	0.0139	0.0006	0.0011	1.0000	0.5851	0.0255	0.0459
110	0.0211	0.0115	0.0003	0.0011	1.0000	0.5469	0.0158	0.0521

1.0 μm radius spheres - Perpendicular polarization

Angle	Calculated Stokes parameters				Normalized to S_0			
	S_0	S_1	S_2	S_3	S_0	S_1	S_2	S_3
10	6.1828	-6.1146	0.1277	0.5423	1.0000	-0.9890	0.0207	0.0877
15	3.3106	-3.2791	-0.0061	0.2560	1.0000	-0.9905	-0.0018	0.0773
20	2.3168	-2.2919	-0.0098	0.1809	1.0000	-0.9893	-0.0042	0.0781
25	1.3584	-1.3393	-0.0139	0.1101	1.0000	-0.9859	-0.0102	0.0810
30	0.8164	-0.8010	-0.0002	0.0654	1.0000	-0.9812	-0.0003	0.0801
35	0.6524	-0.6392	-0.0385	0.0593	1.0000	-0.9798	-0.0590	0.0909
40	0.3161	-0.3061	-0.0003	0.0222	1.0000	-0.9682	-0.0010	0.0702
45	0.2191	-0.2095	-0.0011	0.0177	1.0000	-0.9566	-0.0051	0.0806
50	0.1785	-0.1689	-0.0014	0.0126	1.0000	-0.9466	-0.0079	0.0704
55	0.1219	-0.1128	-0.0008	0.0097	1.0000	-0.9247	-0.0067	0.0792
60	0.0839	-0.0751	-0.0002	0.0063	1.0000	-0.8951	-0.0029	0.0752
65	0.0652	-0.0576	-0.0001	0.0046	1.0000	-0.8833	-0.0016	0.0699
70	0.0463	-0.0390	-0.0001	0.0027	1.0000	-0.8418	-0.0024	0.0581
75	0.0420	-0.0348	0.0006	0.0026	1.0000	-0.8276	0.0147	0.0613
80	0.0358	-0.0289	0.0001	0.0021	1.0000	-0.8067	0.0024	0.0587
85	0.0302	-0.0233	0.0011	0.0016	1.0000	-0.7698	0.0361	0.0525
90	0.0314	-0.0244	0.0012	0.0013	1.0000	-0.7771	0.0390	0.0415
95	0.0291	-0.0214	0.0006	0.0011	1.0000	-0.7341	0.0197	0.0384
100	0.0278	-0.0201	0.0006	0.0009	1.0000	-0.7248	0.0228	0.0337
105	0.0365	-0.0280	0.0011	0.0009	1.0000	-0.7674	0.0311	0.0255

Table 4.3. Stokes parameters calculated for the light scattering experiments on the 0.5 µm polystyrene sphere suspensions using Equations 4.16 to 4.19 for both parallel and perpendicular polarized light.

0.5 µm radius spheres - Parallel polarization

Angle	Calculated Stokes parameters				Normalized to S_0			
	S_0	S_1	S_2	S_3	S_0	S_1	S_2	S_3
15	3.8501	3.3611	-0.0106	0.4069	1.0000	0.8730	-0.0028	0.1057
20	2.3456	2.0528	-0.0132	0.2320	1.0000	0.8752	-0.0056	0.0989
25	1.6142	1.4081	-0.0052	0.1628	1.0000	0.8723	-0.0032	0.1008
30	1.1713	1.0134	0.0011	0.1166	1.0000	0.8652	0.0009	0.0996
35	0.8309	0.7298	-0.0224	0.0984	1.0000	0.8783	-0.0270	0.1184
40	0.5180	0.4430	-0.0002	0.0512	1.0000	0.8552	-0.0004	0.0988
45	0.3504	0.3012	0.0008	0.0340	1.0000	0.8595	0.0023	0.0970
50	0.2399	0.2081	0.0010	0.0238	1.0000	0.8674	0.0041	0.0992
55	0.1945	0.1666	0.0008	0.0191	1.0000	0.8564	0.0043	0.0983
60	0.1261	0.1067	0.0010	0.0120	1.0000	0.8458	0.0082	0.0951
65	0.0806	0.0692	0.0004	0.0079	1.0000	0.8585	0.0048	0.0978
70	0.0644	0.0531	0.0008	0.0060	1.0000	0.8245	0.0124	0.0936
75	0.0459	0.0346	0.0001	0.0042	1.0000	0.7533	0.0028	0.0921
80	0.0322	0.0248	0.0000	0.0030	1.0000	0.7688	0.0008	0.0943
85	0.0270	0.0203	0.0004	0.0026	1.0000	0.7520	0.0139	0.0961
90	0.0214	0.0161	0.0002	0.0016	1.0000	0.7500	0.0074	0.0730
95	0.0176	0.0124	-0.0001	0.0009	1.0000	0.7056	-0.0079	0.0526
100	0.0153	0.0118	0.0011	0.0009	1.0000	0.7723	0.0722	0.0588
105	0.0134	0.0089	0.0008	0.0008	1.0000	0.6657	0.0594	0.0566
110	0.0126	0.0083	0.0006	-0.0001	1.0000	0.6618	0.0487	-0.0081

0.5 µm radius spheres - Perpendicular polarization

Angle	Calculated Stokes parameters				Normalized to S_0			
	S_0	S_1	S_2	S_3	S_0	S_1	S_2	S_3
10	4.3741	-4.3377	0.0970	0.3580	1.0000	-0.9917	0.0222	0.0819
15	3.3811	-3.3555	-0.0030	0.2421	1.0000	-0.9924	-0.0009	0.0716
20	2.2832	-2.2636	-0.0141	0.1651	1.0000	-0.9914	-0.0062	0.0723
25	1.5857	-1.5687	-0.0096	0.1127	1.0000	-0.9893	-0.0060	0.0710
30	1.0293	-1.0162	-0.0053	0.0767	1.0000	-0.9872	-0.0052	0.0745
35	0.6943	-0.6827	-0.0098	0.0521	1.0000	-0.9833	-0.0141	0.0750
40	0.4713	-0.4618	-0.0063	0.0340	1.0000	-0.9799	-0.0133	0.0721
45	0.3494	-0.3410	-0.0056	0.0261	1.0000	-0.9759	-0.0159	0.0747
50	0.2301	-0.2235	-0.0040	0.0167	1.0000	-0.9712	-0.0173	0.0727
55	0.1786	-0.1721	-0.0030	0.0129	1.0000	-0.9640	-0.0170	0.0720
60	0.1336	-0.1275	-0.0021	0.0097	1.0000	-0.9548	-0.0154	0.0724
65	0.0886	-0.0836	-0.0012	0.0060	1.0000	-0.9433	-0.0130	0.0673
70	0.0678	-0.0633	-0.0012	0.0044	1.0000	-0.9337	-0.0179	0.0646
75	0.0550	-0.0508	-0.0012	0.0030	1.0000	-0.9238	-0.0217	0.0554
80	0.0457	-0.0423	-0.0004	0.0023	1.0000	-0.9252	-0.0085	0.0499
85	0.0360	-0.0329	-0.0006	0.0016	1.0000	-0.9142	-0.0169	0.0441
90	0.0295	-0.0268	-0.0001	0.0014	1.0000	-0.9107	-0.0019	0.0477
95	0.0248	-0.0223	-0.0005	0.0008	1.0000	-0.8976	-0.0218	0.0322
100	0.0250	-0.0224	0.0002	0.0005	1.0000	-0.8964	0.0092	0.0184
105	0.0259	-0.0230	-0.0006	0.0002	1.0000	-0.8879	-0.0216	0.0070

Table 4.4. Stokes parameters calculated from the *in situ* light scattering experiments on photochemically-generated aerosols by fitting experimental data to Equation 4.11

Angle	Calculated Stokes parameters				Normalized to S_0			
	S_0	S_1	S_2	S_3	S_0	S_1	S_2	S_3
60	0.094±0.001*	-0.011±0.002	0.010±0.002	0.002±0.001	1.00	-0.11±0.02	0.11±0.02	0.02±0.01
65	0.066±0.001	-0.013±0.001	0.002±0.001	0.001±0.001	1.00	-0.20±0.02	0.03±0.02	0.02±0.01
70	0.060±0.001	-0.013±0.001	0.001±0.001	-0.001±0.001	1.00	-0.21±0.02	0.01±0.02	-0.02±0.01
75	0.042±0.001	-0.012±0.002	0.002±0.002	-0.001±0.001	1.00	-0.28±0.04	0.05±0.04	-0.02±0.02
80	0.024±0.001	-0.010±0.002	0.002±0.002	-0.001±0.001	1.00	-0.43±0.07	0.08±0.07	-0.05±0.03
85	0.006±0.001	-0.003±0.001	0.001±0.001	-0.001±0.001	1.00	-0.58±0.20	0.14±0.20	-0.12±0.10

* Uncertainty values are the 1σ errors given by the curve fitting analysis.

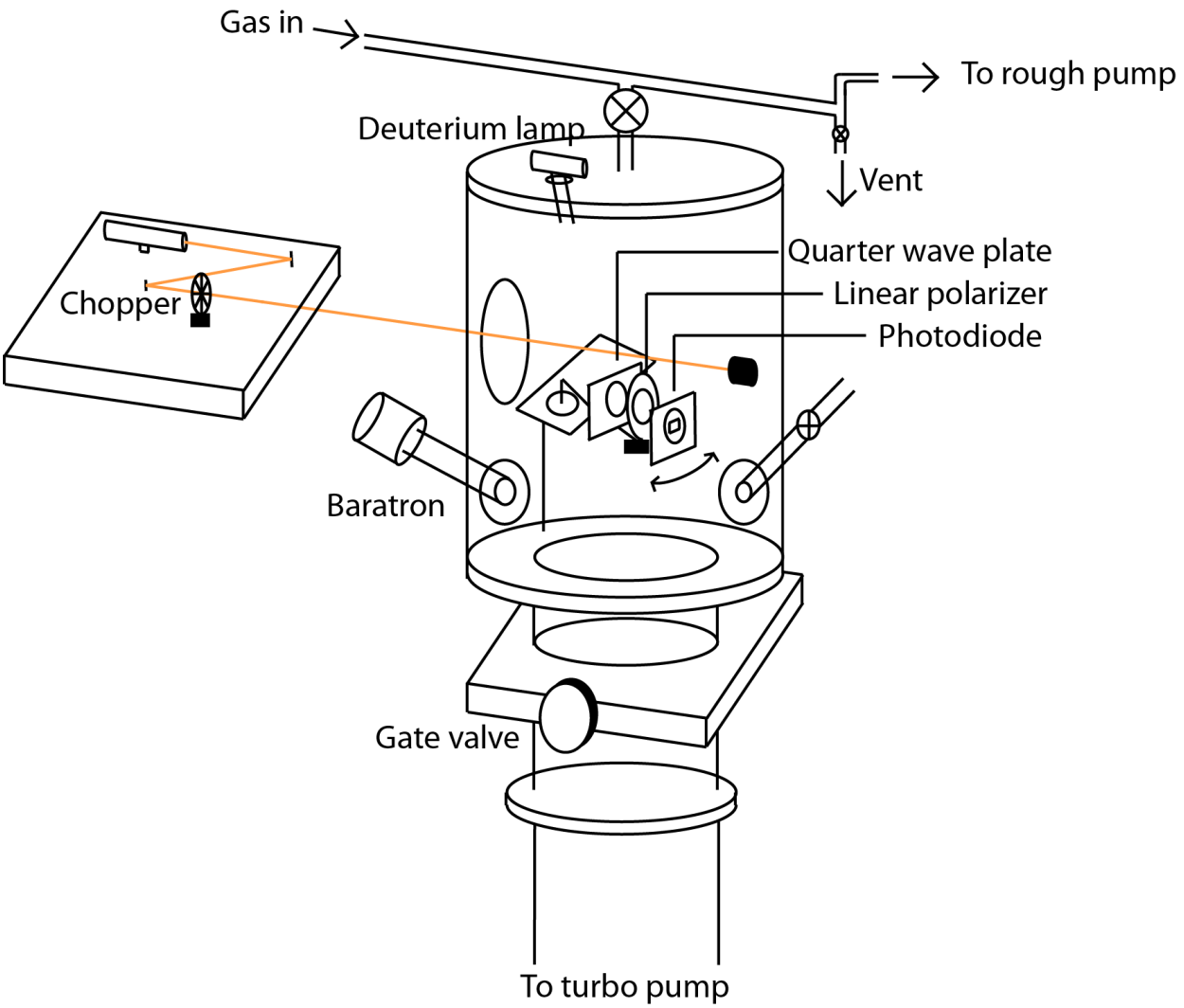

Figure 4.1. Schematic of the experimental setup used for *in situ* measurements of photochemically-generated aerosols suspended in the gas phase. Aerosols are formed by UV photolysis of C_2H_2 by a deuterium lamp in the 13 L stainless steel chamber at ~200 Torr of C_2H_2. Laser light from a 613 nm HeNe laser is chopped at 600 Hz and introduced into the chamber through a glass viewport. Laser light is scattered by the aerosol towards the new polarimeter, which consists of (1) a quarter-wave plate whose angle, ϕ, with respect to the linear polarizer is remotely rotated, (2) a linear polarizer, and (3) a photodiode, and the entire polarimeter unit can be remotely rotated horizontally to different laboratory angles, θ, with respect to the incident laser beam; the signal from the photodiode is amplified by a lock-in amplifier synchronized with the chopper frequency.

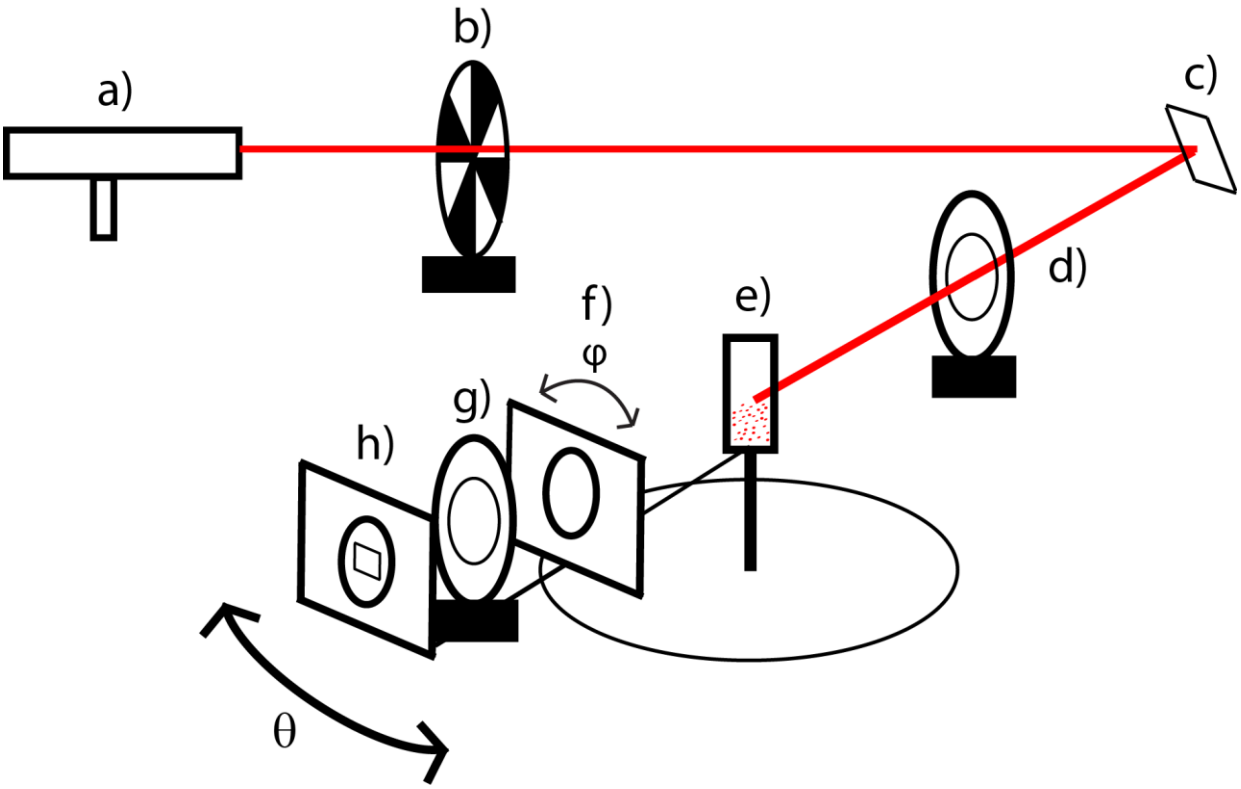

Figure 4.2. Schematic of the experimental setup used for the test case of aqueous suspensions of size-calibrated polystyrene spheres. The components are a) HeNe laser with wavelength 633 nm, b) chopper wheel operated at 600 Hz, c) mirror, d) linear polarizer, e) scattering medium: polystyrene spheres suspended in water in a 20 mL glass scintillation vial, f) quarter-wave plate mounted in a computer-controlled rotating stage, which is rotated in discrete steps to different angles, ϕ, g) linear polarizer, and h) photodiode. Components f, g, and h, were rotated manually to different laboratory angles, θ, for the experiments with a suspension of polystyrene spheres as the scattering medium.

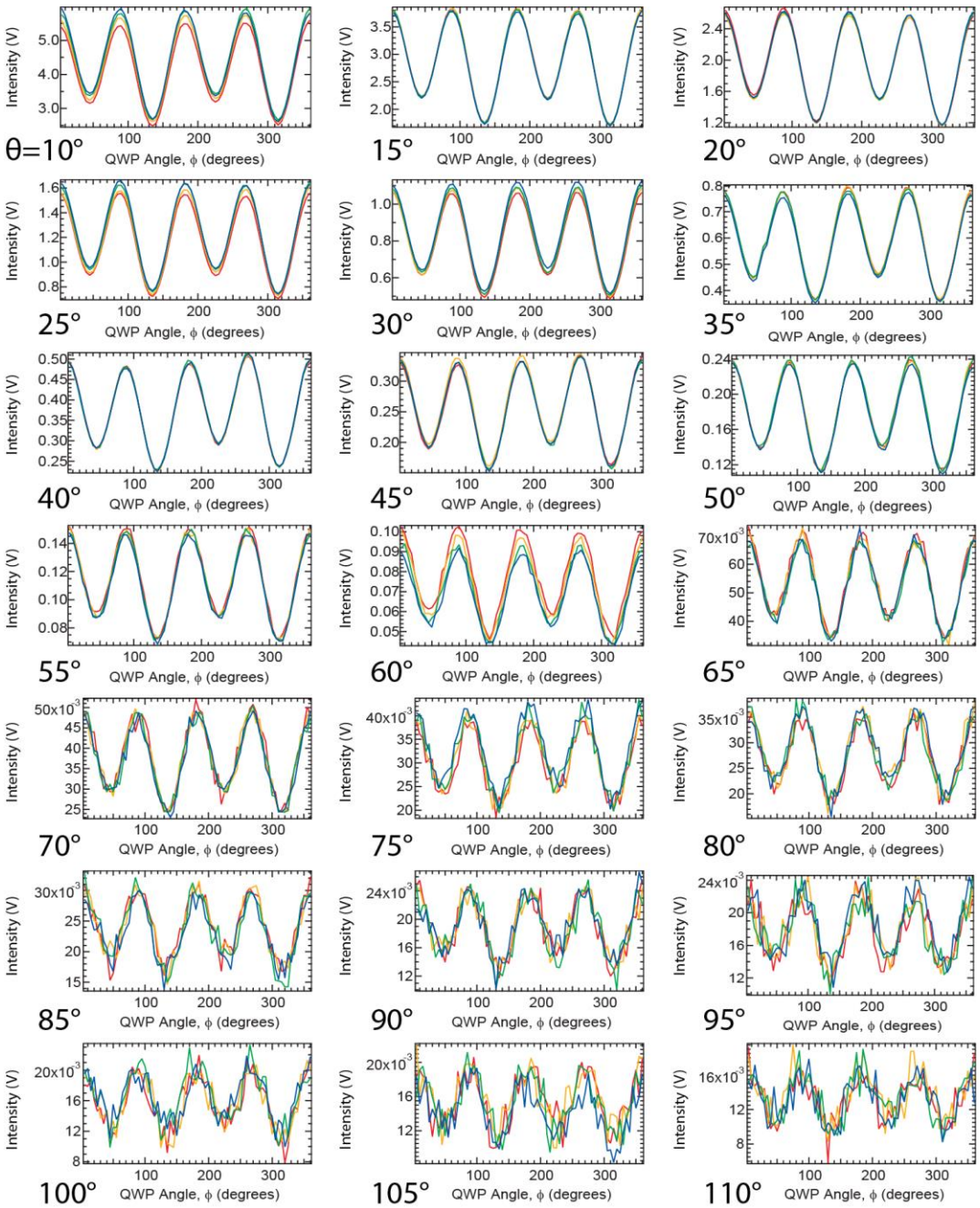

Figure 4.3. Signal intensity passing through the polarimeter and detected by the photodiode as a function of quarter-wave plate angle, ϕ, for parallel polarized light scattered by the aqueous suspension of polystyrene spheres with radius 1.0 μm at laboratory angles, θ, between 10° and 110°. Each lab angle was measured for four full revolutions of the quarter-wave plate (represented by four different colors, red, orange, green and blue in each of the graphs), and Stokes parameters from all four revolutions were averaged together for the values reported in the top half of Table 4.3.

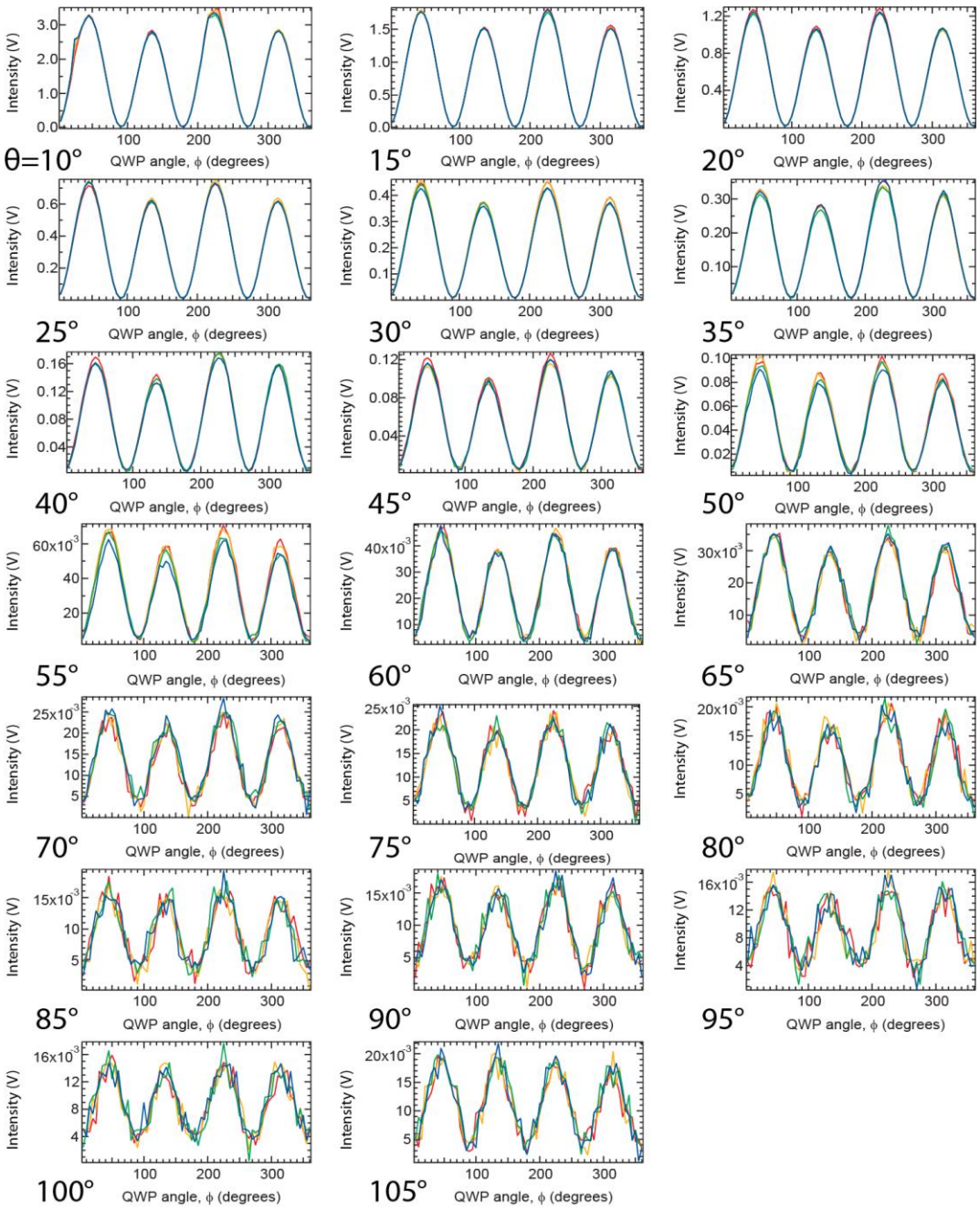

Figure 4.4. Signal intensity passing through the polarimeter and detected by the photodiode as a function of quarter-wave plate angle for perpendicular polarized light scattered by polystyrene spheres with radius 1.0 μm at laboratory angles, θ, between 10° and 105°. Each lab angle was measured for four full revolutions of the quarter-wave plate (represented by four different colors, red, orange, green and blue in each of the graphs), and Stokes parameters from all four revolutions were averaged together for the values reported in the bottom half of Table 4.3.

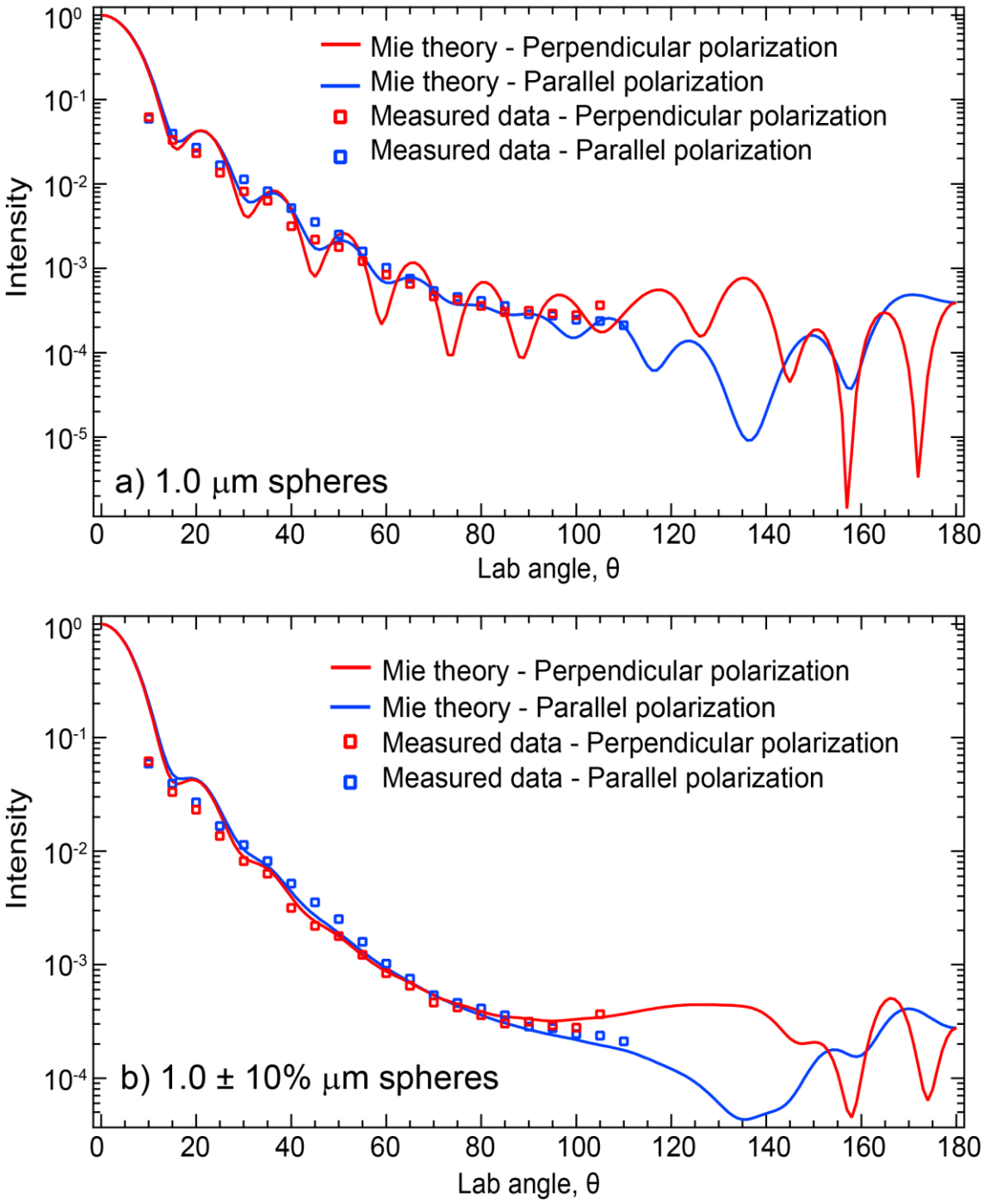

Figure 4.5. Measured light scattering intensity (S_0) versus laboratory angle, θ, for 1.0 μm polystyrene spheres shown with Mie theory calculations for both perpendicularly and parallel polarized light. In panel (a), Mie theory calculations were performed with a monodisperse distribution of spheres with 1.0 μm radius. In panel (b), Mie theory calculations were performed with a polydisperse sample of spheres with a Gaussian distribution of radii with a standard deviation of 10% about the mean.

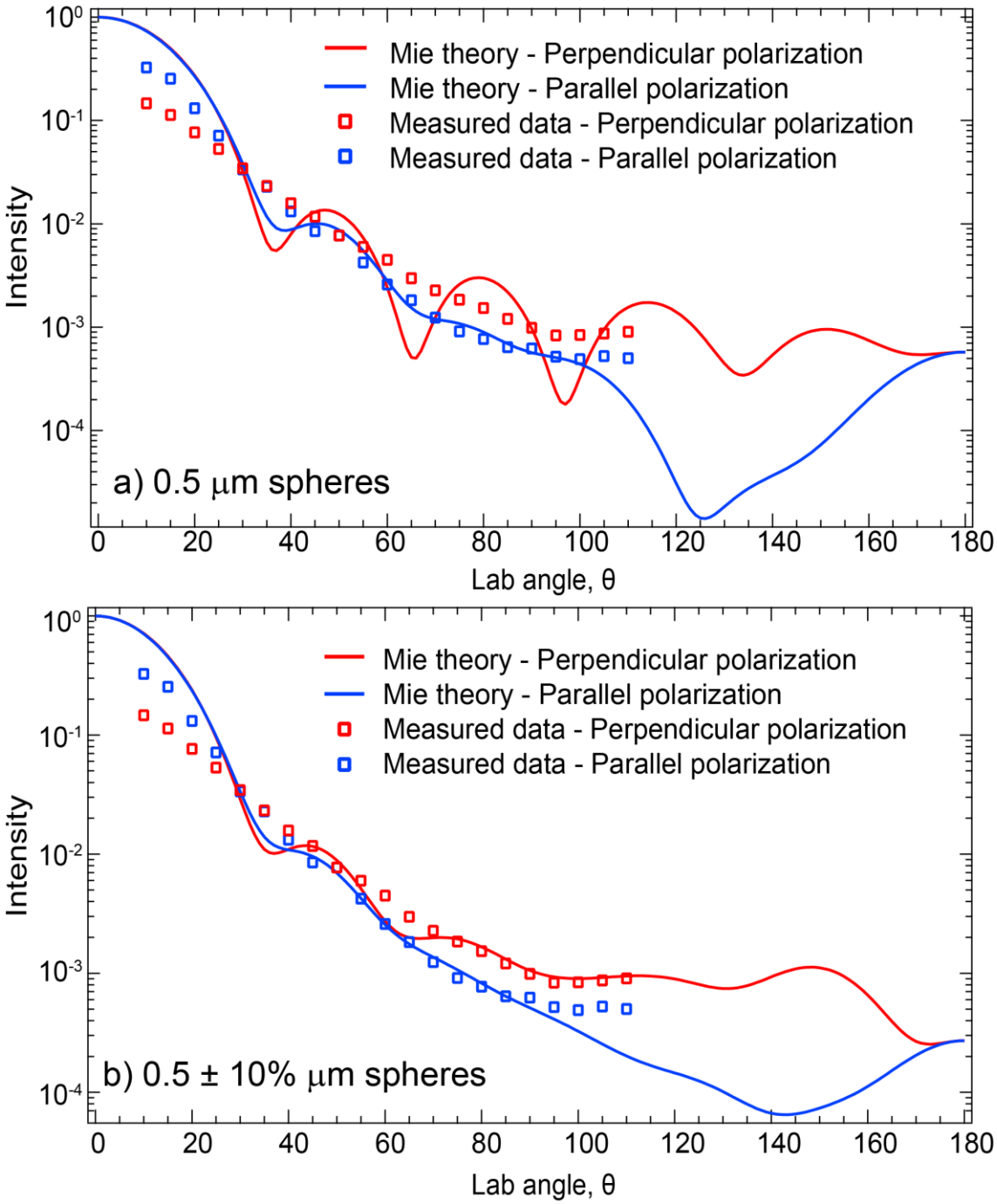

Figure 4.6. Measured light scattering intensity (S_0) versus laboratory angle, θ, for 0.5 μm polystyrene spheres shown with Mie theory calculations for both perpendicularly and parallel polarized light. In panel (a), Mie theory calculations were performed with a monodisperse distribution of spheres with 0.5 μm radius. In panel (b), Mie theory calculations were performed with a polydisperse sample of spheres with a Gaussian distribution of radii with a standard deviation of 10% about the mean.

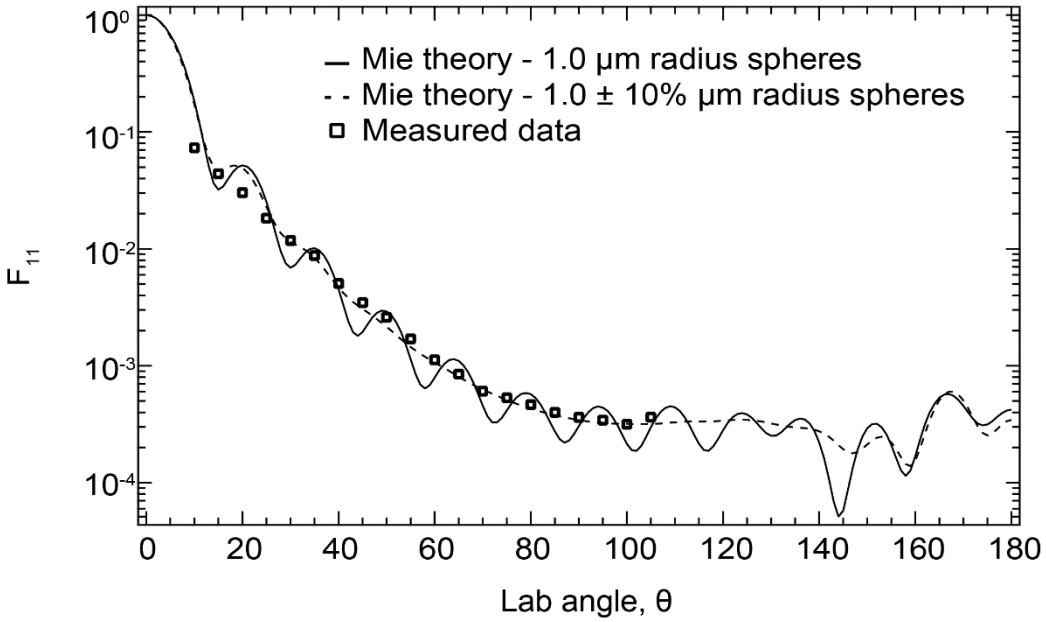

Figure 4.7. Measurements of the scattering matrix element F_{11} versus laboratory angle, θ, for 1.0 μm spheres shown with Mie theory calculations for both a monodisperse (solid lines) and a polydisperse (dashed lines) sample of spheres.

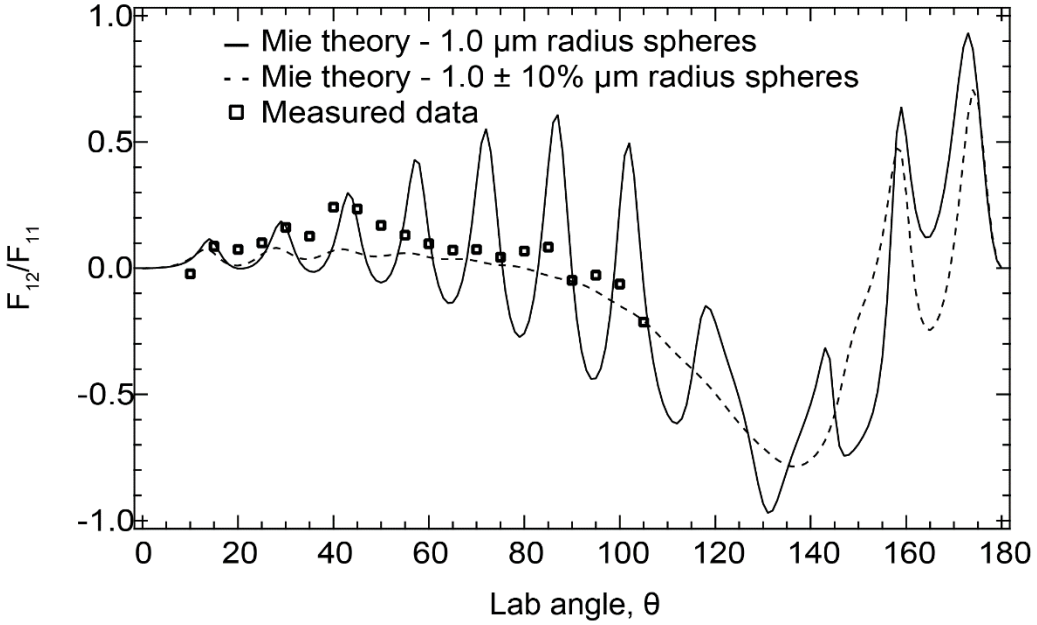

Figure 4.8. Measurements of the ratio of scattering matrix elements F_{12}/F_{11} versus laboratory angle, θ, for 1.0 μm spheres shown with Mie theory calculations for both a monodisperse (solid lines) and a polydisperse (dashed lines) sample of spheres. Note that, being a ratio, the scaling constant for the scattering matrix cancels out and a direct comparison can be made between Mie theory and the measurements

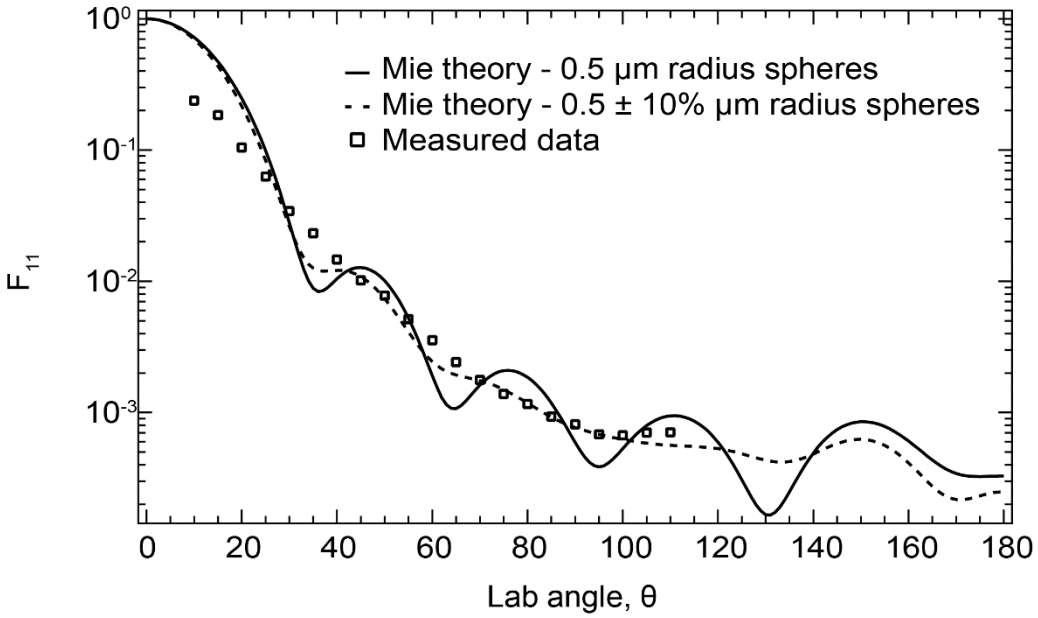

Figure 4.9. Measurements of the scattering matrix element F_{11} versus laboratory angle, θ, for 0.5 μm spheres shown with Mie theory calculations for both a monodisperse (solid lines) and a polydisperse (dashed lines) sample of spheres.

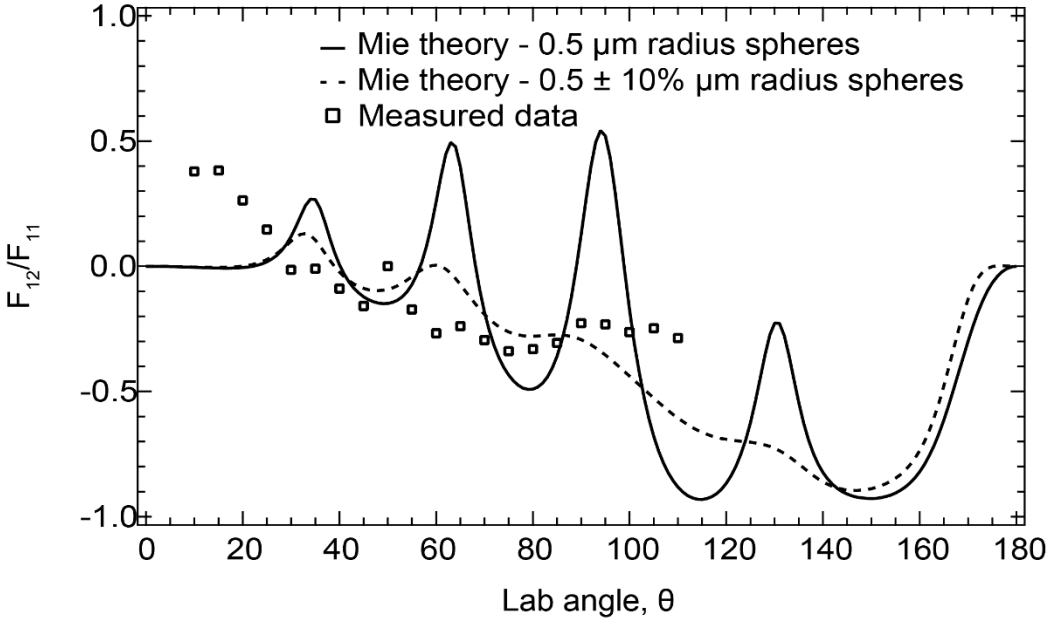

Figure 4.10. Measurements of the ratio of scattering matrix elements F_{12}/F_{11} versus laboratory angle, θ, for 0.5 μm spheres shown with Mie theory calculations for both a monodisperse (solid lines) and a polydisperse (dashed lines) sample of spheres. Note that, being a ratio, the scaling constant for the scattering matrix cancels out and a direct comparison can be made between Mie theory and the measurements.

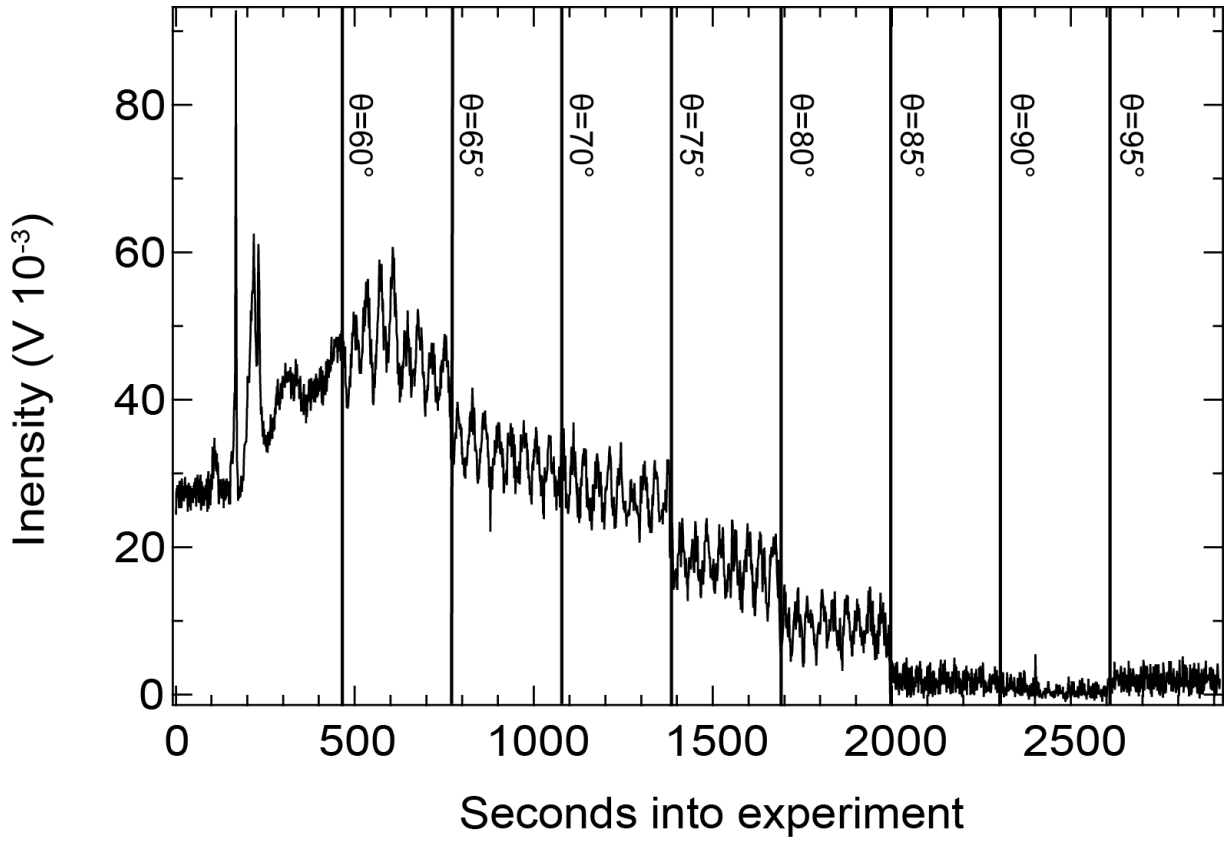

Figure 4.11. Measured scattering light intensity from photochemically-generated hydrocarbon aerosol vs. time elapsed from when the deuterium lamp is turned on in the reaction chamber. Intensity is in units of mV from the photodiode via the lock-in amplifier. Each step of the horizontal rotating stage, marked by a vertical line, lowers the intensity by a discrete amount (see text). Once the scattered intensity reaches a steady state at ~500 seconds, the quarter-wave plate is rotated to different angles, ϕ, signified by the oscillations of signal intensity for each step of the horizontal rotating stage. After two full revolutions of the quarter-wave plate, the polarimeter and photodiode are rotated to the next laboratory angle, θ, with respect to the incident laser beam.

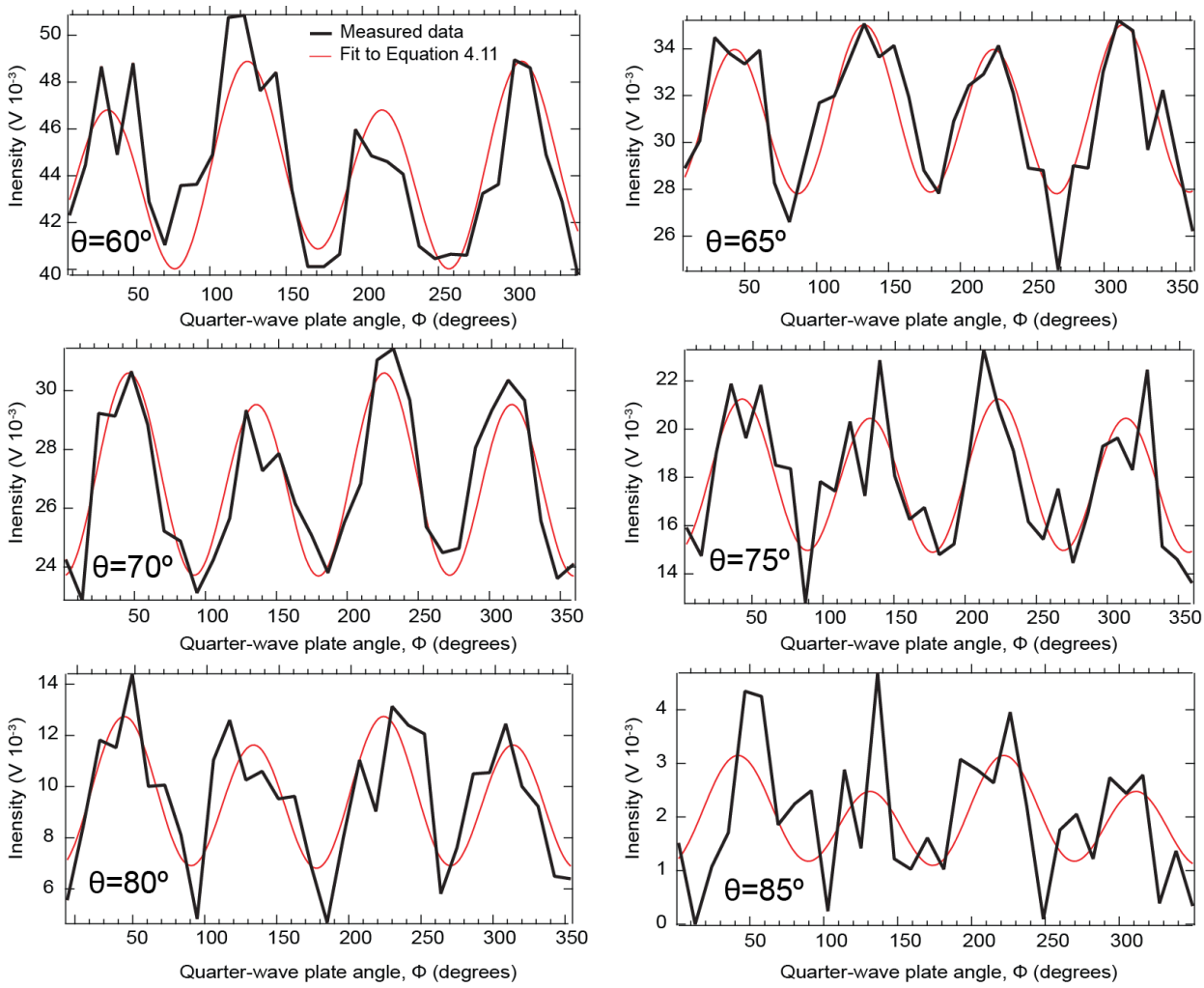

Figure 4.12. *In situ* scattering intensity (black lines) as a function of ϕ and θ corresponding to one full revolution (i.e., 360°), along with curve fits (red lines) to Equation 4.11 performed in Igor Pro. Stokes parameters and uncertainties derived from the curve fits are shown in Table 4.4.

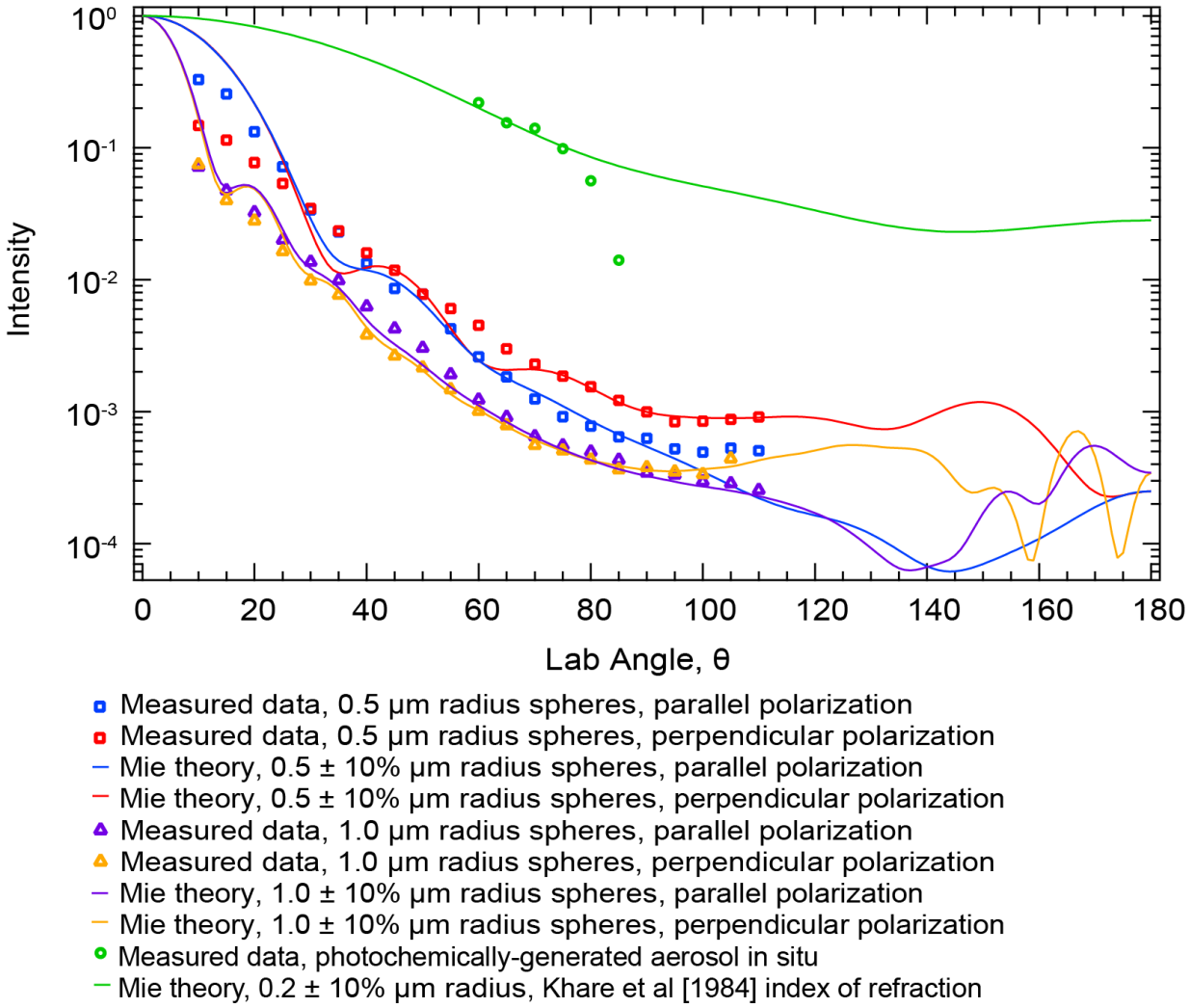

Figure 4.13. Comparison of measured light scattering intensity versus laboratory angle for polystyrene spheres and photochemically-generated aerosol. Measurements of polystyrene spheres are the same as those shown in Figure 4.5(b) for 1.0 µm radius spheres (purple and orange triangles) and Figure 4.6(b) for 0.5 µm radius spheres (blue and red squares) for both parallel and perpendicularly polarized light, along with Mie theory calculations performed with a polydisperse sample of spheres with a Gaussian distribution of radii with a standard deviation 10% about the mean (solid lines). *In situ* measurements (green circles) are compared with Mie theory calculations using 0.2 µm radius spheres, a real refractive index of n=1.70, and an imaginary refractive index of k=0.016 taken from *Khare et al.* [1984] for 613 nm.

Ádámkovics, M. (2004) Hydrocarbon photochemistry in planetary atmospheres: Laboratory and observational investigations of organic aerosols. University of California - Berkeley.

Ádámkovics, M., and K.A. Boering (2003) Photochemical formation rates of organic aerosols through time-resolved in situ laboratory measurements, *J. Geophys. Res.-Planets*, *108*, 5092, doi:10.1029/2002JE002028.

Anderson, C.M., and R.E. Samuelson (2011) Titan's aerosol and stratospheric ice opacities between 18 and 500 μm: Vertical and spectral characteristics from Cassini CIRS, *Icarus*, *212*, 762–778, doi:10.1016/j.icarus.2011.01.024.

Bellucci, A., B. Sicardy, P. Drossart, P. Rannou, P.D. Nicholson, M. Hedman, K.H. Baines, and B. Burrati (2009) Titan solar occultation observed by Cassini/VIMS: Gas absorption and constraints on aerosol composition, *Icarus*, *201*, 198–216, doi:10.1016/j.icarus.2008.12.024.

Bohren, C.F., and D.R. Huffman (2007) Absorption and scattering of light by small particles. Wiley-VCH Verlag GmbH, Weinheim, Germany.

Burgdorf, M., G. Orton, J. van Cleve, V. Meadows, and J. Houck (2006) Detection of new hydrocarbons in Uranus' atmosphere by infrared spectroscopy, *Icarus*, *184*, 634–637, doi:10.1016/j.icarus.2006.06.006.

Chu, E.F. (2013) Experimental investigations of photochemically-generated organic aerosols and applications to early Earth and Mars. University of California - Berkeley.

Croteau, P. (2010) Nitrous oxide and molecular nitrogen isotopic compositions and aerosol optical properties: experiments and observations relevant to planetary atmospheres. University of California - Berkeley.

Domagal-Goldman, S.D., J.F. Kasting, D.T. Johnston, and J. Farquhar (2008) Organic haze, glaciations and multiple sulfur isotopes in the Mid-Archean Era, *Earth Planet. Sci. Lett.*, *269*, 29–40, doi:10.1016/j.epsl.2008.01.040.

Gillett, F.C., and W.J. Forrest (1974) 7.5- to 13.5-micron spectrum of Saturn, *Astrophys. J.*, *187*, L37–L39, doi:10.1086/181387.

Goldstein, D. (2003) Polarized Light. Marcel Dekker, New York.

Hadamcik, E., J.-B. Renard, A. Mahjoub, T. Gautier, N. Carrasco, G. Cernogora, and C. Szopa (2013) Optical properties of analogs of Titan's aerosols produced by dusty plasma, *Earth Planets Space*, *65*, 1175–1184, doi:10.5047/eps.2013.05.019.

Haqq-Misra, J.D., S.D. Domagal-Goldman, P.J. Kasting, and J.F. Kasting (2008) A revised, hazy methane greenhouse for the Archean Earth, *Astrobiology*, *8*, 1127–1137, doi:10.1089/ast.2007.0197.

Hasenkopf, C.A., M.R. Beaver, M.G. Trainer, H.L. Dewitt, M.A. Freedman, O.B. Toon, C.P. McKay, and M.A. Tolbert (2010) Optical properties of Titan and early Earth haze laboratory analogs in the mid-visible, *Icarus*, *207*, 903–913, doi:10.1016/j.icarus.2009.12.015.

Imanaka, H., D.P. Cruikshank, B.N. Khare, and C.P. McKay (2012) Optical constants of Titan tholins at mid-infrared wavelengths (2.5-25 μm) and the possible chemical nature of Titan's haze particles, *Icarus, 218,* 247–261, doi:10.1016/j.icarus.2011.11.018.

Imanaka, H., B.N. Khare, J.E. Elsila, E.L.O. Bakes, C.P. McKay, D.P. Cruikshank, S. Sugita, T. Matsui, and R.N. Zare (2004) Laboratory experiments of Titan tholin formed in cold plasma at various pressures: implications for nitrogen-containing polycyclic aromatic compounds in Titan haze, *Icarus, 168,* 344–366, doi:10.1016/j.icarus.2003.12.014.

Karkoschka, E. (2011) Neptune's cloud and haze variations 1994-2008 from 500 HST-WFPC2 images, *Icarus, 215,* 759–773, doi:10.1016/j.icarus.2011.06.010.

Kasting, J.F. (2005) Methane and climate during the Precambrian era, *Precambrian Res., 137,* 119–129, doi:10.1016/j.precamres.2005.03.002.

Kasting, J.F. (2013) How was early Earth kept warm?, *Science, 339,* 44–45, doi:10.1126/science.1232662.

Kasting, J.F., K.J. Zahnle, and J.C.G. Walker (1983) Photochemistry of methane in Earth's early atmosphere, *Precambrian Res., 20,* 121–148, doi:10.1016/0301-9268(83)90069-4.

Khare, B.N., C. Sagan, E.T. Arakawa, F. Suits, T.A. Callcott, and M.W. Williams (1984) Optical constants of organic tholins produced in a simulated titanian atmosphere: from soft x-ray to microwave frequencies, *Icarus, 60,* 127–137, doi:10.1016/0019-1035(84)90142-8.

Kim, S.J., J. Caldwell, A.R. Rivolo, R. Wagener, and G.S. Orton (1985) Infrared polar brightening on Jupiter: 3. Spectrometry from the Voyager 1 IRIS experiment, *Icarus, 64,* 233–248, doi:10.1016/0019-1035(85)90088-0.

Kim, S.J., and R. Courtin (2013) Spectral characteristics of the Titanian haze at 1-5 micron from Cassini/VIMS solar occultation data, *Astron. Astrophys., 557,* L6, doi:10.1051/0004-6361/201322173.

De Kok, R., P.G.J. Irwin, N.A. Teanby, C.A. Nixon, D.E. Jennings, L. Fletcher, C. Howett, S.B. Calcutt, N.E. Bowles, F.M. Flasar, and F.W. Taylor (2007) Characteristics of Titan's stratospheric aerosols and condensate clouds from Cassini CIRS far-infrared spectra, *Icarus, 191,* 223–235, doi:10.1016/j.icarus.2007.04.003.

Kostogryz, N.M. (2013) Time variations of aerosol properties in the atmosphere of Uranus, *Sol. Syst. Res., 47,* 24–30, doi:10.1134/S0038094612060044.

Laven, P. (2003) Simulation of rainbows, coronas, and glories by use of Mie theory, *Appl. Opt., 42,* 436–444, doi:10.1364/AO.42.000436.

Lavvas, P., R.V. Yelle, and C.A. Griffith (2010) Titan's vertical aerosol structure at the Huygens landing site: Constraints on particle size, density, charge, and refractive index, *Icarus, 210,* 832–842, doi:10.1016/j.icarus.2010.07.025.

Mahjoub, A., N. Carrasco, P.-R. Dahoo, T. Gautier, C. Szopa, and G. Cernogora (2012) Influence of methane concentration on the optical indices of Titan's aerosols analogues, *Icarus, 221,* 670–677, doi:10.1016/j.icarus.2012.08.015.

Maltsev, V.P., A.V. Chernyshev, K.A. Semyanov, and E. Soini (1996) Absolute real-time measurement of particle size distribution with the flying light-scattering indicatrix method, *Appl. Opt., 35*, 3275–3280, doi:10.1364/AO.35.003275.

McKay, C.P., J.B. Pollack, and R. Courtin (1991) The greenhouse and antigreenhourse effects on Titan, *Science, 253*, 1118–1121, doi:10.1126/science.11538492.

Moses, J.I., K. Rages, and J.B. Pollack (1995) An analysis of Neptune stratospheric haze using high-phase-angle Voyager images, *Icarus*, *113*, 232–266, doi:10.1006/icar.1995.1022.

Pavlov, A.A., L.L. Brown, and J.F. Kasting (2001) UV shielding of NH_3 and O_2 by organic hazes in the Archean atmosphere, *J. Geophys. Res.-Planets*, *106*, 23267–23287, doi:10.1029/2000JE001448.

Ramirez, S.I., P. Coll, A. da Silva, R. Navarro-Gonzalez, J. Lafait, and F. Raulin (2002) Complex refractive index of Titan's aerosol analogues in the 200-900 nm domain, *Icarus*, *156*, 515–529, doi:10.1006/icar.2001.6783.

Rannou, P., T. Cours, S. Le Mouelic, S. Rodriguez, C. Sotin, P. Drossart, and R. Brown (2010) Titan haze distribution and optical properties retrieved from recent observations, *Icarus*, *208*, 850–867, doi:10.1016/j.icarus.2010.03.016.

Roman, M.T., D. Banfield, and P.J. Gierasch (2013) Saturn's cloud structure inferred from Cassini ISS, *Icarus*, *225*, 93–110, doi:10.1016/j.icarus.2013.03.015.

Sagan, C. and C. Chyba (1997) The early faint sun paradox: Organic shielding of ultraviolet-labile greenhouse gases, *Science*, *276*, 1217-1221, doi: 10.1126/science.276.5316.1217.

Sciamma-O'Brien, E., P.-R. Dahoo, E. Hadamcik, N. Carrasco, E. Quirico, C. Szopa, and G. Cernogora (2012) Optical constants from 370 nm to 900 nm of Titan tholins produced in a low pressure RF plasma discharge, *Icarus*, *218*, 356–363, doi:10.1016/j.icarus.2011.12.014.

Smith, B.A., L. Soderblom, R. Beebe, J. Boyce, G. Briggs, A. Bunker, S.A. Collins, C.J. Hansen, T.V. Johnson, J.L. Mitchell, R.J. Terrile, M. Carr, A.F. Cook, J. Cuzzi, J.B. Pollack, G.E. Danielson, A. Ingersoll, M.E. Davies, G.E. Hunt, H. Masursky, E. Shoemaker, D. Morrison, T. Owen, C. Sagan, J. Veverka, R. Strom, and V.E. Suomi (1981) Encounter with Saturn - Voyager 1 imaging science results, *Science*, *212*, 163–191, doi:10.1126/science.212.4491.163.

Tomasko, M.G., B. Archinal, T. Becker, B. Bezard, M. Bushroe, M. Combes, D. Cook, A. Coustenis, C. de Bergh, L.E. Dafoe, L. Doose, S. Doute, A. Eibl, S. Engel, F. Gliem, B. Grieger, K. Holso, E. Howington-Kraus, E. Karkoschka, H.U. Keller, R. Kirk, R. Kramm, M. Kuppers, P. Lanagan, E. Lellouch, M. Lemmon, J. Lunine, E. McFarlane, J. Moores, G.M. Prout, B. Rizk, M. Rosiek, P. Rueffer, S.E. Schroder, B. Schmitt, C. See, P. Smith, L. Soderblom, N. Thomas, and R. West (2005) Rain, winds and haze during the Huygens probe's descent to Titan's surface, *Nature*, *438*, 765–778, doi:10.1038/nature04126.

Tomasko, M.G., L. Doose, S. Engel, L.E. Dafoe, R. West, M. Lemmon, E. Karkoschka, and C. See (2008) A model of Titan's aerosols based on measurements made inside the atmosphere, *Planet. Space Sci.*, *56*, 669–707, doi:10.1016/j.pss.2007.11.019.

Trainer, M.G. (2013) Atmospheric prebiotic chemistry and organic hazes, *Curr. Org. Chem.*, *17*, 1710–1723.

Tran, B.N., J.C. Joseph, J.P. Ferris, P.D. Persans, and J.J. Chera (2003) Simulation of Titan haze formation using a photochemical flow reactor - The optical constants of the polymer, *Icarus*, *165*, 379–390, doi:10.1016/S0019-1035(03)00209-4.

Tran, B.N., J.C. Joseph, M. Force, R.G. Briggs, V. Vuitton, and J.P. Ferris (2005) Photochemical processes on Titan: Irradiation of mixtures of gases that simulate Titan's atmosphere, *Icarus*, *177*, 106–115, doi:10.1016/j.icarus.2005.03.015.

Vinatier, S., B. Bezard, C.A. Nixon, A. Mamoutkine, R.C. Carlson, D.E. Jennings, E.A. Guandique, N.A. Teanby, G.L. Bjoraker, F.M. Flasar, and V.G. Kunde (2010) Analysis of Cassini/CIRS limb spectra of Titan acquired during the nominal mission I. Hydrocarbons, nitriles and CO_2 vertical mixing ratio profiles, *Icarus*, *205*, 559–570, doi:10.1016/j.icarus.2009.08.013.

Vinatier, S., P. Rannou, C.M. Anderson, B. Bezard, R. de Kok, and R.E. Samuelson (2012) Optical constants of Titan's stratospheric aerosols in the 70-1500 cm^{-1} spectral range constrained by Cassini/CIRS observations, *Icarus*, *219*, 5–12, doi:10.1016/j.icarus.2012.02.009.

Vuitton, V., B.N. Tran, P.D. Persans, and J.P. Ferris (2009) Determination of the complex refractive indices of Titan haze analogs using photothermal deflection spectroscopy, *Icarus*, *203*, 663–671, doi:10.1016/j.icarus.2009.04.016.

Wolf, E.T., and O.B. Toon (2010) Fractal organic hazes provided an ultraviolet shield for early Earth, *Science*, *328*, 1266–1268, doi:10.1126/science.1183260.

Yung, Y.L., and W.B. Demore (1999) Photochemistry of planetary atmospheres. Oxford University Press, New York.

Zhang, X., R.A. West, D. Banfield, and Y.L. Yung (2013) Stratospheric aerosols on Jupiter from Cassini observations, *Icarus*, *226*, 159–171, doi:10.1016/j.icarus.2013.05.020.

Chapter 5

Design and first results of a new apparatus to produce N_2O by corona discharge in air for measurements of its isotopic composition

5.1 Introduction

Nitrous oxide (N_2O) is a potent greenhouse gas with a 120-year lifetime. The sources of N_2O to the atmosphere are both natural and anthropogenic, including production by microbes in the oceans and in soils and fossil fuel and biomass burning, while the main sink is photolysis in the stratosphere [*IPCC*, 2013]. The mixing ratio of N_2O in the atmosphere has increased by 20% since 1750, largely due to the increased use of nitrogen-based fertilizers as world population and therefore agriculture have grown [e.g., *Park et al.*, 2012; *IPCC*, 2013]. Observations of N_2O mixing ratios have been used to infer the sources and magnitudes of fluxes of N_2O to the atmosphere [*Hirsch et al.*, 2006; *Huang et al.*, 2008], and measurements of the isotopic composition of N_2O hold the promise of providing additional constraints and reducing uncertainties [e.g., *Sowers et al.*, 2002; *Röckmann et al.*, 2003; *Röckmann and Levin*, 2005; *Park et al.*, 2012]. Recently, *Park et al.* [2012] measured the concentration and isotopic composition of N_2O in firn air samples from Antarctica and archived air samples from Cape Grim, Tasmania, from 1978 to 2005 and used the measured trends and seasonal cycles in the isotopic composition of N_2O, including the $^{18}O/^{16}O$ ratio, the average $^{15}N/^{14}N$ ratio, and the "site-specific" $^{15}N/^{14}N$ ratio (i.e., the relative enrichment or depletion in ^{15}N at the central N atom versus the terminal N atom in N_2O), to demonstrate empirically that an increase in the use of nitrogen-based fertilizers for agriculture is indeed the major cause of the increase in concentration of N_2O since the 1940s. However, further measurements and analyses of both N_2O mixing ratios and isotopic composition are needed to gain a more mechanistic understanding of the magnitudes of the fluxes of N_2O from both anthropogenic and natural sources and to monitor how they may change over time as climate changes.

One source of N_2O to the atmosphere for which relatively little is known is production in air by corona discharge, which is a plasma discharge caused by ionization of gases in a high-voltage gradient, which can occur in high-voltage environments such as thunderstorms. Corona discharge has previously been shown to produce N_2O in the laboratory in N_2 and O_2 gas mixtures [*Donohoe et al.*, 1977; *Hill et al.*, 1988; *Brandvold et al.*, 1996; *Nna Mvondo et al.*, 2001]. Kinetics modeling of processes relevant for a corona discharge, such as electronic excitation, electron impact, electron attachment, and electron-ion, ion-molecule, and ion-ion reactions, have also suggested that significant amounts of N_2O can be formed in a corona discharge [*Bhetanbhotla et al.*, 1985; *Kossyi et al.*, 1992], and calculations of the production of N_2O by lightning in the atmosphere suggest that significant amounts of N_2O can be produced in thunderstorms on a local scale [*Griffing*, 1977; *Hill et al.*, 1984]. Field measurements during thunderstorms have also shown increased levels of N_2O attributed to corona discharge [*Levine and Shaw*, 1983; *Brandvold et al.*, 1996]. While thunderstorms are only a small source of N_2O globally [*IPCC*, 2013], if the isotopic signature of N_2O formed by corona discharge is greatly different from the isotopic composition of background N_2O in the troposphere or of the various sources or sinks of N_2O, then the effect of contributions of N_2O formed by corona discharge on the isotopic composition of tropospheric N_2O and how such a source may have changed over time could be potentially important for interpreting long-term trends and/or seasonal cycles in the isotopic composition of atmospheric N_2O measured

over time, such as those in *Park et al.* [2012]. Indeed, it is thought, for example, that the frequency and severity of thunderstorms will increase because of enhanced global radiative forcing associated with elevated greenhouse gas concentrations [e.g., *Trapp et al.*, 2007; *Diffenbaugh et al.*, 2013].

Together, several studies in particular motivate the work presented in this chapter to measure the isotopic composition of N_2O formed by corona discharge in air in order to assess its possible relevance to the isotopic composition of atmospheric N_2O. First, *Wofsy* [2011] recently discovered large enhancements in N_2O mixing ratios over large regions of the upper troposphere in the Southern Hemisphere during the HIAPER (High-performance Instrumented Airborne Platform for Environmental Research) Pole-to-Pole Observations (HIPPO) campaign, suggesting the presence of unaccounted-for tropical sources of N_2O. Production of N_2O by biomass burning or by corona discharge could potentially result in such upper tropospheric enhancements. Second, two previous laboratory studies have shown very large enrichments in ^{15}N in the gaseous species formed by electric discharges relative to the initial N_2. *Manuccia and Clark* [1976] used a pulsed glow discharge in N_2 and O_2 at 77 K to form nitrogen oxides (e.g., NO, N_2O, NO_2) with enrichments in the $^{15}N/^{14}N$ ratio measured by magnetic sector mass spectrometry as high as 21% relative to the starting N_2. *Gorshunov and Gudenko* [2003] used a pulsed discharge in N_2 and measured up to 30-fold enrichments in ^{15}N atoms measured by electron spin resonance spectroscopy in the "post-discharge zone" of their apparatus. Enrichments this large in the $^{15}N/^{14}N$ ratio in N_2O, if verified by modern isotope ratio mass spectrometry and specifically for N_2O gas, would make detection of N_2O production by corona discharge feasible in future atmospheric field studies and would motivate inclusion of such a highly enriched ^{15}N source of N_2O to the atmosphere in atmospheric models.

To measure whether the isotopic composition of N_2O formed by corona discharge is significantly different from atmospheric N_2, O_2, and background tropospheric N_2O, a new apparatus was designed and constructed to produce a corona discharge in dry, purified air and to collect the N_2O produced cryogenically for subsequent analysis by isotope ratio mass spectrometry (IRMS). In Section 5.2, the design and construction of the corona discharge apparatus are described, as well as the experimental methods for testing and verifying the formation of N_2O with the apparatus. In Section 5.3, preliminary results of measurements of the isotopic composition of N_2O formed by the corona discharge apparatus are presented and discussed. In Section 5.4, a brief summary is given.

5.2 Design, construction, and preliminary testing of the corona discharge apparatus

Corona discharge occurs when gas in an area with a high voltage gradient is ionized, forming a plasma. Free electrons are accelerated by the high voltage gradient and collide with surrounding gas molecules, causing ionization and dissociation via electron impact. Additional electrons created by ionizing gases are also accelerated by the gradient, causing additional electron-molecule collisions, thus sustaining the discharge. Photons are emitted by the relaxation of excited molecules, causing the characteristic bluish glow associated with a corona, and additional ionization and dissociation can occur when the photons are in the high-energy UV range [*Chen and Davidson*, 2002]. Compared to spark discharges, corona discharge is a low current process (typically microamperes, although the voltage is typically in the kilovolts range) and therefore the temperatures of the surrounding gas are much colder. Many different mechanisms for the formation of N_2O via various ground and excited state species containing oxygen and

nitrogen present in high energy environments such as corona, have been proposed, as shown in Table 5.1, but the exact mechanism by which N_2O is formed in a corona discharge is unknown.

In order to generate N_2O by corona discharge for measurements of its isotopic composition, the experimental setup shown schematically in Figure 5.1 was designed and built. Reactant gases originate from a cylinder of high-purity zero air (Ultra Zero grade, Praxair, Danbury, CT), the flow from which is controlled by changing the regulator delivery pressure and by restricting flow with a needle valve. Gases from this cylinder pass through a 12-cm-long corona discharge cell, which consists of a 100 μm diameter tungsten wire suspended coaxially within a 2 cm diameter stainless steel cylinder. The tungsten wire is connected to the output from a high-voltage power supply (MJ10P1500, Glassman High Voltage, High Bridge, NJ) controlled by a low voltage power supply (1651A, B&K Precision, Yorba Linda, CA) to an output of 5 kV and 1.5 mA maximum. The stainless steel cylinder is grounded through a picoammeter (6485, Keithley Instruments, Cleveland, OH), which monitors the current passing through the stainless steel cylinder. The voltage difference between the wire and the cylinder creates a corona discharge through which the reactant gases flow. Although the flow rate, and therefore the residence time in the discharge cell, is not measured directly, the pressure of the system is monitored by a convection pressure gauge (317, MKS Instruments, Andover, MA, calibrated for air) mounted ~30 cm downstream from the discharge cell. After passing through the discharge chamber, the gas mixture passes through two scrubbing materials, which are present to remove unwanted by-products of the corona discharge from the gas stream. The first scrubbing material is ascarite (sodium hydroxide coated silica; Sigma-Aldrich, St. Louis, MO), which removes NO_x from the gas mixture (and any residual CO_2 in the zero air), and the second scrubbing material is silver wool (Sigma-Aldrich), which removes ozone from the gas mixture. Next, the gas mixture passes through a Russian doll trap – a cryogenic trap consisting of nested curved glass tubing and a glass fiber thimble to create high surface area [*Brenninkmeijer and Röckmann*, 1996] – submerged in liquid nitrogen in order to trap any condensable species, particularly N_2O, while N_2 and O_2 continue downstream. A second pressure gauge – a capacitance manometer (Baratron, 10 Torr range, MKS Instruments) – is mounted downstream from the Russian doll trap followed by an evacuated stainless steel sample cylinder. The entire system is pumped down with a turbomolecular pump (CFV100, Alcatel Vacuum Technology) backed by a rough pump (E2M1.5, Edwards, Sanborn, NY).

To test for the formation of N_2O in the corona discharge, a quadrupole mass spectrometer in the form of a residual gas analyzer (RGA; Model 300, Stanford Research Systems, Sunnyvale, CA) replaced the sample cylinder downstream from the Russian doll trap. The RGA monitored several channels corresponding to different mass to charge ratios (m/z) relevant for the formation of N_2O: m/z = 12 for C, 14 for N, 18 for H_2O, 28 for N_2, 30 for NO, 32 for O_2, and 44 for CO_2/N_2O. This experiment had several stages. First, flow from the zero air cylinder was started with a regulator delivery pressure of 15 psi, and the pressure of the system reached a steady state as measured by the two online pressure gauges: 435 mTorr for the upstream gauge and 97 mTorr for the downstream gauge. Next, the high-voltage power supply was switched on, generating a corona discharge through which the reactant gas mixture was flowing. Then, after ~15 minutes, the Russian doll trap was submerged in liquid nitrogen, trapping any condensable species flowing out from the discharge cell and through the scrubbing materials. Next, after another ~15 minutes, the high-voltage power supply was switched off, stopping the corona discharge, and the Russian doll trap was allowed to warm up to room temperature, releasing the condensable species trapped.

The results from the mass spectrometric measurements of the gases flowing through the apparatus and as a function of time are shown in Figure 5.2. The most abundant species throughout

the experiment are N_2 and O_2 from the reactant zero air. When the corona is turned on, there is an immediate increase in the signals for mass to charge (m/z) 44 and 30, corresponding to N_2O and NO, respectively, which reach a steady state quickly. There was a concern that the channel for m/z 44 may have included interfering signal from CO_2, which has the same mass as N_2O, if there were any residual ambient CO_2 in the line or CO_2 impurities in the zero air (although the latter should also be trapped by the ascarite). However, because the signal for NO with m/z 30, which is a fragment ion of N_2O in the electron impact of the RGA, rises together with the signal for m/z 44, we conclude that m/z 44 comes from N_2O and not CO_2. When the Russian doll trap is submerged in liquid nitrogen, the signals for N_2O and NO drop down to levels at or below what they were before the corona was switched on, indicating these substances are being trapped by the cold temperatures in the Russian doll trap. When the corona is turned off and the Russian doll trap is allowed to warm to room temperature, the N_2O and NO signals sharply rise, indicating species sublimating and flowing into the RGA. These results demonstrate that N_2O can be formed in the corona discharge cell and is successfully trapped by the Russian doll trap.

5.3 Preliminary results for N_2O isotopic compositions formed by corona discharge

After the tests of N_2O production by the new apparatus were completed, the RGA mass spectrometer was removed and replaced with a 40 mL stainless steel sample cylinder used to isolate a sample of N_2O for IRMS measurements. Two different flow conditions were used for sample generation, and the experimental conditions are summarized in Table 5.2. Seven samples were generated under "low flow" conditions in which the regulator delivery pressure was 15 psi, and the steady state pressure of the system ranged from 520 mTorr to 578 mTorr for the upstream pressure gauge and 101 mTorr to 112 mTorr for the downstream pressure gauge, and one sample was generated under "high flow" conditions, in which the regulator delivery pressure was 25 psi, and the steady state pressure was 886 mTorr for the upstream pressure gauge and 166 mTorr for the downstream pressure gauge. Once the pressure had reached a steady state value, the high voltage power supply was switched on, thus starting the corona discharge, for 5 minutes prior to placing liquid nitrogen on the Russian doll trap. Then, liquid nitrogen was placed on the Russian doll trap for 2.5 minutes, trapping condensable species in the trap. Next, the valve to the zero air cylinder, the valve to the vacuum pump, and the upstream valve of the Russian doll trap were closed, isolating the sample between the Russian doll trap and sample cylinder. Liquid nitrogen was removed from the Russian doll trap and replaced with a liquid-nitrogen/ethanol slurry at -95° C, and liquid nitrogen was placed on the sample cylinder, in order to revolatilize N_2O in the Russian doll trap while keeping high-boiling-point species such as water in the trap and to condense N_2O in the sample cylinder. After 10 minutes, the downstream valve was closed on the Russian doll trap, and the valve to the vacuum pump was opened for 5 minutes to remove any residual non-condensed gases. Then, the valve to the vacuum pump was closed, and liquid nitrogen was removed from the sample cylinder, which was then allowed to warm up to room temperature. Finally, the pressure of the sample cylinder was measured by the capacitance monometer. The sample cylinder was then closed, removed from the line, and mounted on a separate gas transfer vacuum line maintained by an oil diffusion pump. Using the gas transfer line, gases from the sample cylinder were expanded into either two or four 20 mL glass tubes for analysis of the N_2O isotopic composition by a Finnigan 252 isotope ratio mass spectrometer operated in continuous flow mode [See *Croteau*, 2010; *Croteau et al.*, 2010; *Park et al.*, 2012]. Prior to measuring a sample of N_2O generated by corona discharge, an air sample was collected at ground level on the UC – Berkeley campus (referred to as "campus air" in the results below), and the isotopic

composition of N_2O in the air sample was measured in order to assess the accuracy and stability of the IRMS on a given day.

Due to the low abundances of rare isotopologues (e.g., $^{15}N^{14}N^{16}O$ and $^{14}N^{14}N^{18}O$), isotopic compositions are typically measured as the ratio of the rare isotopologue to the common isotopologue because the ratio can be measured much more precisely than the absolute abundances. Furthermore, measurements are taken relative to a working standard that is calibrated beforehand against international isotope standards in order to compare isotopic composition measurements between different laboratories and instruments. Therefore, isotopic compositions are typically reported in δ-notation, which is a measure of deviation in parts per thousand (or per mil, denoted by the symbol "‰") of the ratio of rare to common isotopes of a sample over the ratio of rare to heavy isotopes of a standard, as given in Equation 5.1 for the $^{15}N/^{14}N$ ratio.

$$\delta^{15}N = \{[(^{15}N/^{14}N)_{sample} / (^{15}N/^{14}N)_{standard}] - 1 \} \times 1000 \text{ ‰} \quad (5.1)$$

The isotope ratio mass spectrometer, run in continuous flow mode with a preconcentrator and gas chromatography (GC) column to preconcentrate N_2O and separate it from other gases in a sample, is capable of determining $\delta^{15}N$ and $\delta^{18}O$ in a single measurement by measuring the ratio of N_2O^+ signals at m/z 44, 45, and 46. A separate measurement can be done to determine the so-called site-specific ^{15}N isotopic composition, i.e., the isotopic composition at the central N atom (N^{α}), which is denoted $\delta^{15}N^{\alpha}$ and the terminal N atom (N^{β}), which is denoted $\delta^{15}N^{\beta}$, by measuring the ratio of NO^+ fragment ion signals in the IRMS at m/z 30 and 31 at the GC retention time for N_2O. Historically, the single measurement precisions (1σ) for N_2O isotope measurements in our laboratory are 0.2‰ for $\delta^{15}N$ and $\delta^{18}O$ and 0.8 and 0.9‰ for $\delta^{15}N^{\alpha}$ and $\delta^{15}N^{\beta}$, respectively. Ideally, different aliquots of the same sample would be used for the N_2O^+ and the NO^+ in order to in principle derive the most precise site-specific $\delta^{15}N$ values. However, the N_2O^+ and the NO^+ runs cannot be done on a single day due to constraints of operating the IRMS properly and the means for long term storage of samples (i.e., longer than one day) discussed here were not always available; thus, aliquots of the same sample were not always available for both of the two separate measurements required for $\delta^{15}N$ and $\delta^{18}O$ and for $\delta^{15}N^{\alpha}$. Therefore, a "mix and match" approach was used in this first set of results for which measurements for m/z = 44, 45, 46 for 'low flow' or 'high flow' samples through the corona discharge were paired with the available 'low flow' or 'high flow' samples run for m/z = 30, 31.

The isotopic compositions of N_2O in campus air and corona discharge samples are shown in Table 5.3, and Table 5.4 summarizes the most important aspects and are discussed below. The enormous ^{15}N enrichments inferred in the previous two studies on nitrogen atoms and nitrogen oxides in a discharge [*Manuccia and Clark*, 1976; *Gorshunov and Gudenko*, 2003] are clearly not observed. Rather, much more modest differences between the $^{15}N/^{14}N$ ratio in the N_2O formed by corona discharge and the starting N_2 isotopic composition are measured. Indeed, all the runs at both 'low flow' and 'high flow' conditions yield values for $\delta^{15}N$ for N_2O formed by corona discharge that are within a few per mil of the starting isotopic composition of N_2, which we estimate to be 0 to +2‰ on the air N_2 scale (based on measurements by *Severinghaus et al.* [2003] of high purity N_2 cylinders for which the commercial air reduction process results in small enrichments in $\delta^{15}N$ of typically 2‰, while zero air is even less likely to be isotopically fractionated). Thus, at least under the conditions and protocol of these initial experiments, we see no evidence for large isotope effects in the chemistry of the corona discharge that result in large enrichments in ^{15}N in the N_2O produced. Differences with respect to the earlier experiments may

be the result of using a different type of discharge (earlier experiments used a glow or a spark discharge) or the extremely low temperature of 77 K used in the *Manuccia and Clark* [1976] experiment (and it is well-known that isotope effects are in general much larger at lower temperatures, as *Manuccia and Clark* [1976] discuss), the result of very different sampling conditions and/or artifacts in our experiments or in theirs. A comparison of the $\delta^{15}N$ values for N_2O formed by corona discharge with those for tropospheric N_2O show that the corona discharge values are lower by about 2 to 7‰ (i.e., less enriched in ^{15}N). These values, if future experiments varying the corona discharge conditions yield similar results, are most likely not large enough to make a difference in the global N_2O isotope budget but might be interesting to look for in field studies for locally-produced N_2O in thunderstorms.

The results for $\delta^{18}O$ of N_2O produced by corona discharge shown in Tables 5.3 and 5.4 represent the first data available for oxygen isotope fractionation forming N_2O in a corona discharge. For the low flow conditions, $\delta^{18}O$ values for the corona discharge N_2O are enriched in ^{18}O by about 20‰ (or 2%) relative to the starting O_2 isotopic composition in the zero air tank (based on measurements by *Feilberg et al.* [2013] of our high purity O_2 cylinder for which the commercial air reduction process results in a small enrichment in $\delta^{18}O$ of 3.0±0.2‰ relative to air O_2, while zero air is even less likely to be isotopically fractionated) and are a few per mil enriched relative to tropospheric N_2O. For the high flow conditions, however, the results are reversed: $\delta^{18}O$ values for the N_2O produced by corona discharge are within a few per mil of the starting O_2 isotopic composition and are depleted in ^{18}O by about 20‰ relative to tropospheric N_2O. Further testing of various experimental conditions are clearly warranted to understand the dependence of the ^{18}O composition on experimental conditions shown by these preliminary results, as discussed further below. In addition, given all the possible reactions involving ozone in Table 5.1, it would also be highly desirable to measure the ^{17}O isotopic composition of N_2O formed in the discharge (which requires heating N_2O on a gold catalyst and then measuring the O_2 produced by dual inlet IRMS [e.g., *Cliff and Thiemens*, 1997]), since ozone itself is highly enriched in both ^{17}O and ^{18}O in a non-mass-dependent manner [e.g., *Mauersberger et al.*, 2003; *Thiemens et al.*, 2012; *Feilberg et al.*, 2013]. Such ^{17}O measurements could provide some important new mechanistic information about N_2O formation pathways and why or why not N_2O in the experiments presented here are depleted, not enriched, in ^{18}O.

As for $\delta^{18}O$, the results for the site-specific ^{15}N isotopic compositions shown in Tables 5.3 and 5.4 also represent the first data available for N_2O produced in a corona discharge in air. For the low flow conditions, the so-called ^{15}N site preference values (i.e., $\delta^{15}N^{\alpha} - \delta^{15}N^{\beta}$) show enrichments at the central N atom relative to the terminal N atom in N_2O of about 20 to 25‰ relative to the starting N_2 (which, by definition – and necessity since the N atoms are indistinguishable in N_2 – is 0). For the high flow conditions, the ^{15}N site preference is even higher, at 40‰, and is similar to site preference measurements for tropospheric N_2O. From the variety of possible reactions in Table 5.1, it is not surprising that there are likely to be isotope effects that lead to enrichments or depletions at the terminal versus the central N atoms in the reactions that form (and destroy) N_2O in a corona discharge, as such isotope effects are also known, of course, in stratospheric photolysis and in the different microbial pathways that lead to N_2O production (i.e., ^{15}N site preference is different for N_2O produced by nitrification than that by denitrification) (See *Park et al.* [2012] and references therein.) As noted for the $\delta^{18}O$ results above, further testing of various experimental conditions are needed to understand the dependence of the site-specific $\delta^{15}N$ values on the high flow and low flow conditions measured here.

Notably, the combined results for $\delta^{15}N$, site-specific $\delta^{15}N$, and $\delta^{18}O$ do not appear to be consistent with a varying amount of N_2O leaking in from the atmosphere or with collection of residual N_2O from the zero air tank, nor simply with isotope fractionation due to sample collection artifacts, although these potential problems should certainly be followed up with additional experiments and testing. Rather, the differences measured between low flow and high flow conditions likely indicate that the isotopic composition, and by extension, the underlying chemistry in the corona discharge are sensitive to the experimental conditions. Changing the flow rate alters both the residence time of gases in the discharge chamber as well as the overall pressure of the entire system. *Manuccia and Clark* [1976] measured a significant pressure dependence in the ^{15}N enrichments in their glow discharge experiment due to the fact that the total energy deposition and the energy deposition per molecule decreased as the pressure increased, and they argued that these would be expected to result in differences in the magnitude of the isotope effects, as did their experiments at 300 and at 77 K. Thus, additional experiments with this new apparatus should be performed under different conditions for the corona discharge (e.g., mapping out the dependence of N_2O isotopic composition on zero air flow rate, system pressures, and corona discharge current), as well as the N_2O collection conditions and procedures. These additional tests should provide new information that will yield more mechanistic information on what controls the isotopic composition of N_2O produced by corona discharge.

5.4 Summary

In this chapter, the design, construction, and testing of an apparatus to form N_2O by corona discharge in air were presented. Preliminary tests showed the N_2O can indeed be produced and cryogenically collected by this apparatus. The first measurements of the isotopic composition of N_2O formed by corona discharge were performed. While they do not show the extremely large ^{15}N enrichments inferred in two previous experiments in a glow discharge [*Manuccia and Clark*, 1976] and in a spark discharge [*Gorshunov and Gudenko*, 2003], they do show results for N_2O isotopic compositions that, under some conditions, are significantly different from the isotopic composition of N_2 and O_2 reactants from which the N_2O is formed, and, under other conditions, are significantly different from background tropospheric N_2O. Additional measurements can now be pursued with this apparatus to explore how different experimental conditions affect the isotopic composition of N_2O formed by the corona discharge, and, ultimately, the possible influence corona discharge might have on the isotopic composition of N_2O in the atmosphere.

Table 5.1. Proposed mechanisms for N_2O formation via species present in high-energy environments, such as corona discharges

Reaction	References
$O_3^+ + N_2 \rightarrow N_2O^+ + O_2$ $O_3^+ + N_2 \rightarrow N_2O + O_2^+$	*Cacace et al.* [2001]; *Midey et al.* [2002]; *de Petris* [2003]
$O(^1D) + N_2 \rightarrow N_2O$	*Demore and Raper* [1962]; *Kajimoto and Cvetanović* [1976]; *Estupinan et al.* [2002]; *Prasad* [2002, 2005]
O_3* (vibrationally excited) + $N_2 \rightarrow N_2O + O_2$	*Estupinan et al.* [2002]
$N_2(A\ ^3\Sigma_u^+) + O_2 \rightarrow N_2O + O$	*Malcolme-Lawes* [1974]; *Zipf* [1980]; *Zipf and Prasad* [1980, 1982]; *Iannuzzi et al.* [1982]; *Fraser and Piper* [1989]
N_2* + O_2* $\rightarrow N_2O + O$	*Fraser et al.* [1990]
$N(^4S) + NO \rightarrow N_2 + O$	*Funke et al.* [2008]
$NO^+ + N \rightarrow N_2O^+$	*Nna Mvondo et al.* [2001]
O_3* (electronically excited) + $N_2 \rightarrow N_2O + O_2$	*Prasad* [1981, 2002]
$O_3 \cdot N_2$ (dimer) + hν $\rightarrow N_2O + O_2$	*Prasad* [2002]
$O_3\ (^1B_2) + N_2 \rightarrow N_2O + O_2$ $O_3\ (^3B_1) + N_2 \rightarrow N_2O + O_2$	*Prasad* [2005]
$NO_2 + N \rightarrow N_2O + O$	*Semeniuk et al.* [2008]
NO_3* + $N_2 \rightarrow NO_2 + N_2O$ NO_2* + $N_2 \rightarrow NO + N_2O$	*Zellner et al.* [1992]

Table 5.2. Summary of experimental delivery pressures which determined the flow rate of reactant gases through the corona discharge cell, the steady-state pressure measured downstream from the discharge cell, and the total N_2O collected in the sample cell at the end of each corona discharge experiment.

	Regulator delivery pressure (psi)	Pressure downstream from discharge cell (mTorr)	Approximate amount of N_2O collected (nmol)
Sample 1	15	520	43
Sample 2	15	554	44
Sample 3	15	578	44
Sample 4	15	572	44
Sample 5	15	562	42
Sample 6	15	534	42
Sample 7	15	572	42
Sample 8	25	886	63

Table 5.3. Measured isotopic composition of N_2O formed by corona discharge in air and in campus air samples from the same day.

Sample, aliquot for m/z = 44,45,46	Sample, aliquot for m/z= 30,31	$\delta^{15}N$ vs. Air N_2 (‰)	$\delta^{18}O$ vs. Air O_2 (‰)	$\delta^{15}N$-α vs. Air N_2 (‰)	$\delta^{15}N$-β vs. Air N_2 (‰)	Site Preference (α – β) vs. Air N_2 (‰)	$\delta^{15}N$-α vs. Trop. N_2O (‰)	$\delta^{15}N$-β vs. Trop. N_2O (‰)	Site Preference (α – β) vs. Trop. N_2O (‰)
Group 1 – April 2013, low flow conditions									
Campus air on 4/29/2013	Campus air on 4/30/2013	5.6	20.0	25	-14	40	-1	0	-2
Sample 1, aliquot 1	Sample 3, aliquot 1	-1.9	22.3	8	-11	19	-19	3	-22
Sample 1, aliquot 1	Sample 3, aliquot 2	-1.9	22.3	8	-12	21	-18	2	-20
Sample 2, aliquot 2	Sample 4, aliquot 1	-1.7	22.4	8	-11	19	-19	4	-22
Sample 2, aliquot 2	Sample 4, aliquot 2	-1.7	22.4	8	-12	20	-18	3	-21
	Average*	-1.8±0.1	22.34±0.03	8±1	-11±1	20±1	-18.4±0.5	3±1	-21±1
	(Corona samples – campus air)	-7.4	2.4	-17	3	-20	-17	3	-20
Group 2 – April/May 2014, low flow conditions									
Campus air on 4/29/2014	Campus air on 4/30/2014	4.6	20.6	25	-16	42	-2	-2	0
Sample 5, aliquot 1	Sample 7, aliquot 1	2.5	24.8	15	-11	26	-11	4	-15
Sample 5, aliquot 1	Sample 7, aliquot 2	2.5	24.8	15	-11	26	-11	4	-15
Sample 5, aliquot 2	Sample 7, aliquot 1	2.5	24.8	15	-10	26	-11	4	-16
Sample 5, aliquot 2	Sample 7, aliquot 2	2.2	24.2	16	-11	27	-11	3	-14
Sample 6, aliquot 1	Sample 7, aliquot 1	2.2	24.2	15	-11	26	-11	4	-15
Sample 6, aliquot 1	Sample 7, aliquot 2	1.5	22.6	16	-13	29	-11	2	-13
Sample 6, aliquot 2	Sample 7, aliquot 1	1.5	22.6	15	-12	28	-11	2	-13
Sample 6, aliquot 2	Sample 7, aliquot 2	1.2	22.0	16	-13	30	-11	1	-12
	Average*	1.9±0.5	23±1	15.5±0.3	-12±1	28±1	-11.1±0.3	3±1	-14±1
	(Corona samples – campus air)	-2.7	2.8	-10	4	-14	-9	4	-14

* ± values are the 1σ standard deviation of the averages and do not include propagation of the single measurement uncertainties.

Table 5.3 continued

Sample, aliquot for m/z = 44,45,46	Sample, aliquot for m/z= 30,31	$\delta^{15}N$ vs. Air N_2 (‰)	$\delta^{18}O$ vs. Air O_2 (‰)	$\delta^{15}N$-α vs. Air N_2 (‰)	$\delta^{15}N$-β vs. Air N_2 (‰)	Rel. enrich. (α – β) (‰)	$\delta^{15}N$-α vs. Trop. N_2O (‰)	$\delta^{15}N$-β vs. Trop. N_2O (‰)	Rel. enrich. (α – β) (‰)
Group 3 – April/May 2014, high flow conditions									
Campus air on 5/1/2014	Campus air on 4/30/2014	4.9	20.5	25	-15	41	-2	-1	-1
Sample 8, aliquot 2	Sample 8, aliquot 1	2.6	-1.2	23	-18	41	-4	-3	-1
Sample 8, aliquot 3	Sample 8, aliquot 1	2.6	-0.2	23	-18	41	-4	-3	-1
	Average*	2.60±0.02	-0.68±0.68	22.70±0.04	-17.51±0.01	40.92±0.03	-4.07±0.04	-3.07±0.01	-1.00±0.03
	(Corona samples – campus air)	-2.3	-21.2	-2.4	-2	0	-2	-2	-1

* ± values are given by the 1σ standard deviation of the averages and do not include propagation of the single measurement uncertainties.

Table 5.4. Highlights of results from Table 5.3: Isotopic composition of N_2O in campus air samples and of N_2O formed by corona discharge in air

	$\delta^{15}N$ vs. Air N_2 (‰)	$\delta^{18}O$ vs. Air O_2 (‰)	Rel. enrich. (^{15}N-α – ^{15}N-β) (‰)
Group 1 – low flow			
Campus air	5.6	20.0	40
Average of corona samples	-1.8±0.1	22.34±0.03	20±1
(Corona samples – campus air)	-7.4	+2.4	-20
Group 2 – low flow			
Campus air	4.6	20.6	42
Average of corona samples	1.9±0.5	23±1	28±2
(Corona samples – campus air)	-2.7	+2.8	-14
Group 3 – high flow			
Campus air	4.9	20.5	41
Average of corona samples	2.60±0.02	-0.7±0.7	40.92±0.03
(Corona samples – campus air)	-2.3	-21.2	-0.1

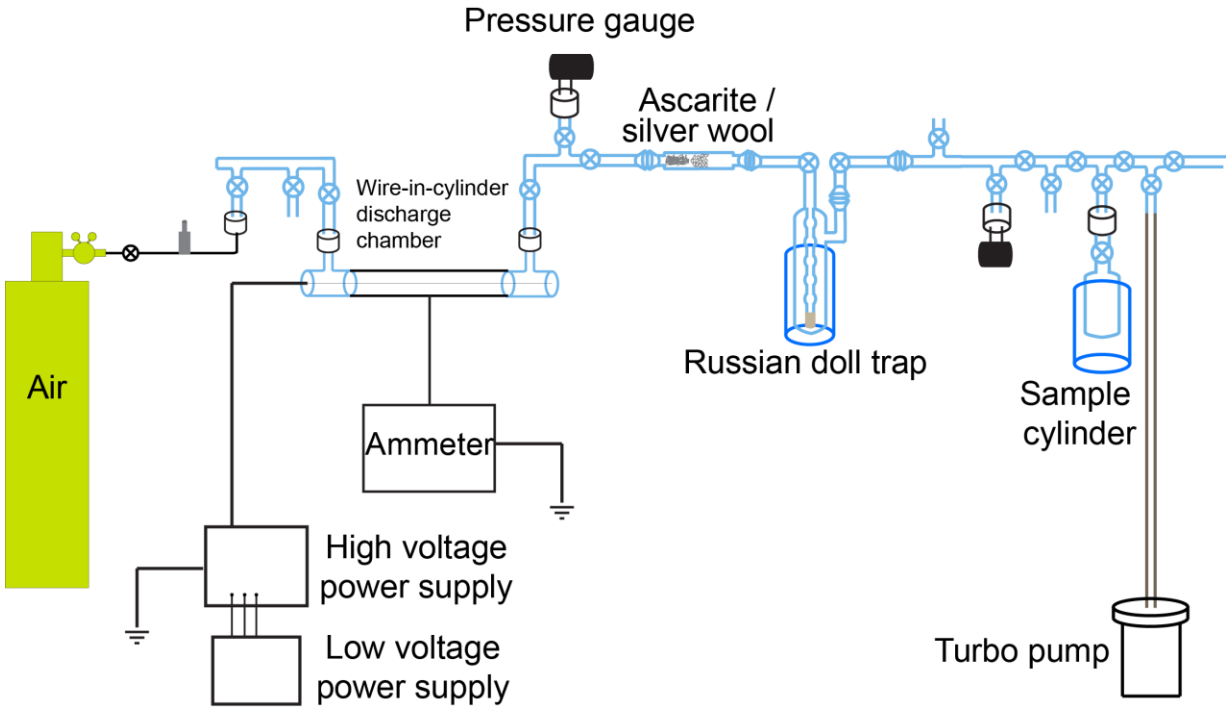

Figure 5.1. Experimental setup for the formation and sample collection of N_2O via corona discharge. Gas flows from left to right from the source cylinder of zero air to the turbo pump. Flow from the zero air cylinder is controlled by changing the regulator delivery pressure and restricting the flow with a needle valve and is directed to the discharge chamber. The discharge chamber consists of a 100 μm diameter tungsten wire with a 5 kV potential applied from the high voltage power supply and a grounded stainless steel cylinder. Downstream of the discharge chamber, ascarite and silver wool act as scrubbers to remove NO_x and ozone, respectively. N_2O is collected in a Russian doll cold trap at 77 K, submerged in liquid nitrogen, and is then transferred to a stainless steel sample cylinder for analysis by isotope ratio mass spectrometry.

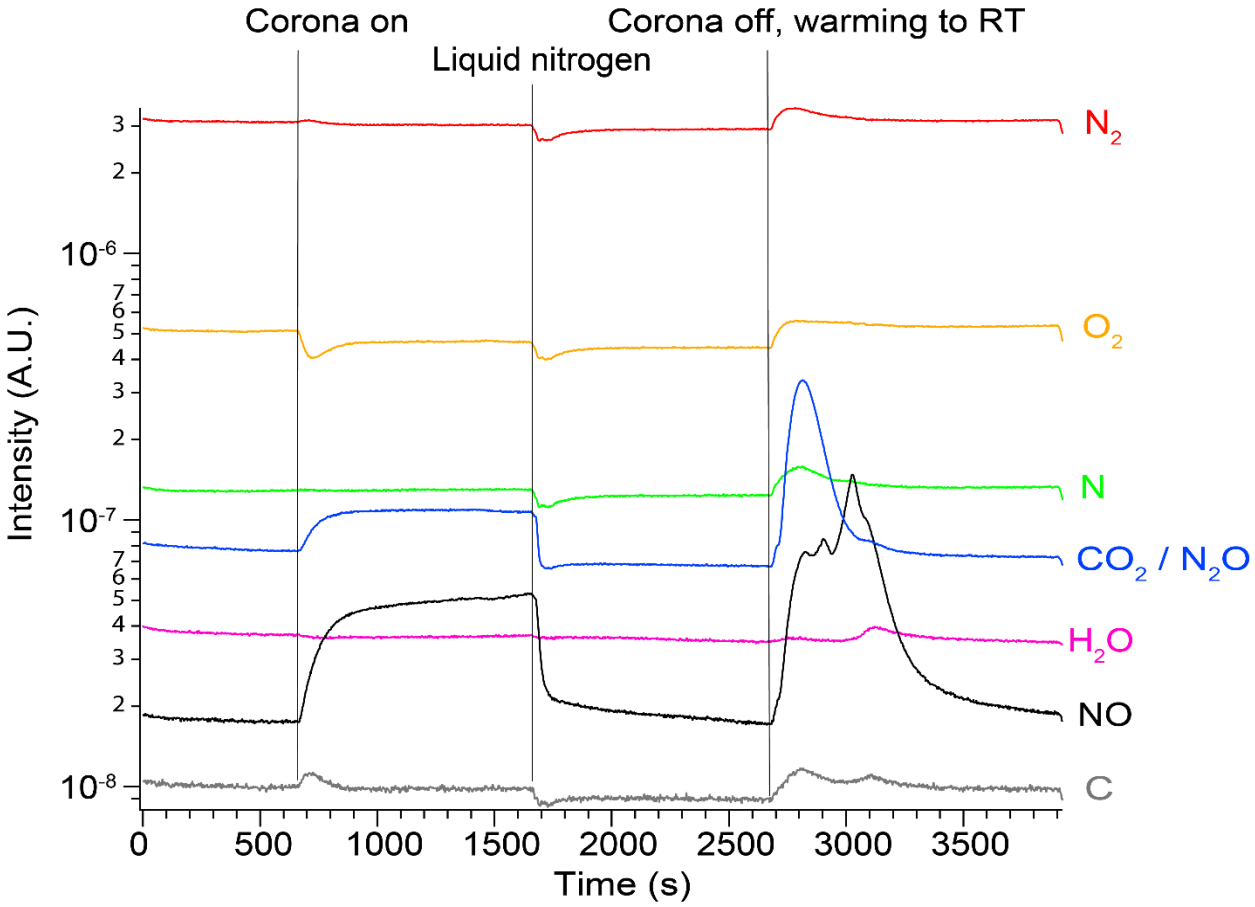

Figure 5.2. Residual gas analyzer signals for the mass-to-charge ratios monitored during the initial test for N_2O formation in the corona discharge experiment. The different stages of the experiment are labeled with vertical gray lines. At 0 seconds, gas from the source cylinder of zero air began flowing in the absence of a corona discharge. Next, the voltage to the corona was switched on, leading to a measurable increase in N_2O and NO. Next, liquid nitrogen was placed on the Russian doll trap, trapping any species condensable at 77 K. Finally, the corona was switched off and the Russian doll trap was allowed to warm to room temperature, revolatilizing the condensable species.

Bhetanbhotla, M.N., B.A. Crowell, A. Coucouvinos, R.D. Hill, and R.G. Rinker (1985) Simulation of trace species production by lightning and corona discharge, *Atmos. Environ., 19*, 1391–1397, doi:10.1016/0004-6981(85)90276-8.

Brandvold, D.K., P. Martinez, and R. Hipsh (1996) Field measurements of O_3 and N_2O produced from corona discharge, *Atmos. Environ., 30*, 973–976, doi:10.1016/1352-2310(95)00234-0.

Brenninkmeijer, C.A.M., and T. Röckmann (1996) Russian doll type cryogenic traps: Improved design and isotope separation effects, *Anal. Chem., 68*, 3050–3053, doi:10.1021/ac960208w.

Cacace, F., G. de Petris, M. Rosi, and A. Troiani (2001) Ionization of O_3 in excess N_2: A new route to N_2O via intermediate $N_2O_3^+$ complexes, *Angew. Chem.-Int. Ed., 40*, 1938–1941.

Chen, J.H., and J.H. Davidson (2002) Electron density and energy distributions in the positive DC corona: Interpretation for corona-enhanced chemical reactions, *Plasma Chem. Plasma Process., 22*, 199–224, doi:10.1023/A:1014851908545.

Cliff, S.S., and M.H. Thiemens (1997) The $^{18}O/^{16}O$ and $^{17}O/^{16}O$ ratios in atmospheric nitrous oxide: A mass-independent anomaly, *Science, 278*, 1774–1776, doi:10.1126/science.278.5344.1774.

Croteau, P. (2010) Nitrous oxide and molecular nitrogen isotopic compositions and aerosol optical properties: experiments and observations relevant to planetary atmospheres. University of California - Berkeley.

Croteau, P., E.L. Atlas, S.M. Schauffler, D.R. Blake, G.S. Diskin, and K.A. Boering (2010) Effect of local and regional sources on the isotopic composition of nitrous oxide in the tropical free troposphere and tropopause layer, *J. Geophys. Res.-Atmospheres, 115*, D00J11, doi:10.1029/2009JD013117.

Demore, W., and O.F. Raper (1962) Reaction of $O(^1D)$ with nitrogen, *J. Chem. Phys., 37*, 2048, doi:10.1063/1.1733425.

Diffenbaugh, N.S., M. Scherer, and R.J. Trapp (2013) Robust increases in severe thunderstorm environments in response to greenhouse forcing, *Proc. Natl. Acad. Sci. U. S. A., 110*, 16361–16366, doi:10.1073/pnas.1307758110.

Donohoe, K.G., F.H. Shair, and O.R. Wulf (1977) Production of O_3, NO, and N_2O in a pulsed discharge at 1 atm, *Ind. Eng. Chem. Fundam., 16*, 208–215, doi:10.1021/i160062a006.

Estupinan, E.G., J.M. Nicovich, J. Li, D.M. Cunnold, and P.H. Wine (2002) Investigation of N2O production from 266 and 532 nm laser flash photolysis of $O_3/N_2/O_2$ mixtures, *J. Phys. Chem. A, 106*, 5880–5890, doi:10.1021/jp014242c.

Feilberg, K.L., A.A. Wiegel, and K.A. Boering (2013) Probing the unusual isotope effects in ozone formation: Bath gas and pressure dependence of the non-mass-dependent isotope enrichments in ozone, *Chem. Phys. Lett., 556*, 1–8, doi:10.1016/j.cplett.2012.10.038.

Fraser, M.E., and L.G. Piper (1989) Product branching ratios from the $N_2(A\ ^3\Sigma_u^+) + O_2$ interaction, *J. Phys. Chem., 93*, 1107–1111, doi:10.1021/j100340a017.

Funke, B., M. Garcia-Comas, M. Lopez-Puertas, N. Glatthor, G.P. Stiller, T. von Clarmann, K. Semeniuk, and J.C. McConnell (2008) Enhancement of N_2O during the October-November 2003 solar proton events, *Atmospheric Chem. Phys.*, *8*, 3805–3815.

Gorshunov, N.M., and S.V. Gudenko (2003) Enrichment of the nitrogen atomic component with the ^{15}N isotope in a post-discharge zone, *Jetp Lett.*, *77*, 162–166, doi:10.1134/1.1571874.

Griffing, G.W. (1977) Ozone and oxides of nitrogen-production during thunderstorms, *J. Geophys. Res.-Oceans Atmospheres*, *82*, 943–950, doi:10.1029/JC082i006p00943.

Hill, R.D., I. Rahmin, and R.G. Rinker (1988) Experimental study of the production of NO, N_2O, and O_3 in a simulated atmospheric corona, *Ind. Eng. Chem. Res.*, *27*, 1264–1269, doi:10.1021/ie00079a029.

Hill, R.D., R.G. Rinker, and A. Coucouvinos (1984) Nitrous oxide production by lightning, *J. Geophys. Res.-Atmospheres*, *89*, 1411–1421, doi:10.1029/JD089iD01p01411.

Hirsch, A.I., A.M. Michalak, L.M. Bruhwiler, W. Peters, E.J. Dlugokencky, and P.P. Tans (2006) Inverse modeling estimates of the global nitrous oxide surface flux from 1998-2001, *Glob. Biogeochem. Cycles*, *20*, GB1008, doi:10.1029/2004GB002443.

Huang, J., A. Golombek, R. Prinn, R. Weiss, P. Fraser, P. Simmonds, E.J. Dlugokencky, B. Hall, J. Elkins, P. Steele, R. Langenfelds, P. Krummel, G. Dutton, and L. Porter (2008) Estimation of regional emissions of nitrous oxide from 1997 to 2005 using multinetwork measurements, a chemical transport model, and an inverse method, *J. Geophys. Res.-Atmospheres*, *113*, D17313, doi:10.1029/2007JD009381.

Iannuzzi, M.P., J.B. Jeffries, and F. Kaufman (1982) Product channels of the $N_2(A\ ^3\Sigma_u^+) + O_2$ interaction, *Chem. Phys. Lett.*, *87*, 570–574, doi:10.1016/0009-2614(82)83180-1.

IPCC (2013) Climate change 2013: The physical science basis. Contribution of working group I to the fifth assessment report of the intergovernmental panel on climate change. T.F. Stocker, D. Qin, Plattner G.-K., M. Tignor, S.K. Allen, J. Boschung, A. Nauels, Y. Xia, Y. Bex, and P.M. Midgley, editors. Cambridge University Press, Cambridge, United Kingdom and New York, USA. 1535 pp.

Kajimoto, O., and R.J. Cvetanović (1976) Formation of nitrous oxide in the reaction of $O(^1D_2)$ atoms with nitrogen, *J. Chem. Phys.*, *64*, 1005–1015, doi:10.1063/1.432308.

Kossyi, I.A., A.Y. Kostinsky, A.A. Matveyev, and V.P. Silakov (1992) Kinetic scheme of the non-equilibrium discharge in nitrogen-oxygen mixtures, *Plasma Sources Sci. Technol.*, *1*, 207–220, doi:10.1088/0963-0252/1/3/011.

Levine, J.S., and E.F. Shaw (1983) In situ aircraft measurements of enhanced levels of N_2O associated with thunderstorm lightning, *Nature*, *303*, 312–314, doi:10.1038/303312a0.

Malcolme-Lawes, D.J. (1974) New route for quenching of $N_2(A\ ^3\Sigma_u^+)$ in aurora, *Nature*, *247*, 540–541, doi:10.1038/247540a0.

Manuccia, T.J., and M.D. Clark (1976) Enrichment of N^{15} by chemical reactions in a glow discharge at 77°K, *Appl. Phys. Lett.*, *28*, 372–374, doi:10.1063/1.88785.

Mauersberger, K., D. Krankowsky, and C. Janssen (2003) Oxygen isotope processes and transfer reactions, *Space Sci. Rev.*, *106*, 265–279, doi:10.1023/A:1024650007258.

Midey, A.J., S. Williams, T.M. Miller, P.T. Larsen, and A.A. Viggiano (2002) Investigation of the reaction of O_3^+ with N_2 and O_2 from 100 to 298 K, *J. Phys. Chem. A*, *106*, 11739–11742, doi:10.1021/jp020311r.

Nna Mvondo, D., R. Navarro-Gonzalez, C.P. McKay, P. Coll, and F. Raulin (2001) Production of nitrogen oxides by lightning and coronae discharges in simulated early Earth, Venus and Mars environments, *Adv. Space Res. Off. J. Comm. Space Res. COSPAR*, *27*, 217–23, doi:10.1016/S0273-1177(01)00050-3.

Park, S., P. Croteau, K.A. Boering, D.M. Etheridge, D. Ferretti, P.J. Fraser, K.-R. Kim, P.B. Krummel, R.L. Langenfelds, T.D. van Ommen, L.P. Steele, and C.M. Trudinger (2012) Trends and seasonal cycles in the isotopic composition of nitrous oxide since 1940, *Nat. Geosci.*, *5*, 261–265, doi:10.1038/NGEO1421.

De Petris, G. (2003) Atmospherically relevant ion chemistry of ozone and its cation, *Mass Spectrom. Rev.*, *22*, 251–271, doi:10.1002/mas.10053.

Prasad, S.S. (1981) Excited ozone is a possible source of atmospheric N_2O, *Nature*, *289*, 386–388, doi:10.1038/289386a0.

Prasad, S.S. (2002) A new model of N_2O quantum yield in the UV photolysis of $O_3/O_2/N_2$ mixtures: Contributions of electronically excited O_3 and $O_3 \cdot N_2$, *J. Chem. Phys.*, *117*, 10104–10108, doi:10.1063/1.1516795.

Prasad, S.S. (2005) Especially significant new component of N_2O quantum yield in the UV photolysis of O_3 in air, *J. Phys. Chem. A*, *109*, 9035–9043, doi:10.1021/jp058114q.

Röckmann, T., J. Kaiser, and C.A.M. Brenninkmeijer (2003) The isotopic fingerprint of the pre-industrial and the anthropogenic N_2O source, *Atmospheric Chem. Phys.*, *3*, 315–323.

Röckmann, T., and I. Levin (2005) High-precision determination of the changing isotopic composition of atmospheric N_2O from 1990 to 2002, *J. Geophys. Res.-Atmospheres*, *110*, D21304, doi:10.1029/2005JD006066.

Semeniuk, K., J.C. McConnell, J.J. Jin, J.R. Jarosz, C.D. Boone, and P.F. Bernath (2008) N_2O production by high energy auroral electron precipitation, *J. Geophys. Res.-Atmospheres*, *113*, D16302, doi:10.1029/2007JD009690.

Severinghaus, J.P., A. Grachev, B. Luz, and N. Caillon (2003) A method for precise measurement of argon 40/36 and krypton/argon ratios in trapped air in polar ice with applications to past firn thickness and abrupt climate change in Greenland and at Siple Dome, Antarctica, *Geochim. Cosmochim. Acta*, *67*, 325–343, doi:10.1016/S0016-7037(02)00965-1.

Sowers, T., A. Rodebaugh, N. Yoshida, and S. Toyoda (2002) Extending records of the isotopic composition of atmospheric N_2O back to 1800 AD from air trapped in snow at the South Pole and the Greenland Ice Sheet Project II ice core, *Glob. Biogeochem. Cycles*, *16*, 1129, doi:10.1029/2002GB001911.

Thiemens, M.H., S. Chakraborty, and G. Dominguez (2012) The Physical Chemistry of Mass-Independent Isotope Effects and Their Observation in Nature, *Annu. Rev. Phys. Chem. Vol 63*, *63*, 155–177, doi:10.1146/annurev-physchem-032511-143657.

Trapp, R.J., N.S. Diffenbaugh, H.E. Brooks, M.E. Baldwin, E.D. Robinson, and J.S. Pal (2007) Changes in severe thunderstorm environment frequency during the 21st century caused by anthropogenically enhanced global radiative forcing, *Proc. Natl. Acad. Sci. U. S. A.*, *104*, 19719–19723, doi:10.1073/pnas.0705494104.

Wofsy, S.C. (2011) HIAPER Pole-to-Pole Observations (HIPPO): fine-grained, global-scale measurements of climatically important atmospheric gases and aerosols, *Philos. Trans. R. Soc. -Math. Phys. Eng. Sci.*, *369*, 2073–2086, doi:10.1098/rsta.2010.0313.

Zellner, R., D. Hartmann, and I. Rosner (1992) N_2O formation in the reactive collisional quenching of NO_3^* and NO_2^* by N_2, *Berichte Bunsen-Ges.-Phys. Chem. Chem. Phys.*, *96*, 385–390.

Zipf, E.C. (1980) A laboratory study on the formation of nitrous oxide by the reaction $N_2(A\ ^3\Sigma_u^+) + O_2 \rightarrow N_2O + O$, *Nature*, *287*, 523–524, doi:10.1038/287523a0.

Zipf, E.C., and S.S. Prasad (1980) Production of nitrous oxide in the auroral D regions and E regions, *Nature*, *287*, 525–526, doi:10.1038/287525a0.

Zipf, E.C., and S.S. Prasad (1982) A mesospheric source of nitrous oxide, *Nature*, *295*, 133–135, doi:10.1038/295133a0.